# Zeeman Relaxation of Cold Iron and Nickel in Collisions with $^3$He

by

Cort Nolan Johnson

Submitted to the Department of Physics
in partial fulfillment of the requirements for the degree of

Doctor of Philosophy

at the

MASSACHUSETTS INSTITUTE OF TECHNOLOGY

May 2008

Author . . . . . . . . . . . . . . . . . . . . . . . . . . . . . . . . . . . . . . . . . . . . . . . . . . . . . . . .
Department of Physics
May 23, 2008

Certified by . . . . . . . . . . . . . . . . . . . . . . . . . . . . . . . . . . . . . . . . . . . . . . . . . . . .
Daniel Kleppner
Lester Wolfe Professor of Physics, Emeritus
Thesis Supervisor

Certified by . . . . . . . . . . . . . . . . . . . . . . . . . . . . . . . . . . . . . . . . . . . . . . . . . . . .
Thomas Greytak
Lester Wolfe Professor of Physics
Thesis Supervisor

Accepted by . . . . . . . . . . . . . . . . . . . . . . . . . . . . . . . . . . . . . . . . . . . . . . . . . . . .
Thomas Greytak
Chairman, Department Committee on Graduate Students

# Zeeman Relaxation of Cold Iron and Nickel in Collisions with $^3$He

by

Cort Nolan Johnson

Submitted to the Department of Physics
on May 23, 2008, in partial fulfillment of the
requirements for the degree of
Doctor of Philosophy

## Abstract

This thesis describes a measurement of the ratio of elastic to Zeeman-projection changing collision cross sections ($\gamma$) in the Fe-$^3$He and Ni-$^3$He systems. This ratio is a probe of the anisotropy of the interaction between the colliding species. Theory and experiment confirm that Zeeman-projection collisions are suppressed in transition metals due to the presence of a spherically symmetric, full $4s$ shell, making them good candidates for loading a magnetic trap with the buffer gas cooling method.

Nickel and iron atoms are introduced via laser ablation into an experimental cell containing a background $^3$He buffer gas. Elastic collisions with the buffer gas thermalize the atoms to less than 1K. The highest energy $m_J = J$ Zeeman state decays via diffusion through the buffer gas and collisional Zeeman relaxation. Therefore the $m_J = J$ lifetime depends on the buffer gas density of the cell. By measuring the $m_J = J$ lifetime as a function of buffer gas density we determine $\gamma$. We find $\gamma$ for Ni [$^3F_4$, $m_J = 4$] is between $2 \times 10^3$ and $1.1 \times 10^4$ at 0.75 K in a 0.8 T magnetic field. Zeeman relaxation in Fe [$^5D_4$, $m_J = 4$] occurs on time scales too rapid for us to measure accurately, and we are only able to set an upper bound of $\gamma < 3 \times 10^3$. The nickel result confirms that Zeeman relaxation is highly suppressed in submerged shell transition metal atoms.

Thesis Supervisor: Daniel Kleppner
Title: Lester Wolfe Professor of Physics, Emeritus

Thesis Supervisor: Thomas Greytak
Title: Lester Wolfe Professor of Physics

# Acknowledgments

It has been a great pleasure and honor to work with my advisors Tom Greytak and Dan Kleppner over the past seven years. I appreciate their dedication to high quality work and have learned essentially everything I know about being an experimental physicist within the exciting framework of their labs. I appreciate all of their efforts on my behalf over the years. My family will miss our visits to their vacation homes. It has also been a great pleasure to collaborate with John Doyle over the last 4 years. His experimental creativity and confidence brings an excitement and vitality to each meeting that bolsters morale.

The labmates I have worked with over the years have become my very close friends. In the early years Kendra Vant, Lia Matos, and Julia Steinberger were the core of my lab existence working on the historic Hydrogen BEC apparatus. Lia's friendly demeanor put me at ease immediately. She gave me my introduction to lasers and was patient along the way. I feel that Kendra is a truly kind person, as she made sure we socialized outside of work to remind us that we were friends first and labmates second. Julia is remarkable and generous with a passion for making the world and her working environment a better place and backs it up with action. Another big influence in my early years was Lorenz Willmann. His excitement for the work and encyclopedic knowledge were truly inspiring. It was truly a pleasure to see so many of my early co-workers have children while here at MIT...it made my wife and me feel less out of place.

In recent years I have worked with Rob deCarvalho, Chih-Hao Li, Nathan Brahms and Bonna Newman. Rob's cheerful enthusiasm for thinking through a problem was a breath of fresh air. I have yet to meet a more friendly, kind man than Chih-Hao. He knew everything, but didn't act like it. It has been a great pleasure working so closely with Nathan and Bonna over the past 4 years. Nathan has a passion for the world of physics that is difficult to match and is generous with his knowledge. His persistence in encouraging me to take lunch breaks with him are evidence of his kindness. Bonna is a natural leader. I have learned much watching her generously dedicate her time

to the physics community and the MIT community at large. I always appreciate her concern for my family.

Steven and Cristie Charles have been our dear friends and neighbors for the past seven years. I thank them especially for their friendship but also for their help and support.

I word of thanks must be given to Jim Kunka, my 8th grade math teacher, who taught me that "Math is Beautiful". He gave freely of his time during the summer to prepare me for a math competition. I did not win, but his efforts had a profound impact on me. From him I discovered that extra-curricular learning was exciting and fun; a principle I hope to pass on to others.

I have two wonderful parents whose focus has always been their children. The trips home have been few over the past seven years, but I have always felt their love and support from a distance. From them I learned so many things that have been indispensable while at MIT: faith, patience, hard work, and love of learning. My brother Rhett and his wife Patty were there for us when we first arrived, and helped us make Boston our beloved home, and them our beloved friends. My twin brother Dirk and I have always been close and his many encouraging conversations over the years have brought me comfort.

I believe in God. I believe He has shown me how to live a happy and balanced life. This believe has been a comfort on many levels throughout my experience at MIT, and I thank Him for His many gifts to me and my family.

The balance of this thesis could easily be my acknowledgment to my absolutely amazing, patient, beautiful, brilliant, and wonderfully supportive wife. Neither of us quite knew the implications of what we were getting ourselves into when we drove across the country with all our possessions in tow, and our infant son along for the ride. It cannot be overstated how generous and supportive she has been throughout our MIT experience. We have had two more children since then, and it is all of them that make my life one worth living: Ethan, for his wisdom, Elliot for his zest for life, Claire for her sweet disposition, Corey, for her love. If there were any justice in this world her name, Coreen Nikole Johnson, would also be on my diploma.

# Contents

# List of Figures

# List of Tables

# Chapter 1

# Introduction

## 1.1 Cooling and Trapping Atoms

A resurgence of atomic and molecular physics has occurred over the past several decades. Much of the renewed enthusiasm has come about due to advances in the cooling and trapping of atoms and molecules. By cooling atoms to ultracold temperatures ($\sim \mu K$), unprecedented control of the external and internal atomic degrees of freedom has been achieved. The realization of Bose-Einstein condensation [1, 2] in metastable gases was both a seminal accomplishment and a launching point for further work. Studies of ultracold trapped samples are helping to advance the fields of quantum information, precision measurement and atomic clocks, and quantum simulation of condensed matter systems to name a few. The current research landscape and the prospects for the coming decade have recently been reviewed [3]. However, the individual research fields advance rapidly and the any review is sure to become outdated quickly.

If an atomic sample is to be confined by a magnetic potential, its thermal energy must be less than the strength of its interaction with the confining potential. This requires cooling atoms to temperatures on the order of 1K or less, even for the largest fields achievable in the lab. The atomic species most often trapped are those which can be laser cooled [4]. A stationary atom absorbs photons with energy equal to the energy splitting between the atomic ground and excited states. A moving atom absorbs photons at a different energy due to the Doppler shift. When a laser is red detuned from an atomic transition, counter-moving atoms experience resonant excitation and are slowed due to photon recoil during the excitation process. When the excited atom emits the photon, it does not need to emit into the laser mode but can emit in any direction with equal probability. The emitted photons will on average have the energy equal to a photon absorbed by an atom at rest. Thus on average the emitted photons are more energetic than the absorbed photons and cooling occurs. Laser cooling requires many scattering events, so a closed transition is required to make the cooling feasible. It is possible to add other lasers to pump atoms back into the ground state of the cooling transition, but this becomes impractical for atoms with complex electronic structures. In practice, this limits the method to alkali and alkali earth atoms and a handful of others across the periodic table. For atoms with complex electronic structures there is no closed transition, laser cooling is impossible, and other methods must be used to thermalize atoms to trappable temperatures.

## 1.2 MIT Ultracold Hydrogen Group: Background

The MIT ultracold hydrogen group has a rich history of developing cryogenic techniques for loading spin polarized atomic hydrogen into a magnetic trap. These efforts led to the only successful demonstration to date of Bose condensed atomic hydrogen [5–7]. A crucial feature of the group's approach was the use of a superfluid film of He on the inner wall of an experimental cell to cool atomic hydrogen to a sufficiently low temperature to confine it in a magnetic trap [6]. This technique is effective only for atomic hydrogen due to hydrogen's low binding energy on the helium film [8]. For all other species free space confinement is not possible because the binding energy with the film is so high that the atoms are adsorbed onto the surface. For example, our group's diligent efforts to trap deuterium using the same approach proved fruitless [9, 10]

The group desired more experimental flexibility in its next generation apparatus. Thermalizing atoms to low temperatures via elastic collisions with a cold buffer gas

- buffer gas cooling - is an attractive alternative for trapping atoms. This method accommodates a wide range of atomic species because it does not depend upon a specific internal atomic degree of freedom (e.g. laser cooling) or thermalization with a cryogenic helium film. A major goal was to accelerate the evaporative cooling process by increasing the elastic collision rate using a second trapped species. With buffer gas cooling it is straightforward to trap two species simultaneously in the same trap [11]. For these reasons, in 2003 our group began designing and constructing a trapping apparatus based upon buffer gas cooling. Design and construction began with several experimental goals in mind.

Evaporative cooling hydrogen to BEC is very difficult in large part because of the small H-H elastic cross section [12]. The cross section for collisions between alkali atoms and hydrogen is predicted to be roughly 3 orders of magnitude larger than the H-H cross section [13, 14]. It was therefore proposed that co-trapping an alkali species and hydrogen would greatly increase the thermalization rate of hydrogen during evaporative cooling and accelerate the path to hydrogen BEC.

An ultracold, trapped hydrogen samples holds great potential for precision measurement of the two-photon $1S-2S$ transition in the simple hydrogen system. Such a measurement can be used to extract improved values for the Rydberg constant and the Lamb shift, and has possible clock applications [15]. Several laser sources had been developed for the purpose of performing such measurements [15, 16] before the old apparatus was decommissioned. We were anxious to resume that line of research as soon as possible.

Our long standing goal to trap deuterium was also a high priority. Once the new apparatus could successfully trap hydrogen, deuterium trapping was expected to follow in a straightforward manner since film binding energy issues are avoided by the buffer gas method.

All of these long term research goals first required the ability to load hydrogen or deuterium into a magnetic trap using the buffer gas method. The technical challenge of loading a magnetic trap increases as the strength of the atomic magnetic moment decreases, as discussed in Section 1.3.1. The state of the art in buffer gas loading at the time we began designing the apparatus was that trapping effective magnetic moments of 3 $\mu_B$ was straightforward but became difficult below $\sim 2\,\mu_B$. [17]. For 1 $\mu_B$ species the interaction with the magnetic field is weak. These species must be loaded into the trap at very low temperatures. In addition, the background buffer gas causes atom loss from the trap. Energetic buffer gas atoms impart their kinetic energy to trapped atoms, promoting them into trajectories that carry them over the trap edge and onto the cell wall. Trap losses are particularly rapid for 1 $\mu_B$ species because the trap depth is relatively low. Therefore, the buffer gas must be removed quickly to minimize this loss and thermally isolate the trapped sample from its surroundings. Buffer gas loading of 1 $\mu_B$ CaH molecules has been demonstrated [18]. However, the enhancement in lifetime over the zero-field diffusion lifetime was only a factor of 4 and all molecules were lost from the trap before the buffer gas could be removed. Thus, thermal isolation was not achieved and evaporative cooling could not be implemented.

The primary research effort of the group in recent years has been specific to advancing buffer gas loading technology to permit trapping a 1 $\mu_B$ species and to thermally isolate the species by removing the buffer gas. Much of the design and implementation of the 1 $\mu_B$ apparatus is the focus two companion theses by Nathan Brahms and Bonna Newman [19, 20]. Although 1 $\mu_B$ species have been trapped and studied in our apparatus [21], obstacles we encountered increased the development time of the apparatus and prevented further study of hydrogen. As a result, the measurements in this thesis are on a different topic. They consist of a variety of studies of buffer gas loading the transition metals nickel, cobalt, and iron with magnetic moments greater than 5 $\mu_B$. The success of the buffer gas loading process depends crucially on the properties of collisions between the buffer gas and the species of interest. Elastic collisions are necessary to thermalize the sample while inelastic collisions can drive trapped atoms into untrapped states. The following section reviews buffer gas loading of magnetic traps and the relevant collisions. In particular we discuss the properties of transition metals that make their collisions with the buffer gas particularly interesting.

## 1.3 Loading Magnetic Traps by Buffer Gas Cooling: The Crucial Ratio of Elastic to Inelastic Collisions

Laser cooling is elegant, but it has a serious limitation. It only works for atoms for which lasers are available to drive principal transitions and which have a suitable energy level structure. Buffer gas cooling has emerged as an alternative to laser cooling in recent years [22]. Elastic collisions with cryogenically cooled helium buffer gas atoms provide the mechanism to thermalize atoms and molecules to temperatures at which they can be trapped. Thermalization occurs for all species and does not depend on a specific, simple internal energy level structure. The method's flexibility has been demonstrated by the trapping of many atomic and molecular species [21, 23, 24] and the list continues to grow.

Although elastic collisions with the buffer gas can thermalize any species, not all species can be loaded into magnetic traps with buffer gas cooling. The method only works for species with a high ratio of elastic to inelastic collision cross sections $\gamma$. Inelastic collisions can change a trappable low-field seeking atom into an untrappable high-field seeking atom through a change in the orientation of its magnetic moment, a process we will refer to as "Zeeman relaxation". This balance between elastic and inelastic collisions is interesting from a collisional physics standpoint alone [25–28]. For the experimenter the balance is crucial for predicting the possibility of using the buffer gas method to load an atomic species into a magnetic trap. The following sections review the physics of thermalization and inelastic collisions with a buffer gas, and motivate the studies of iron and nickel presented in later chapters.

### 1.3.1 Thermalization with the buffer gas

The initial condition for our experiments is a burst of hot atoms at temperature $T_{hot}$ produced via laser ablation by focusing a pulsed Nd:YAG laser onto a metallic foil target. In order to trap them with current superconducting magnet technology they must be cooled, but to what temperature?

We introduce the trap depth $E_B = g\mu_B B_{trap}$, where g is the atomic g-factor, $\mu_B$ is the Bohr magneton, and $B_{trap}$ is the magnetic field at the trap edge[1]. The g-factor varies between about 1 (e.g. H) and 10 (e.g. Dy) for atoms with electronic magnetic moments. Defining the ratio of trap depth to thermal energy $\eta \equiv (g\mu_B B_{trap})/(k_B T)$, we see that $\eta > 1$ must hold to achieve trapping.

Our superconducting magnet has a 4T field at the cell wall. Since $\mu_B/k_B = 0.67K/T$ this results in a $2.7K$ trap depth when $g = 1$, i.e. for a 1 Bohr magneton atom. This limit of $2.7K$ tells us we need to be operating at cryogenic temperatures. The lifetime of the trapped sample increases as $\eta$ increases. Thus the task of trapping gets easier as the magnetic moment of the atom increases. In practice, one loads the trap at as high an $\eta$ as possible[2].

Details of the thermalization process are presented elsewhere [29] using conservation of momentum and energy and assuming hard sphere elastic scattering. After thermal averaging, the analysis shows that if an atom of mass $M$ and temperature $T_{hot}$ collides with a buffer gas atom of mass $m$ at $T_{bg}$, the change in temperature $\Delta T$ due to a single collision is

$$\Delta T = -\frac{T_{hot} - T_{bg}}{\kappa} \tag{1.1}$$

with

$$\kappa = \frac{(M+m)^2}{(2Mm)}. \tag{1.2}$$

Treating the number of collisions N as a continuous variable, we can put this into differential form and solve for the atom temperature $T_{at}$:

---

[1] This assumes the lowest magnetic field in the trap is $\left|\vec{B}\right| = 0$, a condition satisfied in the anti-Helmholtz geometry we normally use.

[2] This is not strictly true. If two-body collisions between the trapped atoms are the dominant loss mechanism it may be favorable to load at a lower $\eta$ in order to keep the density of the trapped sample low.

$$\frac{dT_{at}}{dN} = -\frac{1}{\kappa}(T_{at} - T_{bg}) \tag{1.3}$$

$$T_{at} = T_{bg} + (T_{hot} - T_{bg})e^{-N/\kappa}. \tag{1.4}$$

Since $\kappa \sim M/2m$ when $M >> m$, the number of collisions required to thermalize a heavy atom is linear in atomic mass.

Equation 1.3 gives us insight into the buffer gas density needed in an experiment of typical dimensions. It takes $\sim 100$ collisions to thermalize atoms so they can fall into a magnetic trap. The width of a typical experimental cell is on the order of 10 cm. By assuming linear motion through the buffer gas we arrive at an estimate of the needed buffer gas density required for thermalization[3]. Since $\sim 100$ collisions must take place over $\sim 10$ cm distance, the mean free path $\lambda = 1/(n_{bg}\sigma_{el})$ must be about 0.1cm. Typical values for $\sigma_{el}$ are $\sim 10^{-14}\,cm^2$, so buffer gas densities must be greater than $10^{15}\,cc^{-1}$.

The number of thermalizing collisions is particularly low for atoms with masses close to the mass of the buffer gas. This is manifest in the fact that we can effectively load lithium $M_{Li} = 7$ a.m.u. into our magnetic trap at buffer gas densities close to $10^{15}\,cc^{-1}$ [19]. However, for heavier species studied such as Ag, Cu, Fe, and Ni we do not see appreciable numbers of thermalized atoms below $\sim 5 \times 10^{15}\,cc^{-1}$.

### 1.3.2 Inelastic collisions with the buffer gas

In addition to elastic thermalizing collisions, inelastic processes can induce transitions between magnetic Zeeman levels. This is a problem since magnetic fields in free space can only confine low-field seeking atoms [30]. A thermalized, trapped atom's magnetic

---

[3] Initially, ablated atoms will be moving at much higher speeds than the buffer gas and collisions will do little to deflect their trajectories. This assumption breaks down as thermal equilibrium is approached and a random walk through the buffer gas occurs. In this case the distance traveled $\propto \sqrt{N_{collisions}}\lambda$. We assume the worst case scenario: the distance traveled $\propto N_{collisions}\lambda$.

moment is anti-aligned with the magnetic field; an energetically unfavorable situation. Inelastic collisions can reorient the magnetic moment and align it with the field, causing the atom to be expelled from the trap. Therefore, a key physical parameter for buffer gas loading of magnetic traps is the ratio of elastic to inelastic collision cross sections, $\gamma$. Since we need $\sim 100$ collisions for thermalization, we have no hope of trapping a species with $\gamma < 100$. In practice the required $\gamma$ is higher because it takes a finite amount of time to remove buffer gas from the cell as discussed in Chapter 3. Loading the trap is generally impossible for $\gamma < 10^4$.

In practice, finding the ideal buffer gas density for loading a given atomic species into the magnetic trap is an empirical process. Increasing buffer gas density thermalizes more atoms to trappable temperatures. However, increasing buffer gas density also increases the rate of inelastic collisions. Maximizing the number of trapped atoms requires finding a buffer gas density which balances initial thermalization and subsequent Zeeman relaxation. The ideal density must be found empirically for each atom.

## 1.4 Zeeman Relaxation in non-S-state Atoms

### 1.4.1 Background and previous work

Recent buffer gas loading experiments have generated a flurry of theoretical activity predicting the Zeeman relaxation rates for collisions between atoms and molecules with helium at cold temperatures [25–27, 27]. During a collision between an atomic species and a helium atom there is an angular momentum $\vec{N}$ associated with the rotation of the "diatom" formed by the colliding atoms. Zeeman transitions in the atomic species occur when its electronic orbital angular momentum $\vec{L}$ interacts with the angular momentum of the diatom $\vec{N}$ [26]. The coupling strength between $\vec{L}$ and $\vec{N}$ depends upon the anisotropy of the electrostatic interaction between colliding atoms.

**S-state versus non-S-state Behavior**

In a purely S-state atom the electronic magnetic moment is due solely to the electron spin $\vec{S}$. Spin angular momentum does not couple directly to the diatomic angular momentum during a collision; since S-state atoms interact through isotropic electrostatic potentials, Zeeman relaxation should not occur. In reality the collision will mix in a small amount of non-S-state behavior. This adds a component of nonzero orbital angular momentum $\vec{L}$ to the atom which will couple to the electronic spin through the $\vec{L} \cdot \vec{S}$ fine structure coupling. There will also be an coupling between $\vec{L}$ and $\vec{N}$ as described above. Since $\vec{L}$ is coupled to both $\vec{S}$ and $\vec{N}$, there is an indirect coupling between $\vec{S}$ and $\vec{N}$ which will induce spin relaxation [31–33]. However, this effect is generally small and $\gamma$ for S-state atoms colliding with helium is sufficiently high to allow buffer gas loading [21, 34–36]. For example, $\gamma$ for Cu-He and Ag-He collisions is greater than $10^6$ between 300 mK and 600 mK [21].

The interaction potential between non-S-state atoms with structureless partners can be highly anisotropic and induce rapid collisional Zeeman relaxation. For example, calculations for main group $^3P$ atoms at $T < 1K$ show that the anisotropy is large and $\gamma \sim 1$. [26]

### 1.4.2 Submerged shell atoms

It might be supposed that any non-S-state atom would Zeeman relax quickly due to the anisotropy of its valence electron cloud. However, the interaction anisotropy with the colliding helium atom can be mitigated by the presence of outer filled shells. Non-S-state transition metals have a full $s$ shell surrounding the $d$ shell valence electrons, i.e. the electronic configuration is $nd^m(n+1)s^2$. The $4s$ orbital is isotropic and its average radius is more than two times the size of the $3d$ orbital. [37, 38]. During a collision, the $4s$ transition metal electrons repel the helium atom via the coulomb interaction before it overlaps appreciably with the anisotropic $3d$ cloud. As a result, the anisotropy of the interaction between a transition metal and a helium atom is suppressed and $\gamma$ should be much higher than for the case of a $^3P$ atom. Theoretical studies of scandium and titanium predict that $\gamma$ is on the order of $10^3 - 10^4$ for transition metal-helium collisions [28]. An experimental value for Ti of $\sim 4 \times 10^4$ confirms the theoretical prediction. Upper limits on $\gamma$ for scandium ($\gamma < 1.6 \times 10^4$) and yttrium ($\gamma < 3 \times 10^4$) have been reported; attempts with Zirconium failed due to inconsistent ablation yields [39, 40].

Similar suppression of Zeeman relaxation has also been exhibited for a large number of rare earth atoms with large magnetic moments. Values of $\gamma$ were found to be greater than $10^4$ for Pr, Nd, Tb, Dy, Ho, Er, and Tm and all species were magnetically trapped [24]. Theory has confirmed that the interaction anisotropy between these atoms and helium is indeed very small [27].

### 1.4.3 Motivation to study iron, cobalt, and nickel

These previous theoretical and experimental efforts have shown that magnetic trapping is possible for a much wider array of atomic species than previously considered. Within this framework we were motivated to continue the investigation of transition metal trapping and focused our efforts on iron, cobalt, and nickel.

The magnetic moments of these transition metals are much larger than those of previous transition metals studied. The magnetic moments of Ti, Sc, Zr, and Y are all less than 1.5 $\mu_B$. Buffer gas loading of species with such low magnetic moments into magnetic traps presents numerous challenges detailed elsewhere [17, 19]. Thus it is technologically advantageous to trap species with higher moments. In addition, it was suggested that nickel in particular would have a large value of $\gamma$, making it an attractive transition metal candidate for magnetic trapping [41].

Previous trapping attempts with transition metals were not as fruitful as those with rare earths due to their lower values of $\gamma$ [40]. Our apparatus was primarily designed to trap 1 $\mu_B$ species and has many features necessary for rapid buffer gas removal [19]. We are therefore more equipped than previous groups to successfully trap species with low values of $\gamma$ such as the transition metals.

## 1.5 Thesis Overview

We study the Zeeman relaxation rate in cold collisions of cobalt, iron, and nickel with $^3$He by measuring the decay lifetime of the $m_J = J$ most low-field seeking Zeeman state. This is the state that interacts most strongly with the magnetic field and will be most tightly confined by a trapping field. The Zeeman relaxation rate increases linearly with the buffer gas density. By performing a series of lifetime measurements of the $m_J = J$ state as a function of buffer gas density, we observe this behavior and can determine the ratio of elastic to inelastic cross sections $\gamma$.

When the thermal energy of the atoms is much less than the energy splitting between adjacent Zeeman levels, collisions are not energetic enough to excite an atom from a lower energy Zeeman state into a high energy Zeeman state. As the temperature increases, the probability for thermal excitation also increases. When the thermal energy is approximately equal to the interaction with the magnetic field, the decay of the $m_J = J$ state no longer decays at the Zeeman relaxation rate. Thermal repopulation decreases the rate of decay, resulting in an increase in the observed lifetime. When making Zeeman relaxation measurements it is ideal to operate in the low temperature regime where the Zeeman relaxation behavior is not altered by collisional excitations.

We can not make our lifetime measurements in the ideal low temperature regime. To resolve the $m_J = J$ spectra we apply a Helmholtz magnetic field in the experimental cell. The field is nearly uniform but has some inhomogeneity. As a result, the observed atomic transitions are magnetically broadened and the peak absorption signal decreases with increasing magnetic field strength. This decrease in signal strength at high fields makes lifetime measurements impossible. We therefore must operate at magnetic fields where the thermal energy is approximately equal to the energy splitting between adjacent Zeeman states. As a result, our lifetime measurements are affected by thermal excitations into the $m_J = J$ state.

In Chapter 2 we address the issue of thermal excitations by developing a theoretical framework to accurately describe the dynamics of the $m_J = J$ state. The theory includes losses due to diffusion through the buffer gas, Zeeman relaxation, and thermal excitation. The model includes the couplings between all Zeeman levels and simulates the evolution of all $m_J$ populations. Using the tools developed we can interpret our measured data to extract the value of $\gamma$.

Chapter 3 describes the buffer gas apparatus we constructed and used to make the measurements. We give a detailed description of the design and construction of the experimental cell used in these studies and in our group's 1 $\mu_B$ trapping and evaporative cooling experiments. We explain the spectroscopic methods used to determine atom density, temperature, and lifetime. The laser systems used in the experiments are also described.

Chapter 4 presents our studies of Zeeman relaxation in cold collisions of cobalt, iron, and nickel atoms with $^3$He. We could not determine $\gamma$ for cobalt because it was impossible to fully resolve the $m_J = J$ transition due to the high multiplicity of the atomic transitions arising from cobalt's hyperfine structure. We find $\gamma$ for nickel to be between $2 \times 10^3$ and $1.1 \times 10^4$. Two effects contribute must significantly to the uncertainty. Although the data follows the expected qualitative trends, it is not possible to find a single value of $\gamma$ that fits the entire data range well and only a range of possible values of $\gamma$ can be determined. Second, uncertainties in the model occur because we do not know the exact nature of the coupling between the various $m_J$ levels during the Zeeman relaxation. This limits the accuracy of the predicted collisional excitation effects on the lifetime of the $m_J = J$ state, which effect the value of $\gamma$. The Zeeman relaxation of iron occured on a timescale too rapid for us to determine a value for $\gamma$. We set an upper limit for iron of $\gamma < 3 \times 10^3$.

# Chapter 2

# Buffer Gas Effects on Most Low-field Seeking State Dynamics: Diffusion, Zeeman Relaxation, and Thermal Excitation

In theory an atom in any low field seeking state, one where the energy is an increasing function of the magnetic field strength, can be confined in a magnetic trap. This would comprise either half (for half-integer $J$) or slightly less than half (for integer $J$) of the Zeeman split states in a given $J$ manifold in the high field limit. The state with the greatest value of $m_J$ will be the most strongly confined, the others less so. If one waits long enough, most of the atoms remaining in the trap will be those with the largest value of $m_J$. We refer to these atoms by a special name, the"most low field seeking" or MLFS atoms. They play a special role in magnetic trapping and are the focus of our attention in these experiments.

## 2.1 Buffer Gas Effects on MLFS lifetimes

Elastic and inelastic collisions with the background $^3$He buffer gas affect the lifetime of MLFS atoms in our experimental cell. Therefore, a careful study of the MLFS state lifetime $\tau_{MLFS}$ serves as a probe of collisional properties and can yield a value for the ratio of elastic to inelastic cross sections $\gamma$.

There are two primary loss mechanisms for MLFS atoms. First, when the mean free path for atom-helium collisions $\lambda$ is less than the dimensions of the trapping cell $R_{cell}$ the atoms diffuse via elastic collisions through the buffer gas and eventually stick to the cryogenically cooled wall. The diffusion lifetime increases linearly with buffer gas density. Second, inelastic collisions lead to relaxation of the MLFS state into Zeeman states of lower energy. The Zeeman relaxation lifetime is inversely proportional to buffer gas density.

It is important to note that we can, and do, measure the diffusion lifetime directly by watching the density of all of the atoms decay in the absence of a magnetic field. To examine the lifetime of the MLFS atoms we must apply a magnetic field to be able to identify those particular states.

When $\lambda >> R_{cell}$ and a trapping field is energized, the MLFS atoms can be held for long times. However, individual elastic collisions with helium atoms from the high energy portion of the Boltzmann distribution promote trapped atoms into energetic orbits that intersect the cell wall. This provides a constant source of heating which will induce evaporative loss over the trap edge. These effects become very important when attempting to thermalize trapped samples in a buffer gas apparatus. Under the best of circumstances, when atom-helium collisions are rare, the lifetime of the MLFS atoms in the trap will be limited by state changing atom-atom collisions (dipole relaxation). The experiments detailed in this thesis operate in the region $\lambda < R_{cell}$ without magnetic trapping, so these effects are irrelevant. Details of the $\lambda >> R_{cell}$ regime can be found elsewhere [19].

In addition to loss mechanisms, there is also the possibility of collisional excitation into the MLFS state from lower energy Zeeman states. This source of MLFS atoms increases $\tau_{MLFS}$ in the cell. These effects are only important when the thermal energy $k_B T$ is approximately equal to or larger than the Zeeman energy splitting $g\mu_B B$. For our experimental conditions these effects must be taken into account when we extract a value of $\gamma$ from our observations.

In the sections below models are derived that include diffusion and Zeeman relaxation losses and thermal excitation sources. Chapter 3 explains how to measure $\tau_{MLFS}$ in our experimental cell as a function of buffer gas density. Using the models presented here it is possible to determine $\gamma$ from our measurements of MLFS atom decay.

## 2.2 MLFS Lifetime Models Without Thermal Excitation

A simple $\tau_{MLFS}$ vs. $n_{BG}$ model including only diffusive and Zeeman relaxation losses is the first step toward quantifying MLFS dynamics. The $\tau_{MLFS}$ versus $n_{BG}$ model is instructive because it is easy to visualize the collision rates increasing as we add more buffer gas. Unfortunately, such a model is not ideal for our experimental conditions. It is impossible for us to measure the buffer gas density directly. As we shall see, the diffusion lifetime depends on the product of buffer gas density and elastic collision cross section. Since we do not know the elastic cross sections of the atoms studied, we can not solve for an absolute buffer gas density. Alternative models that require no knowledge of absolute buffer gas density are therefore presented. Although these models may be slightly less intuitive, they have the advantage of needing only one fit parameter to solve for $\gamma$.

The models presented in this section ignore collisions that repopulate the MLFS state once the atom has relaxed into a lower energy state. We shall deal with this finite temperature effect in Section 2.3.

### 2.2.1 $\tau_{MLFS}$ vs. $n_{BG}$

#### Zero-Field Diffusion

The lifetime in the absence of a magnetic field is set by diffusion through the buffer gas. With no buffer gas in the cell atoms travel ballistically to the walls and stick. In this case the lifetime is determined by the thermal velocity distribution. When enough buffer gas is introduced such that $\lambda << R_{cell}$, elastic collisions reorient atomic trajectories and impede their journey to the wall. The motion becomes diffusive and $\tau_{MLFS}$ becomes linearly dependent on buffer gas density.

The spatial distribution and temporal evolution of the diffusing atoms is determined by the diffusion equation

$$\frac{\partial n}{\partial t} = D\nabla^2 n. \tag{2.1}$$

where the diffusion constant $D$ is given by [42]

$$D = \frac{3\pi}{32}\frac{\overline{v}_d}{n_{bg}\sigma_d} \tag{2.2}$$

where $n_{bg}$ is buffer gas density, $\sigma_d$ is the diffusion cross section[1], $\overline{v}_d$ is the average relative thermal velocity [42].

Equation (2.1) can be solved for a cylindrical cell of length $L_{cell}$ and radius $R_{cell}$ with the boundary condition $n = 0$ at the cell wall. The solution consists of a series of spatial eigenmodes multiplied exponential decays in time. The lowest order spatial mode $n_0(\vec{r})$ and its accompanying lifetime $\tau_d$ are

$$\begin{aligned} n_0(\vec{r}) &= n_0(0)J_0\left(\frac{j_{01}r}{R}\right)\cos\left(\frac{\pi z}{L}\right), && (2.3)\\ \tau_d &= \frac{32}{3\pi}\frac{n_{bg}\sigma_d}{\overline{v}_d G}, && (2.4)\\ G &= \left(\frac{\pi^2}{L_{cell}^2} + \frac{j_{01}^2}{R_{cell}^2}\right). && (2.5) \end{aligned}$$

where $j_{01}$ is the first zero of the $J_0(r)$ Bessel function. Higher order modes decay more rapidly than $n_0(\vec{r})$, so our measurements of diffusion lifetime in the cell are measurements of the decay of the lowest order mode.

---

[1] For distinguishable particles, the diffusion cross section is typically smaller than the elastic cross section $\sigma_{el}$ by a factor of order unity. We do not know the exact relationship between $\sigma_d$ and $\sigma_{el}$ for the atoms studied and take them to be equal in this thesis.

### Zeeman Relaxation

The interaction between an atom with a magnetic moment $\vec{\mu}$ and a magnetic field $\vec{B}$ causes a splitting of the zero-field energy levels. The interaction Hamiltonian is

$$H_Z = -\vec{\mu} \cdot \vec{B}. \tag{2.6}$$

Energy is minimized when the magnetic moment aligns with the magnetic field. The magnetic moment for an atom with total electron angular momentum $\vec{J}$ is

$$\vec{\mu} = -g_J \mu_B \vec{J} \tag{2.7}$$

$$\tag{2.8}$$

where $g_J$ is the landé g-factor. The Hamiltonian can now be written as

$$\begin{aligned} H_Z &= g_J \mu_B \vec{J} \cdot \vec{B}; & (2.9) \\ &= g_J \mu_B m_J B & (2.10) \end{aligned}$$

where $m_J$ is the projection of the total angular momentum along the magnetic field axis and takes on the $2J+1$ values $-J, -J+1, ...J-1, J$. The most low-field seeking (MLFS) Zeeman state ($m_J = J$) is the maximum energy state and has its magnetic moment anti-aligned with the field.

Zeeman relaxation occurs when $m_J$ changes during a collision with a buffer gas atom. Overall, this results in a transfer of atomic population from low field seeking states to high field seeking states. The time scale associated with inelastic collisions is

$$\tau_{zr} = \frac{1}{\overline{v}_{zr} \sigma_{zr} n_{bg}}, \tag{2.11}$$

where $\overline{v}_{zr}$ is the average relative thermal velocity, $\sigma_{zr}$ is the inelastic cross section for

Zeeman relaxation collisions, and $n_{bg}$ is the buffer gas density. Specifically we take $\sigma_{zr}$ to refer to the total cross section for transitions from the MLFS state into any of the other Zeeman states, not simply a specific one such as the next lowest one in energy. Also, although $\tau_{zr}$ depends on temperature through $\overline{v}_{zr}$, it does not take into account the possible repopulation of the MLFS state through subsequent collisions. The quantity of physical importance in magnetic trapping and cooling is $\gamma$, the ratio of elastic to inelastic cross-sections. Introducing this parameter into (2.11) yields

$$\tau_{zr} = \frac{\gamma}{\overline{v}_{zr}\sigma_d n_{bg}} \tag{2.12}$$

**MLFS Lifetime**

Combining these effects yields the expected lifetime for a most low-field seeking atom in the cell. The total lifetime, $\tau_{MLFS}$, is the inverse of the total loss rate of MLFS atoms from the cell. This total loss rate is the sum of the diffusion and Zeeman relaxation loss rates:

$$\gamma_{MLFS} = \frac{1}{\tau_{MLFS}} = \Gamma_d + \Gamma_{zr} = \left(\frac{1}{\tau_d} + \frac{1}{\tau_{zr}}\right). \tag{2.13}$$

Defining $\chi \equiv (3\pi/32)G$ and inserting (2.4) and (2.12) into (2.13) yields

$$\tau_{MLFS} = \frac{n_{bg}}{a + b n_{bg}^2} \tag{2.14}$$

$$a = \frac{\chi \overline{v}_d}{\sigma_d} \tag{2.15}$$

$$b = \frac{\overline{v}_{zr}\sigma_d}{\gamma} \tag{2.16}$$

In this model $a$ and $b$ can be used as parameters which can be adjusted to fit experimentally measured data on $\tau_{MLFS}$ vs. $n_{BG}$. Multiplying $a$ and $b$ together cancels the unknown $\sigma_d$ to yield an expression for $\gamma$

$$\gamma = \frac{\overline{v}^2\chi}{ab}. \tag{2.17}$$

where we have set $\overline{v}_{zr} = \overline{v}_d$ and replaced them with $\overline{v}$.[2]

We now convert the above model into forms that do not require direct knowledge of absolute buffer gas density.

### 2.2.2 MLFS lifetime vs. mean free path

It is straightforward to reformulate the previous analysis in terms of the diffusive mean free path, $\lambda_d = 1/(n_{bg}\sigma_d)$. The atom loss rate expressions become:

$$\Gamma_d = \chi\overline{v}\lambda_d \tag{2.18}$$

$$\Gamma_{zr} = \frac{\overline{v}}{\gamma\lambda_d}. \tag{2.19}$$

The resulting total lifetime is

$$\tau_{MLFS} = \frac{\lambda_d}{\alpha + \beta\lambda_d^2} \tag{2.20}$$

$$\alpha = \frac{\overline{v}}{\gamma} \tag{2.21}$$

$$\beta = \chi\overline{v}. \tag{2.22}$$

Although this may look like the previous model with two fit parameters, $\beta$ in (2.22) is a known quantity[3] Thus the model has only one fit parameter. This convenience has occurred because we never decoupled $n_{bg}$ and $\sigma_d$, both unknowns, in the analysis. This is a fairly intuitive way to think about the data as well. We could now imagine

---

[2] The previous distinction between $\overline{v}_{zr}$ and $\overline{v}_d$ in the above expressions is worth discussing. Experimentally, we first measure the diffusive lifetime at zero field. We then turn on a Helmholtz field and measure the low field seeker lifetime. The temperature of the atoms during the two measurements are not necessarily the same, thus $\overline{v}_{zr}$ and $\overline{v}_d$ may in practice be different. For our experimental conditions the atomic temperatures for the two measurements were found to be the same, so the distinction shall be ignored.

[3] The quantity $\beta$ is determined assuming the geometry of the cell and the temperature of the atoms is known. We know the geometry precisely and measure the atom temperature spectroscopically as discussed in Section 3.3.3.

plotting lifetime against the average distance between atom-helium collisions. Fitting for $\alpha$ we could pull out $\gamma$ as desired:

$$\gamma = \frac{\overline{v}}{\alpha}. \tag{2.23}$$

### 2.2.3 $\tau_{MLFS}$ vs. diffusion lifetime

Another alternative approach is to plot the MLFS state lifetime measured in constant field versus the zero-field diffusion lifetime. Plotting one lifetime versus another lifetime might not be intuitive, but from an experimental standpoint it makes perfect sense. In practice, we first measure the zero-field lifetime and then turn on the magnetic field and measure the lifetime of the MLFS state. If we use the mean free path model, we have to calculate $\lambda_d$ from our measured $\tau_d$ prior to analysis using

$$\lambda_d = (\chi \overline{v}_d \tau_d)^{-1}. \tag{2.24}$$

We can avoid this step by using $\tau_d$ directly in our atom loss rate expressions:

$$\Gamma_d = \frac{1}{\tau_d} \tag{2.25}$$

$$\Gamma_{zr} = \frac{\overline{v}^2 \tau_d \chi}{\gamma} \tag{2.26}$$

which yields

$$\tau_{MLFS} = \frac{\tau_d}{1 + \zeta \tau_d^2} \tag{2.27}$$

$$\zeta = \frac{\overline{v}^2 \chi}{\gamma} = \Gamma_d \Gamma_{zr}. \tag{2.28}$$

In this form it is most obvious that there is only one fit parameter $\zeta$ from which $\gamma$ can be obtained:

$$\gamma = \frac{\overline{v}^2\chi}{\zeta}. \tag{2.29}$$

This is similar to the expression found in (2.17) but we need only one fit parameter. Figure 2-1 plots the $\tau_{MLFS}$ vs $\tau_d$ for $\gamma = 10^4$ along with curves for pure diffusion and Zeeman relaxation as guides to the eye.

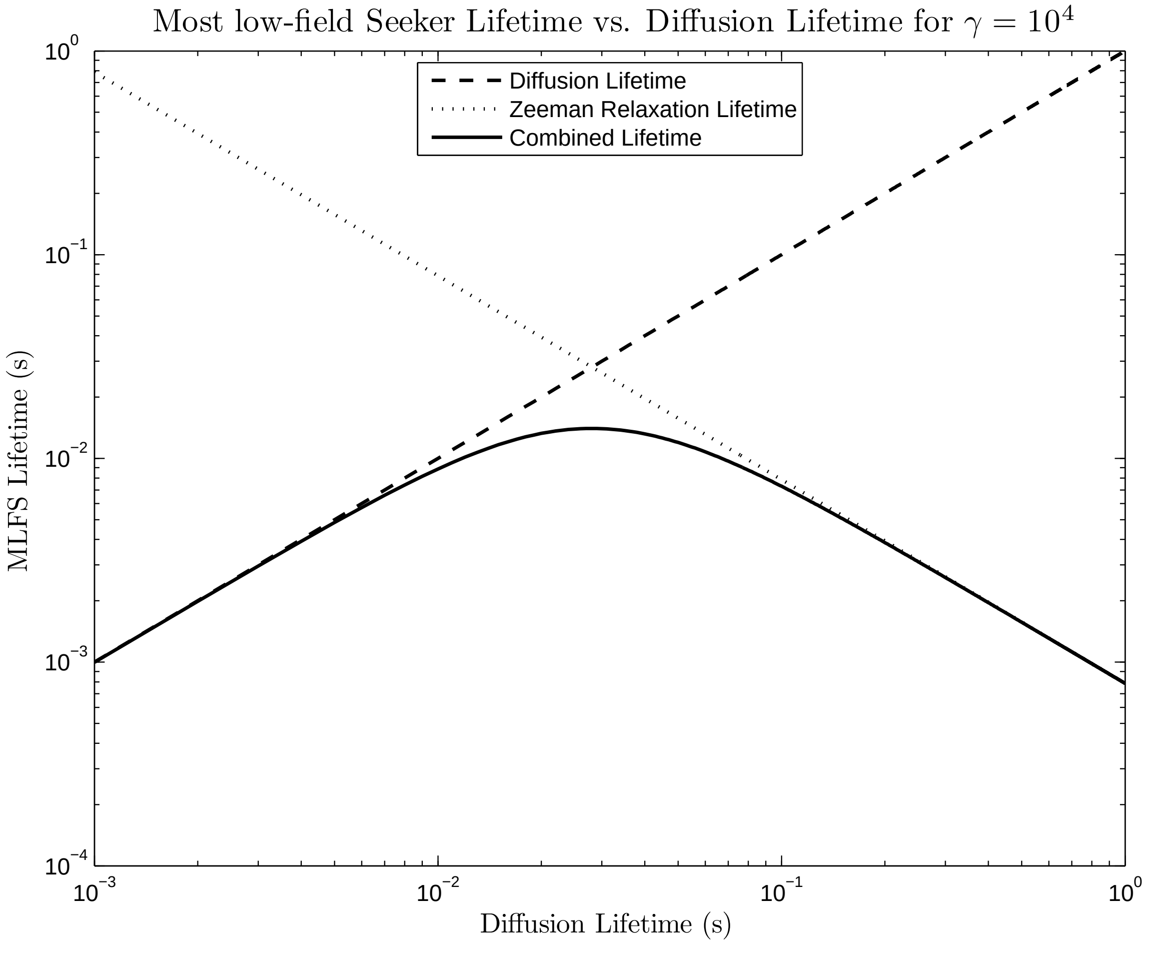

Figure 2-1: Simple MLFS lifetime vs. diffusion lifetime model. Dotted lines denote pure Zeeman relaxation and diffusion losses. The model assumes that no thermal excitations occur.

None of the above models include a trapping field, that is, one which is both strong and non-uniform. Thus they only apply to MLFS states observed in a constant (non-trapping) Helmholtz field geometry. The presence of a magnetic trap will obviously extend the lifetime of MLFS atoms in the cell. Trapping field effect are taken into account by simply multiplying the diffusion lifetime by a factor that depends on $\eta$. Monte Carlo simulations of trapped lifetimes [21] show that the diffusion lifetime in the trap $\tau_{Dtrap}$

$$\tau_{Dtrap} = \tau_d e^{0.24\eta + .03\eta^2}. \tag{2.30}$$

All of the measurements performed in this thesis were done in the Helmholtz geometry. We shall not consider the effects of trapping fields henceforth.

## 2.3 Zeeman Cascade Simulations

### 2.3.1 Importance of including Zeeman cascade effects

In the previous analysis, only Zeeman relaxation and diffusion loss were included. This is an excellent starting point as it introduced the most relevant loss processes in the system. In addition, the model was used successfully in our copper and silver trapping experiments to fit for $\gamma$ [21]. Initially we hoped to explain our transition metal data using such a simple model. However, as will be seen in Chapter 4, the experimental conditions require further effects to be included.

In Section 2.2 it was assumed that once a MLFS atom experienced Zeeman relaxation it remained in a lower energy Zeeman state forever; the possibility of excitation <u>into</u> the MLFS states was ignored. When the thermal energy $k_B T$ is much less than the magnetic interaction energy, this assumption is valid because collisions do not have sufficient energy to excite atoms into states with higher $m_J$. However, at temperatures and magnetic fields where $k_B T << g_J \mu_B B$ does not hold, a non-negligible percentage of the collisions with the buffer gas have enough energy to excite an atom into a higher energy Zeeman state. Thermal excitations act as a source of atoms into the $m_J = J$ state. Therefore they slow the decrease of the MLFS state population in the cell. We are trying to measure $\gamma = \sigma_{el}/\sigma_{zr}$ by measuring $\tau_{MLFS}$ in the cell. Any increase in the observed $\tau_{MLFS}$ due to thermal excitation can be mistaken as a decrease in $\Gamma_{zr}$, which is $\propto \sigma_{zr}$. This leads to an overestimate of $\gamma$. Therefore, a correct determination of $\gamma$ from measured data must take thermal excitations into account. Why do we care, since this is a natural part of the buffer gas cooling process? Because once we know the intrinsic $\sigma_{el}/\sigma_{zr}$ ratio, we can model the buffer gas cooling at any temperatures that occur during the evolution of a particular implementation of the process.

The treatment of Zeeman relaxation in Section 2.2 had no discussion of which Zeeman state an $m_J = J$ atom decays into during Zeeman relaxation. The $m_J = J$ state does not necessarily decay directly into the lowest energy $m_J = -J$ state. Instead it experiences a Zeeman relaxation cascade down through the Zeeman levels. As we shall see, the exact nature of the cascade through the various lower energy Zeeman levels significantly changes the predicted MLFS decay behavior.

We measure the loss of the most high-field seeking (MHFS) $m_J = -J$ atoms to confirm our understanding of atom loss process in the cell. The only expected loss mechanism for MHFS atoms is diffusion to the walls. The diffusion lifetime $\tau_d$ is measured at zero-field where all $m_J$ states are degenerate. The MHFS state decay is measured in Helmholtz field and compared with the $\tau_d$. For a steady state MHFS state population $\tau_d$ should equal $\tau_{MHFS}$. However, the cascade of atoms into the MHFS state from the initial non-equilibrium distribution of states masks the expected diffusion behavior and must be taken into account to fully understand MHFS state evolution.

For the above reasons a more complete model which includes the dynamics of all intermediate Zeeman states and the possibility of thermal excitation must be developed. A full model must include the Zeeman Cascade, thermal excitation, and diffusion. However it is instructive to introduce these effects individually to understand their contribution to the dynamics. Using the models derived, the population dynamics of all Zeeman states can be understood and compared with experimental data.

One other important issue must be considered when developing the Zeeman cascade model. Although it may be clear that a Zeeman cascade will occur, the exact nature of the decay is not so clear. Are all transitions equally allowed? Are there selection rules on $\Delta m_J$ for the transitions? What are the relaxation rates into the individual lower levels? The quantitative answers to these questions are nontrivial even for the experienced theorist [41]. The assumptions adopted significantly affect the predicted behavior, and the various assumptions are worth exploring. We will consider three "selection rule" cases for Zeeman relaxation: all transitions equally allowed, $\Delta m_J = \pm 1$, and an intermediate regime. The first two are extreme cases while the third is more realistic. We shall adopt as our "realistic" case the behavior described in [43, p.4] and [26, p.4]. The authors demonstrate that $\Delta m_J = \pm 1, 2$ transitions rates are comparable while transitions get weaker for $\Delta m_J > \pm 2$. This general statement is true for atoms with large [43] and small [26] values of $\gamma$. For thulium, a "submerged shell" rare earth atom, the rates for $\Delta m_J > \pm 2$ can be as much as 20% to the total rate. While we do not know the exact numbers for our atoms, we adopt the "selection rules" shown in Table 2.1 which are consistent with the trends in the literature. The $\Delta m_J = \pm 1, 2$ transitions are assigned a value 1. The values given for the $\Delta m_J > \pm 1, 2$ transition rates are relative to the $\Delta m_J \pm 1, 2$ transition rates. We are not too concerned that we can only approximate the rates for transitions with large values of $\Delta m_J$ since they do not contribute appreciably to the overall behavior. These values will be used to analyze the data presented in Chapter 4.

| $\Delta m_J = \pm 1, 2$ | $\Delta m_J = \pm 3, 4$ | $\Delta m_J = \pm 5, 6$ | $\Delta m_J = \pm 7, 8$ |
|---|---|---|---|
| 1 | 0.2 | 0.04 | 0.008 |

Table 2.1: Assumed relative rate constants for Zeeman relaxation. All entries are relative to $\Delta m_J = \pm 1, 2$ rate constants. These values are realistic guesses based upon the literature [26, 43].

### 2.3.2 Zeeman cascade without thermal excitation

An $m_J = J$ MLFS atom is unlikely to decay straight into the $m_J = -J$ MHFS state. It can decay to any state with lower energy, i.e. $m_J{}' < J$. Subsequent inelastic collisions will continue to push the atom to even lower energy states. This evolution is referred to as a Zeeman cascade.

### Assumption: all relaxation rates equal

First, let's assume the relaxation rates are equal for every energetically allowed transition. The total rate out of the $m_J = J$ state is $\Gamma_{zr}$ as in Section 2.2. There are $2J$ states lower in energy, so the rate into each individual lower energy level is $\Gamma_{zr}/(2J)$. We assume this is the correct rate for any Zeeman transition from a higher energy state $m_J$ into a lower energy state ${m_J}'$. Under these conditions the following equations describe the density dynamics of each $m_J$ level and the behavior at t = 0 for the MHFS and MLFS states:

$$\dot{n}_{m_J} = -\frac{\Gamma_{zr}}{2J}\sum_{{m_J}'<m_J} n_{m_J} + \frac{\Gamma_{zr}}{2J}\sum_{{m_J}'>m_J} n_{{m_J}'}. \tag{2.31}$$

$$\dot{n}_{MLFS}(t=0) = -\frac{\Gamma_{zr}}{2J}(2J)n_0 = -\Gamma_{zr}n_0 \tag{2.32}$$

$$\dot{n}_{MHFS}(t=0) = \frac{\Gamma_{zr}}{2J}(2J)n_0 = \Gamma_{zr}n_0 \tag{2.33}$$

where $n_0$ is the density at t = 0. The initial densities for all $m_J$ states are assumed to be equal[4]. Particular attention is given to the MHFS and MLFS dynamics at t = 0 because we only monitor these populations in our experiments. We will see later that these initial rates will be altered when collisional excitations are included in the model.

Figure 2-2 shows the solution to (2.31) for ground state nickel ($^3F_4$) with $\Gamma_{zr} = 100\,s^{-1}$. At $t = 0$ the $m_J = J$ atoms decay as a single exponential with $\tau_{zr} = 1/\Gamma_{zr}$, but the other states do not. All of the high-field seeking states ($m_J < 0$) initially grow in population. However, only the MHFS $m_J = -J$ population continues to grow at

---

[4] This is a roughly accurate description of our experimental conditions considering we introduce atoms at temperatures above $10^3K$ via ablation. Recall that for a state of energy $E$, its population is $\propto exp(-E/(k_BT))$. Since typical Zeeman splittings are roughly characterized by $k_B/\mu_B = 0.67K/T$, the 0.8T field used to resolve Zeeman levels produces splittings of $\sim 1K$. The initial temperature is much higher than this, so all Zeeman states populations will be roughly equal.

long times; eventually all states decay into the MHFS state.

A note of explanation is needed regarding the t = 0 slope of the MLFS states in Figure 2-2. The value of $\Gamma_{zr}$ used in the simulations is 100 s$^{-1}$. From equation (2.32) we find the t = 0 slope for the MLFS state equals $\Gamma_{zr} n_{MLFS}$. The normalization in the simulation is such that the summation of all $m_J$ state populations = 1. Therefore $n_{MLFS}(t = 0) = 1/9$ and the initial slope of the decay is $\Gamma_{zr}/9$. The same effect occurs throughout the chapter in figures displaying simulated Zeeman Cascades.

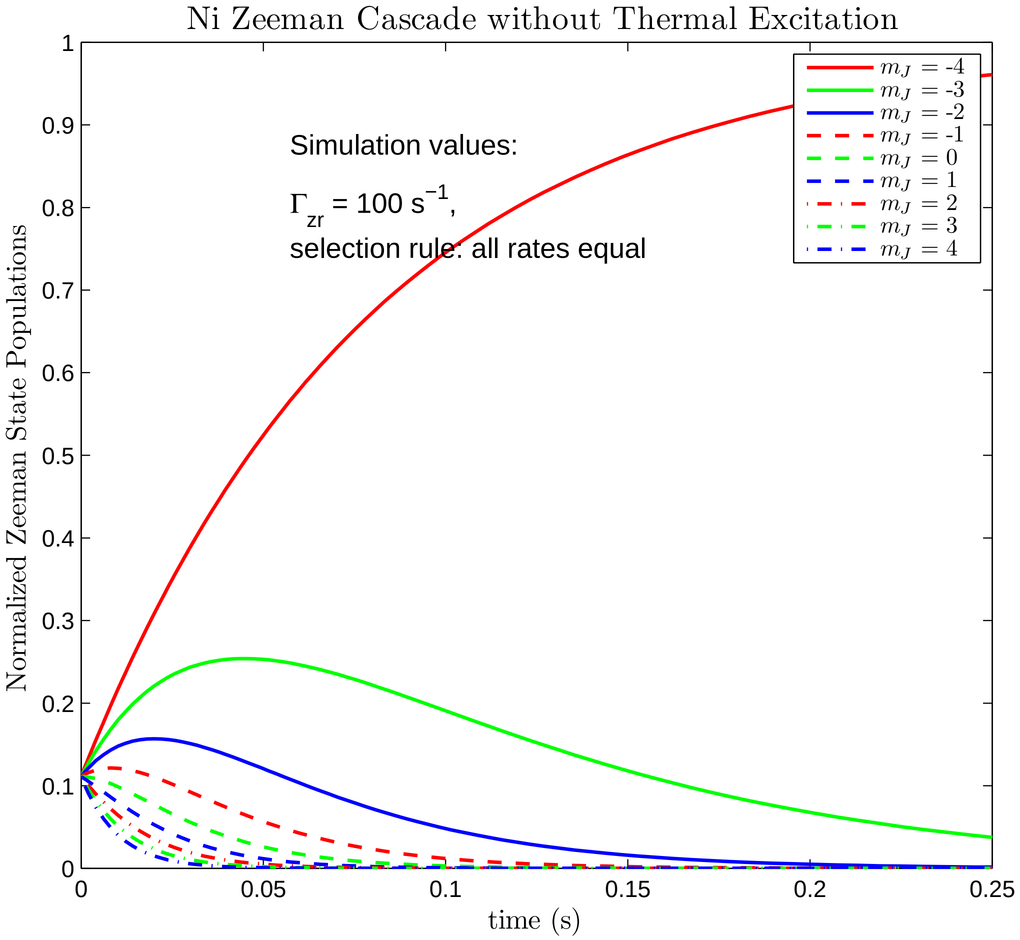

Figure 2-2: Nickel Zeeman cascade without thermal excitation assuming equal relaxation rates to all lower levels and a Zeeman relaxation rate of 100 $s^{-1}$ for the MLFS state. Notice that initially all high field seeking ($m_J < 0$) states have an increase in their populations. As $t \to \infty$ all atoms relax into the $m_J = -J$ stretched state because no thermal re-excitation occurs. The approach to equilibrium is slower than the $\Delta m_J = \pm 1$ case shown in Figure 2-3 because initially the MLFS state is being fed by all states above it. Its rate of growth slows as the upper states are depopulated.

**Assumption: selection rule $\Delta m_J = \pm 1$**

Next we assume a selection rule for Zeeman relaxation of $\Delta m_J = \pm 1$ and a decay rate $\Gamma_{zr}$ between adjacent Zeeman states. The above model simplifies into the following equations:

$$\begin{aligned}
\dot{n}_{m_J} &= -\Gamma_{zr} n_{m_J} && \text{for MLFS } m_J = J, && (2.34)\\
\dot{n}_{m_J} &= -\Gamma_{zr} \left( n_{m_J} - n_{m_J+1} \right) && \text{for } m_J \neq J, -J, && (2.35)\\
\dot{n}_{m_J} &= \Gamma_{zr} n_{m_J+1} && \text{for MHFS } m_J = -J, && (2.36)\\
\dot{n}_{MLFS}(t=0) &= -\Gamma_{zr} n_0, && && (2.37)\\
\dot{n}_{MHFS}(t=0) &= \Gamma_{zr} n_0. && && (2.38)
\end{aligned}$$

Figure 2-3 shows the dynamics predicted by this model. The MLFS state density decays at an exponential rate of $\Gamma_{zr}$ as in the previous model. A comparison with Figure 2-2 shows that it takes less time for the $m_J = -J$ state to reach its asymptotic value that it did in the previous model. This can be understood by examining the rate into the MHFS state. The $m_J = -3$ state is the source of atoms into the MHFS state with a decay rate equal to $\Gamma_{zr}$. This is a factor of 2J larger than the rate for the $m_J = -3 \rightarrow m_J = -4$ transition assumed in the previous model when there were no constraints on $\Delta m_J$. In addition, the $m_J = -3$ population does not decay appreciably until several $1/\Gamma_{zr}$ time scales have passed. For these reasons the rate into the MHFS state remains high and it approaches its equilibrium density more rapidly than in the previous model. The intermediate $m_J \neq J, -J$ level populations remain constant at early times because their initial decay and growth rates are equal.

**Assumption: realistic selection rules**

It is straightforward to adapt Equation (2.31) to accommodate arbitrary selection rules. For each $\Delta m_J = i$ transition we assign a weighting factor $\alpha_i$ such that the $\Delta m_J = i$ transition rate $= \alpha_i \Gamma_{zr}$. In the case of the selection rules we have chosen in

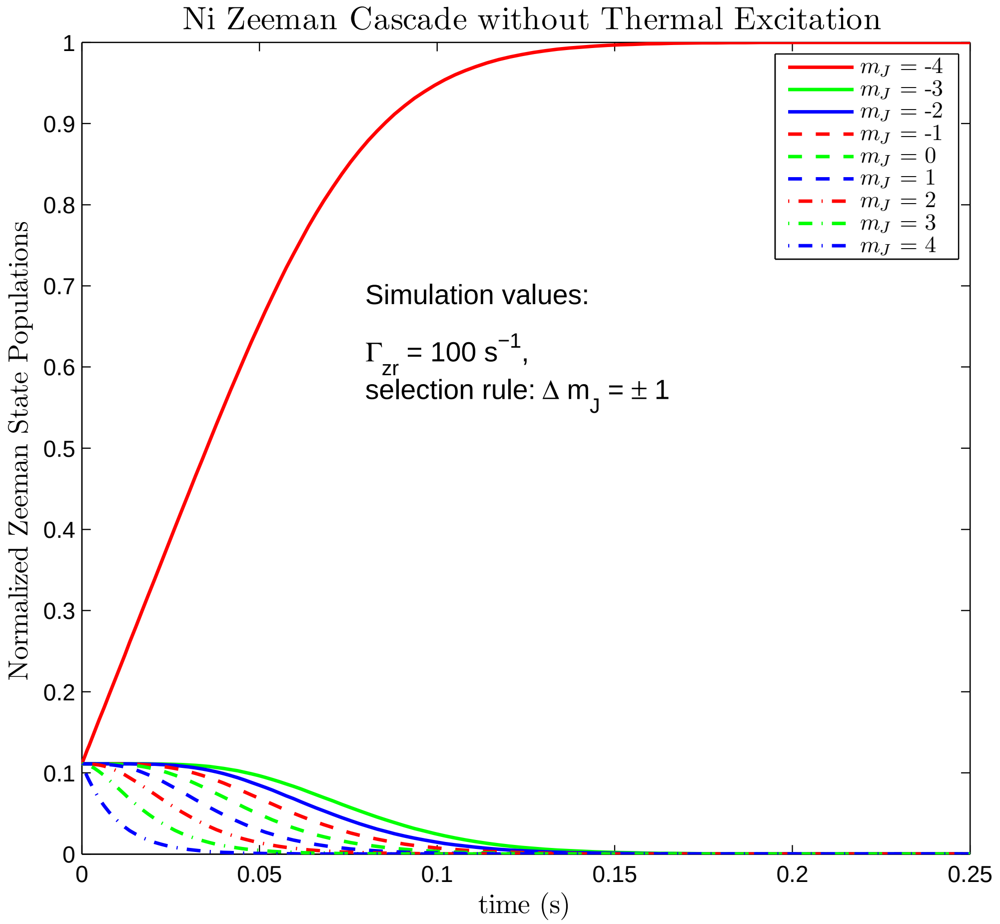

Figure 2-3: Nickel Zeeman cascade without thermal excitation assuming $\Delta m_J = 1$. Under these assumption the MHFS population approaches its final value more rapidly than in the case when there were no constraints on $\Delta m_J$. This occurs because the $m_J = -3$ state population feeding the MHFS state remains high and the assumed rate constant between any two states is a factor of 2J higher than in the previous model. The $m_J = J$ state decay is equal for both models. Intermediate Zeeman states experience no population change at early times because their initial growth and decay rates perfectly balance.

Table 2.1 the weighting factors are $\alpha_1 = \alpha_2 = 1$, $\alpha_3 = \alpha_4 = 0.2$, $\alpha_5 = \alpha_6 = 0.04$, and $\alpha_7 = \alpha_8 = 0.008$. We still want the total rate out of the MLFS state to equal $\Gamma_{zr}$, so we normalize the weighting factors:

$$\alpha_{i normalized} = \frac{\alpha_i}{\sum_{i=1}^{2J} \alpha_i} \tag{2.39}$$

The previous models are recovered by setting all $\alpha_i$ equal to 1 or by setting only

$\alpha_1 = 1$ with all other $\alpha_i = 0$. We will drop the *normalized* subscript on $\alpha_i$, but normalization is implied. Incorporating these factors into Equation (2.31) leads to

$$\dot{n}_{m_J} = -\Gamma_{zr} \sum_{m_J{}' < m_J} \alpha_i n_{m_J} + \frac{\Gamma_{zr}}{2J} \sum_{m_J{}' > m_J} \alpha_i n_{m_J{}'}. \tag{2.40}$$

$$\dot{n}_{MLFS}(t = 0) = -\Gamma_{zr} n_0 \sum_{i=1}^{2J} \alpha_i = -\Gamma_{zr} n_0 \tag{2.41}$$

$$\dot{n}_{MHFS}(t = 0) = \Gamma_{zr} n_0 \sum_{i=1}^{2J} \alpha_i = \Gamma_{zr} n_0 \tag{2.42}$$

The first term in every summation is multiplied by $\alpha_1$, the second term by $\alpha_2$, etc. The Zeeman cascade behavior assuming the transition rates in Table 2.1 is plotted in Figure 2-4. The approach to equilibrium falls between the two extremes; it is faster than the case when all transition rates are equal, but slower than when $\Delta m_J = \pm 1$.

### 2.3.3 Zeeman cascade with thermal excitation

In the previous section we assumed that inelastic collisions only transfer atomic population to lower energy states. This is true only when thermal energy $k_B T$ is much less than magnetic energy $g_J \mu_B B$. At finite temperature the kinetic energy of colliding atoms can supply the energy needed to repopulate higher energy Zeeman states. Ideally, experimental conditions are met that make thermal effects negligible. This can be done in principle by making all measurements at sufficiently high magnetic field strengths. However, this is not always possible. Magnetic broadening of the absorption lines used to measure MLFS lifetimes leads to a decrease in peak absorption. This effect gets worse as the field strength increases. In order to have sufficient signal to make the measurement we could not operate at fields where thermal effects are negligible. We therefore must include thermal excitations in our analysis of MLFS decay.

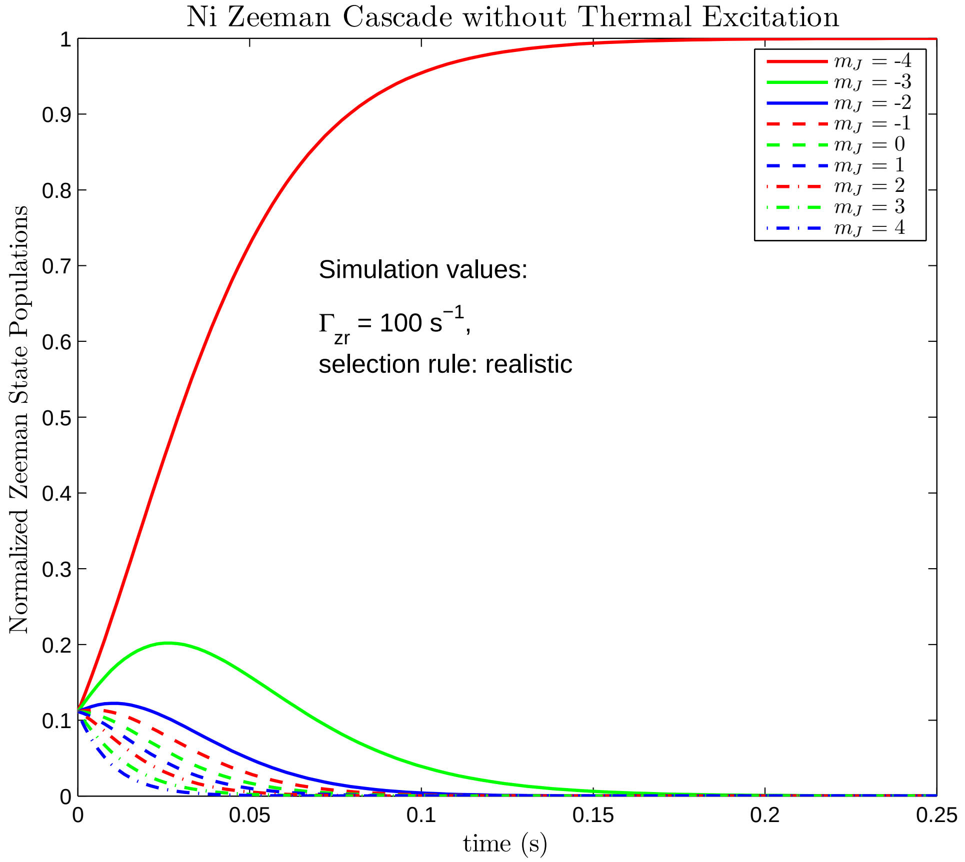

Simulation values:

$\Gamma_{zr}$ = 100 $s^{-1}$,
selection rule: realistic

Figure 2-4: Nickel Zeeman cascade without thermal excitation assuming the realistic selection rules listed in Table 2.1. The MLFS state relaxation rate is $\Gamma_{zr} = 100\, s^{-1}$. The approach to steady state is faster than the case when all transition rates are equal, but slower than the case when $\Delta m_J = \pm 1$.

In thermal equilibrium at temperature $T$ the density of an $m_J$ level $n_{m_J} \propto exp(-(E_{m_J})/(k_B T))$. Thus the density ratio for two Zeeman states $m_J$ and $m_J{}'$ is

$$\frac{n_{m_J}}{n_{m_J{}'}} = exp(-(E_{m_J} - E_{m_J{}'})/(k_B T)) \tag{2.43}$$

In thermal equilibrium it must also be true that all Zeeman populations reach a steady state value, i.e. $\dot{n}_{m_J} = 0$. We incorporate both of these requirements by adding additional terms to (2.31) and (2.34 - 2.36). For each Zeeman level we add a loss term describing thermal excitation to higher Zeeman states and a gain term describing thermal excitation from lower Zeeman states. Due to the energy barrier, the probability to excite to a higher state is less than the probability to relax to a lower energy state. The excitation rate is suppressed relative to the relaxation rate by the ratio of the Boltzmann factors of the states involved. Explicitly, the excitation rate $\Gamma_{ex}$ to drive a transition from an $m_J$ state to a higher energy ${m_J}'$ state is

$$\Gamma_{ex} \propto \Gamma_{zr}\, exp(-(E_{{m_J}'} - E_{m_J})/(k_B T)). \tag{2.44}$$

The proportionality constant is set by the assumed selection rules.

### Assumption: all relaxation rates equal

When thermal excitations are added the dynamics, (2.31) becomes

$$\begin{aligned} \dot{n}_{m_J} = &-\frac{\Gamma_{zr}}{2J}\left(\sum_{{m_J}'<m_J} n_{m_J} + \sum_{{m_J}'>m_J} n_{m_J} exp\left(-\frac{(E_{{m_J}'} - E_{m_J})}{k_B T}\right)\right) \\ &+\frac{\Gamma_{zr}}{2J}\left(\sum_{{m_J}'>m_J} n_{{m_J}'} + \sum_{{m_J}'<m_J} n_{{m_J}'} exp\left(-\frac{(E_{m_J} - E_{{m_J}'})}{k_B T}\right)\right). \end{aligned} \tag{2.45}$$

By inserting (2.43), our first condition for thermal equilibrium, into (2.45) it can be shown that our second condition for thermal equilibrium, $\dot{n} = 0$, is also met.

Figure 2-5 shows the evolution of nickel Zeeman states with $\Gamma_{zr} = 100\, s^{-1}s$, $T = 1K$, and $B = 0.8T$.[5] Under these conditions the ratio of Boltzmann factors for adjacent Zeeman states is only $\sim 1/2$ and thermal effects will be significant. Figure 2-5 makes this clear since now only about half of the atoms are in the MHFS stretched state as $t \rightarrow \infty$. Thermal excitations distribute population amongst all Zeeman states. The ratio of $m_J = 4$ to $m_J = -4$ populations is 4.6%. The initial decay of the MLFS state and growth of the MHFS state are slowed by the effects of repopulation.

---

[5] Recall from (2.10) that the Zeeman energies equal $g_J m_J \mu_B B$. The nickel g factor $g_J = 1.25$ and $J = 4$.

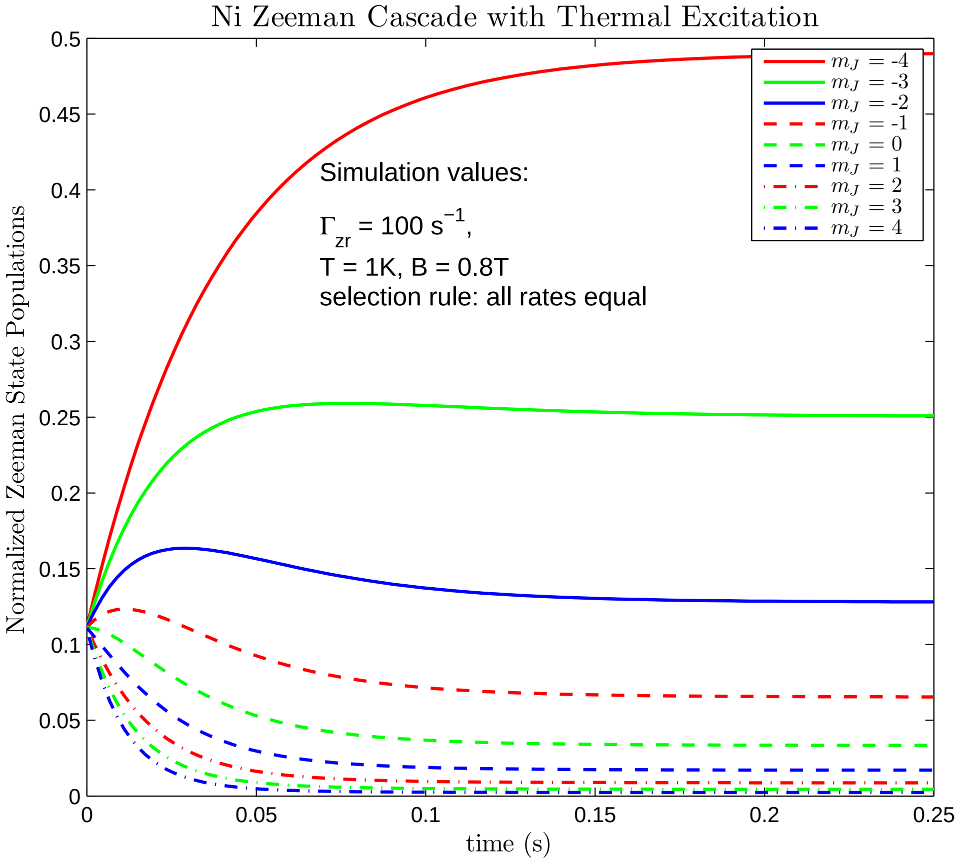

Figure 2-5: Nickel Zeeman cascade with thermal excitation at $T = 1K, B = 0.8T$ assuming equal Zeeman relaxation rates for all transitions and a rate of $100\,s^{-1}$ for the MLFS state. When thermal repopulation occurs in addition to Zeeman relaxation, the Zeeman populations obey a Boltzmann distribution as $t \to \infty$.

The expressions for MLFS state loss and MHFS growth at t = 0 can be put in a simple form by defining $E_{m_J} - E_{m_J'} = g_J \mu_B B \Delta m_J = E \Delta m_J$. The resulting t = 0 behavior is

$$\dot{n}_{MLFS}(t=0) = -\Gamma_{zr} n_0 \left(1 - \frac{1}{2J} \sum_{\Delta m_{J=1}}^{2J} (exp(-E/(k_B T)))^{\Delta m_J}\right) \tag{2.46}$$

$$\dot{n}_{MLFS}(t=0) = \Gamma_{zr} n_0 \left(1 - \frac{1}{2J} \sum_{\Delta m_{J=1}}^{2J} (exp(-E/(k_B T)))^{\Delta m_J}\right) \tag{2.47}$$

The MLFS state decays at a slower rate than when collisional excitations were ignored. For 1K nickel atoms in a 0.8T field, the apparent relaxation rate is now $0.87\Gamma_{zr}$, a 13 % decrease. A measurement of $\tau_{MLFS}$ under these conditions is an overestimate of $\tau_{ZR} = 1/\Gamma_{zr}$. Since $\gamma$ is the ratio of the elastic to inelastic collision cross sections and $\Gamma_{zr} \propto \sigma_{zr}$, ignoring thermal effects leads to an overestimate of $\gamma$.

**Assumption: selection rule $\Delta m_J = \pm 1$**

For the simpler case with relaxation obeying $\Delta m_J = \pm 1$, thermal effects connect only adjacent levels.

$$\dot{n}_{m_J} = -\Gamma_{zr}\left(n_{m_J} - n_{m_J-1}e^{(\frac{-g_J\mu_B B}{k_B T})}\right) \qquad \text{for } m_J = J, \tag{2.48}$$

$$\begin{aligned} \dot{n}_{m_J} &= -\Gamma_{zr}\left(n_{m_J} + n_{m_J}e^{(\frac{-g_J\mu_B B}{k_B T})}\right) + \\ &+ \Gamma_{zr}\left(n_{m_J-1}e^{(\frac{-g_J\mu_B B}{k_B T})} + n_{m_J+1}\right) \qquad \text{for } m_J \neq J, -J, \end{aligned} \tag{2.49}$$

$$\dot{n}_{m_J} = \Gamma_{zr}\left(n_{m_J+1} - n_{m_J}e^{(\frac{-g_J\mu_B B}{k_B T})}\right) \qquad \text{for } m_J = -J, \tag{2.50}$$

$$\dot{n}_{MLFS}(t=0) = -\Gamma_{zr}n_0\left(1 - exp(-(E/k_B T))\right), \tag{2.51}$$

$$\dot{n}_{MHFS}(t=0) = \Gamma_{zr}n_0\left(1 - exp(-(E/k_B T))\right). \tag{2.52}$$

Figure 2-6 shows the thermal effects on this model. The nickel MLFS state apparent relaxation rate is now 0.49 $\Gamma_{zr}$, approximately 1/2 of its true value. Any measured value of $\tau_{zr}$ will be a factor of two off from the true value of the Zeeman relaxation lifetime. It takes longer to reach a steady state thermal distribution compared to the previous model because the initial decay and growth rates are smaller.

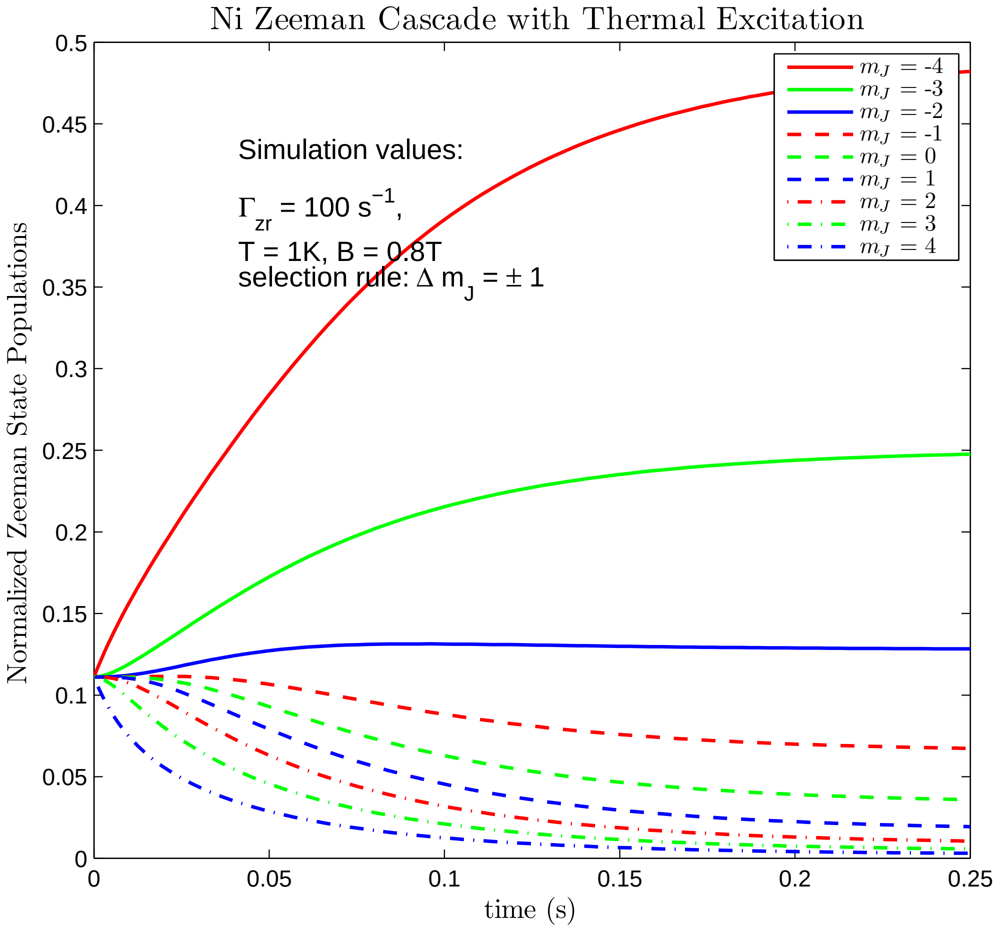

Figure 2-6: Nickel Zeeman cascade with thermal excitation at $T = 1K, B = 0.8T$ assuming $\Delta m_J = \pm 1$ and a Zeeman relaxation rate of $100\, s^{-1}$. The t = 0 decay rate of the MFLS state has decreased by a factor of two from the true Zeeman relaxation rate. The approach to thermal equilibrium is slower than the case where all Zeeman transition rates are assumed to be equal because the initial decay and growth rates are lower.

**Assumption: realistic selection rules**

The equations governing Zeeman state dynamics are found by inserting an $\alpha_i$ into each summation in (2.45).

$$\begin{aligned}\dot{n}_{m_J} = -\Gamma_{zr}&\left(\sum_{{m_J}'<m_J}\alpha_i n_{m_J} + \sum_{{m_J}'>m_J}\alpha_i n_{m_J} exp\left(-\frac{(E_{m_J'}-E_{m_J})}{k_B T}\right)\right)\\ +\Gamma_{zr}&\left(\sum_{{m_J}'>m_J}\alpha_i n_{m_J'} + \sum_{{m_J}'<m_J}\alpha_i n_{m_J'} exp\left(-\frac{(E_{m_J}-E_{m_J'})}{k_B T}\right)\right).\end{aligned} \tag{2.53}$$

The the t = 0 decay and growth rates for the MLFS and MHFS states are

$$\dot{n}_{MLFS}(t=0) = -\Gamma_{zr}n_0\left(1-\sum_{\Delta m_{J=1}}^{2J}\alpha_i(exp(-E/(k_BT)))^{\Delta m_J}\right) \tag{2.54}$$

$$\dot{n}_{MLFS}(t=0) = \Gamma_{zr}n_0\left(1-\sum_{\Delta m_{J=1}}^{2J}\alpha_i(exp(-E/(k_BT)))^{\Delta m_J}\right) \tag{2.55}$$

As in the other models, the t = 0 decay rate out of the MLFS state has been changed from the actual Zeeman relaxation rate. For 1K nickel atoms in a 0.8T field the apparent MLFS Zeeman relaxation rate is now 0.67 $\Gamma_{zr}$. The behavior falls somewhere between the two extreme cases presented earlier. Figure 2-7 shows the full Zeeman Cascade approach to thermal equilibrium.

### 2.3.4 Zeeman casacade with diffusion loss

In addition to Zeeman state changing collisions, all Zeeman levels experience diffusion loss to the cell walls as described in Section 2.2. Including this loss results in the most accurate picture of the MLFS and MHFS dynamics of the atoms in our cell. Again, we consider the three selection rule cases.

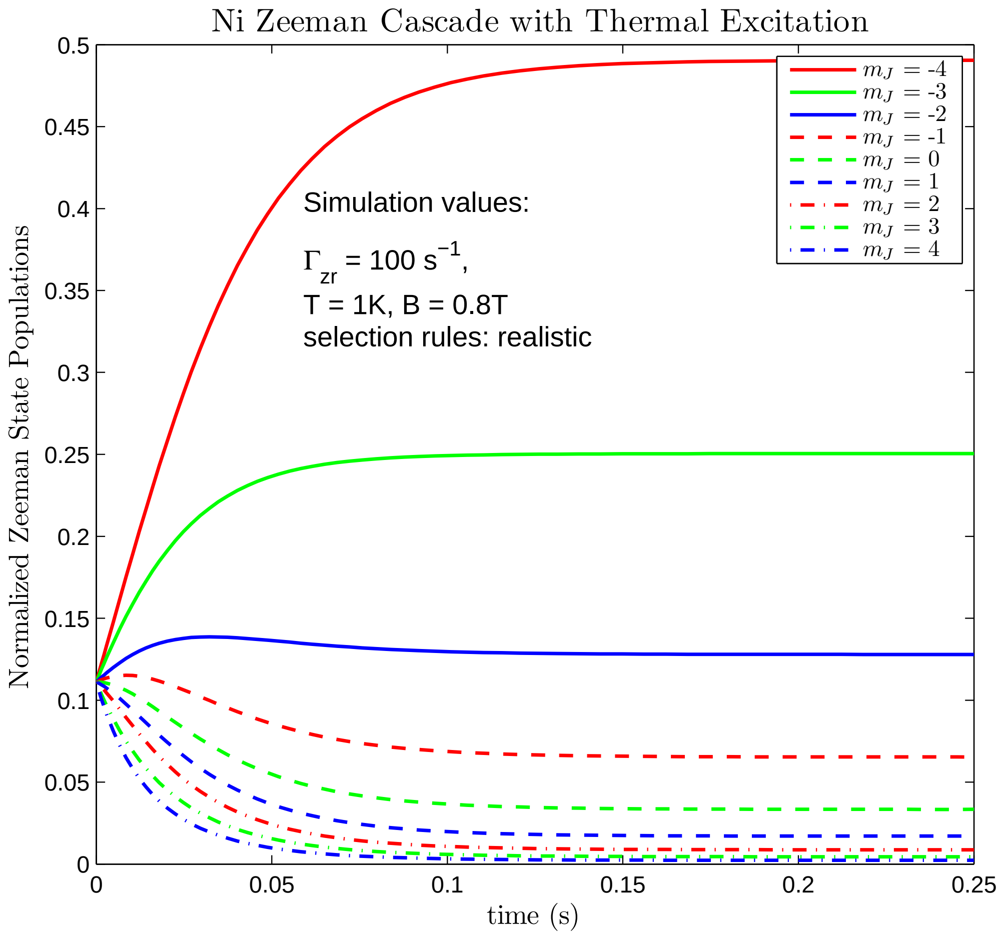

Figure 2-7: Nickel Zeeman cascade with thermal excitation assuming realistic selection rules listed in Table 2.1. The atoms are at $T = 1K, B = 0.8T$. The MLFS state relaxation rate is $\Gamma_{zr} = 100\, s^{-1}$. The t = 0 decay rate of the MFLS state is now $\sim 2/3$ $\Gamma_{zr}$. The approach to thermal equilibrium is faster than the case when $\Delta m_J = \pm 1$, but slower than the case when all transition rates are equal.

### Complete dynamics assuming all relaxation rates are equal

Adding a loss rate $-\Gamma_d\, n_{m_J}$ to Equations (2.45) yields

$$\begin{aligned}\dot{n}_{m_J} = -\Gamma_d\, n_{m_J} - \frac{\Gamma_{zr}}{2J}\left(\sum_{m_J{}' < m_J} n_{m_J} + \sum_{m_J{}' > m_J} n_{m_J} exp\left(-\frac{(E_{m_J{}'} - E_{m_J})}{k_B T}\right)\right) \\ + \frac{\Gamma_{zr}}{2J}\left(\sum_{m_J{}' > m_J} n_{m_J{}'} + \sum_{m_J{}' < m_J} n_{m_J{}'} exp\left(-\frac{(E_{m_J} - E_{m_J{}'})}{k_B T}\right)\right).\end{aligned} \tag{2.56}$$

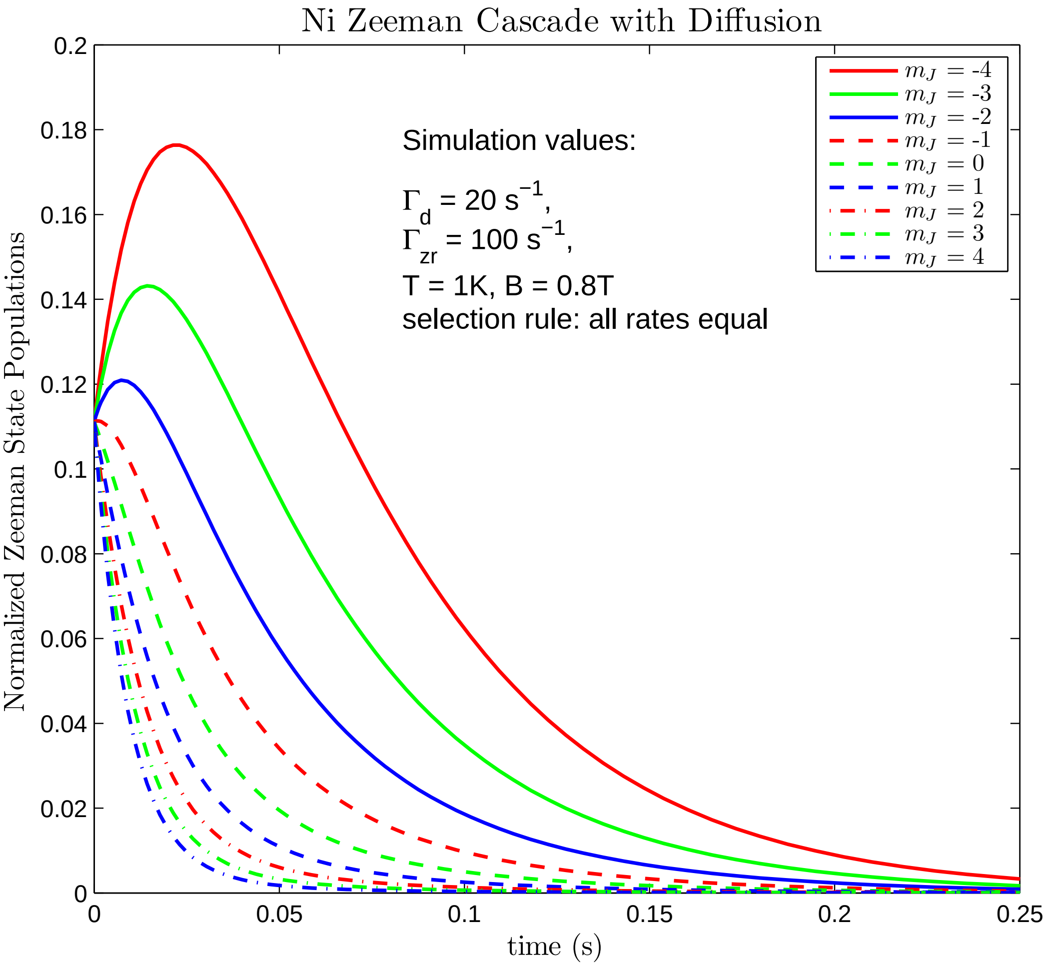

Figure 2-8: Nickel Zeeman cascade at $T = 1K, B = 0.8T$ assuming Zeeman relaxation rates are equal for all transitions. The MLFS decay at $\Gamma_{zr} = 100\,s^{-1}$ and the diffusion rate is $20\,s^{-1}$. A thermal distribution is established as the atoms diffuse to the cell walls.

Figure 2-8 shows nickel Zeeman state density evolution assuming $\Gamma_{zr} = 100\,s^{-1}$, $\Gamma_d = 20\,s^{-1}$, $T = 1K$ and $B = 0.8T$. After a thermal distribution has been established via Zeeman relaxation all states decay with a lifetime $\tau_d = 1/\Gamma_d$. The $m_J = -J$ state has the largest number of source terms since Zeeman relaxation from all higher levels feed its population growth. As a result, it takes the longest time to exhibit simple diffusion to the walls. The initial decay from the MLFS state and growth into the MHFS state are

$$\dot{n}_{MLFS}(t=0) = -n_0\left(\Gamma_d + \Gamma_{zr}\left(1 - \frac{1}{2J}\sum_{\Delta m_{J=1}}^{2J}(exp(-E/(k_BT)))^{\Delta m_J}\right)\right) \quad (2.57)$$

$$\dot{n}_{MLFS}(t=0) = n_0\left(\Gamma_d + \Gamma_{zr}\left(1 - \frac{1}{2J}\sum_{\Delta m_{J=1}}^{2J}(exp(-E/(k_BT)))^{\Delta m_J}\right)\right). \quad (2.58)$$

For 1K nickel atoms in a 0.8T field the apparent decay rate for the MLFS is $\Gamma_d + 0.87\Gamma_{zr}$. When the diffusion rate is much higher than the Zeeman relaxation rate, thermal effects will not alter the observed behavior appreciably. Thermal effects only become important when the time scale for Zeeman relaxation lifetime is less than the diffusion lifetime.

**Complete dynamics assuming relaxation rates obey selection rule $\Delta m_J = \pm 1$**

Adding a loss rate of $\Gamma_d n_{m_J}$ to (2.48 - 2.49) yields

$$\begin{aligned}
\dot{n}_{m_J} &= -\Gamma_d\, n_{m_J} - \Gamma_{zr}\left(n_{m_J} - n_{m_J-1}e^{(\frac{-g_J\mu_B B}{k_BT})}\right) && \text{for } m_J = J, && (2.59)\\
\dot{n}_{m_J} &= -\Gamma_d\, n_{m_J} - \Gamma_{zr}\left(n_{m_J} + n_{m_J}e^{(\frac{-g_J\mu_B B}{k_BT})}\right) && && \\
&\quad + \Gamma_{zr}\left(n_{m_J-1}e^{(\frac{-g_J\mu_B B}{k_BT})} + n_{m_J+1}\right) && \text{for } m_J \neq J, -J, && (2.60)\\
\dot{n}_{m_J} &= -\Gamma_d\, n_{m_J} + \Gamma_{zr}\left(n_{m_J+1} - n_{m_J}e^{(\frac{-g_J\mu_B B}{k_BT})}\right) && \text{for } m_J = -J, && (2.61)
\end{aligned}$$

$$\dot{n}_{MLFS}(t=0) = -n_0\left(\Gamma_d + \Gamma_{zr}\left(1 - exp(-(E/k_BT))\right)\right), \quad (2.62)$$

$$\dot{n}_{MHFS}(t=0) = n_0\left(\Gamma_d + \Gamma_{zr}\left(1 - exp(-(E/k_BT))\right)\right). \quad (2.63)$$

The MLFS t = 0 apparent loss rate for 1K atoms in a 0.8T field is now $\Gamma_d$+$0.49\Gamma_{zr}$. As with the previous model, thermal effects are unimportant until the Zeeman relaxation rate $\geq$ the diffusion rate.

A comparison of Figure 2-9 and Figure 2-8 shows significant differences between

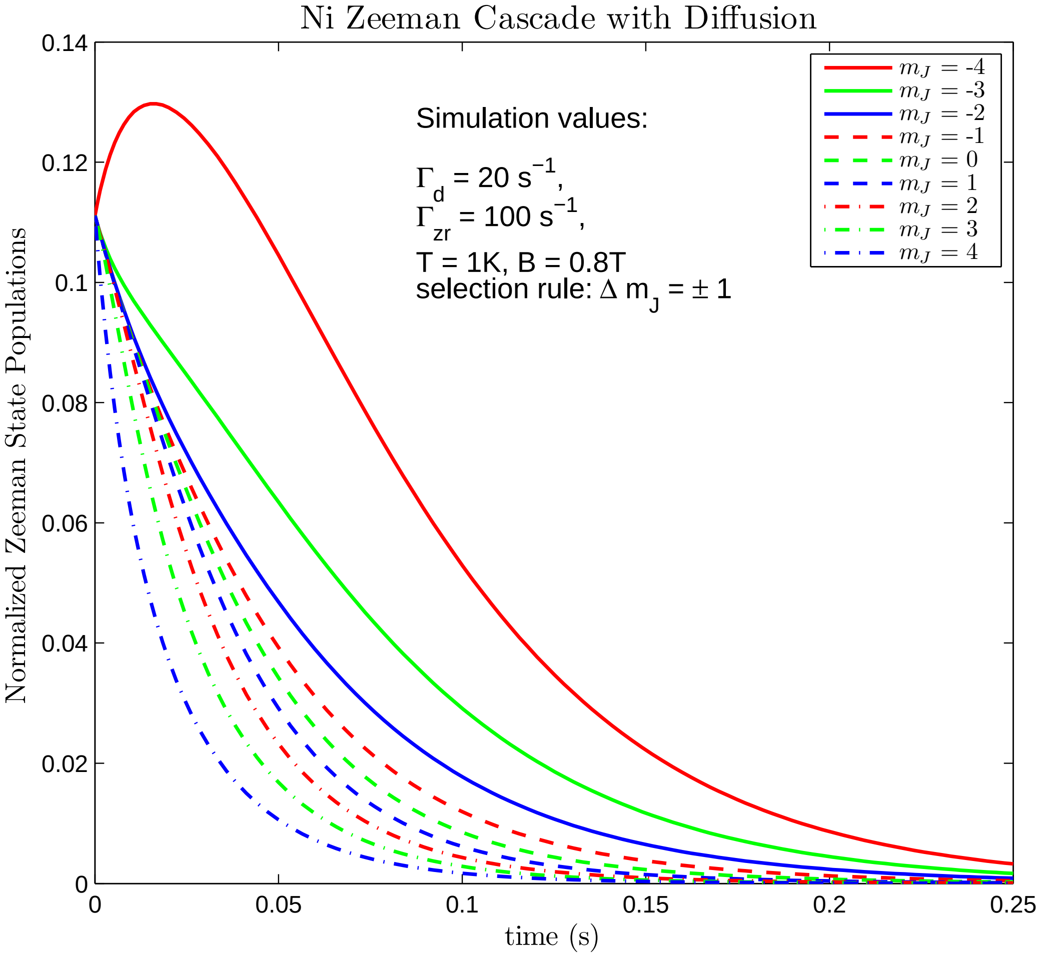

Figure 2-9: Nickel Zeeman cascade with thermal excitation and diffusion at $T = 1K, B = 0.8T$. The MLFS state relaxation rate is $\Gamma_{zr} = 100\,s^{-1}$ and the diffusion rate is $20\,s^{-1}$. A thermal distribution is established as the atoms diffuse to the cell walls. Initially the MHFS state population grows. After several Zeeman relaxation lifetimes MHFS atoms diffuse to the wall at the diffusion rate.

Zeeman state dynamics depending on the assumed selection rules. Assuming $\Delta m_J = \pm 1$, all states other than $m_J = -J$ immediately decay. Assuming all Zeeman transition rates are equal, high-field seeking states experience population growth before diffusion losses induce decay.

### Complete dynamics assuming realistic relaxation rates

The behavior for realistic selection rules will again fall between the two extremes. The complete dynamics are described by

$$
\begin{aligned}
\dot{n}_{m_J} = -\Gamma_d\, n_{m_J} - \Gamma_{zr} & \left( \sum_{{m_J}'<m_J} \alpha_i n_{m_J} + \sum_{{m_J}'>m_J} \alpha_i n_{m_J} exp\left(-\frac{(E_{{m_J}'} - E_{m_J})}{k_B T}\right)\right) \\
& + \Gamma_{zr} \left( \sum_{{m_J}'>m_J} \alpha_i n_{{m_J}'} + \sum_{{m_J}'<m_J} \alpha_i n_{{m_J}'} exp\left(-\frac{(E_{m_J} - E_{{m_J}'})}{k_B T}\right)\right),
\end{aligned}
\tag{2.64}
$$

with the following MLFS and MHFS behavior at t = 0:

$$
\dot{n}_{MLFS}(t=0) = -n_0 \left( \Gamma_d + \Gamma_{zr} \left( 1 - \sum_{\Delta m_{J=1}}^{2J} \alpha_i (exp(-E/(k_B T)))^{\Delta m_J} \right)\right) \tag{2.65}
$$

$$
\dot{n}_{MLFS}(t=0) = n_0 \left( \Gamma_d + \Gamma_{zr} \left( 1 - \sum_{\Delta m_{J=1}}^{2J} \alpha_i (exp(-E/(k_B T)))^{\Delta m_J} \right)\right) \tag{2.66}
$$

For 1K atoms in a 0.8T field the apparent MLFS Zeeman relaxation rate is now $\Gamma_d + 0.67\Gamma_{zr}$. Figure 2-10 shows a Zeeman Cascade with diffusion losses for the case of realistic selection rules.

We measure both the MLFS state and MHFS state population evolutions to make our measurements of $\gamma$. The following sections summarize the effect of the Zeeman Cascade on these states.

### 2.3.5 Zeeman cascade effects on MHFS dynamics

MHFS atoms do not simply diffuse to the walls. At early times the population increases as atoms from higher energy Zeeman states decay into the MHFS state. However, after 8-9 Zeeman relaxation lifetimes a diffusion model for MHFS dynamics is good at the 10% level. Figure 2-11 plots a Zeeman Cascade simulation of MHFS decay along with a simple diffusion loss model. The agreement is excellent after the first 100 ms.

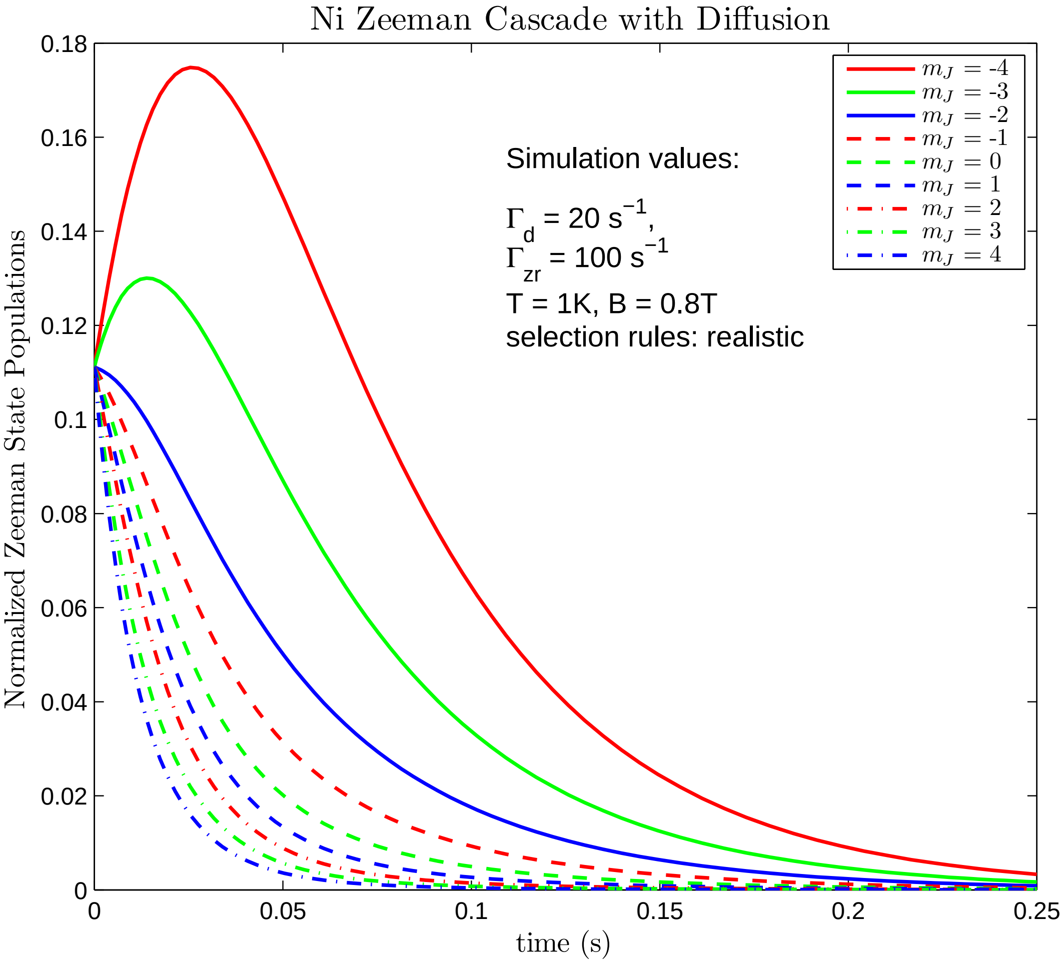

Figure 2-10: Nickel Zeeman cascade with thermal excitation and diffusion assuming realistic selection rules listed in Table 2.1. The atoms are at $T = 1K$ and $B = 0.8T$. The MLFS state relaxation rate is $\Gamma_{zr} = 100\,s^{-1}$ and the diffusion rate is $20\,s^{-1}$. The behavior falls somewhere between the two extreme cases previously discussed. Only the two most high field seeking states experience growth; all other states begin to decay immediately.

### 2.3.6 Thermal effects on MLFS dynamics

A close examination of thermal effects on MLFS state dynamics is crucial to understand experimental measurements of MLFS lifetime. Thermal excitation of atoms from lower Zeeman states to the MLFS state causes the MLFS decay rate to deviate from the simple model presented in Section 2.2. In addition, the assumptions regarding selection rules for Zeeman relaxation alter the predicted behavior.

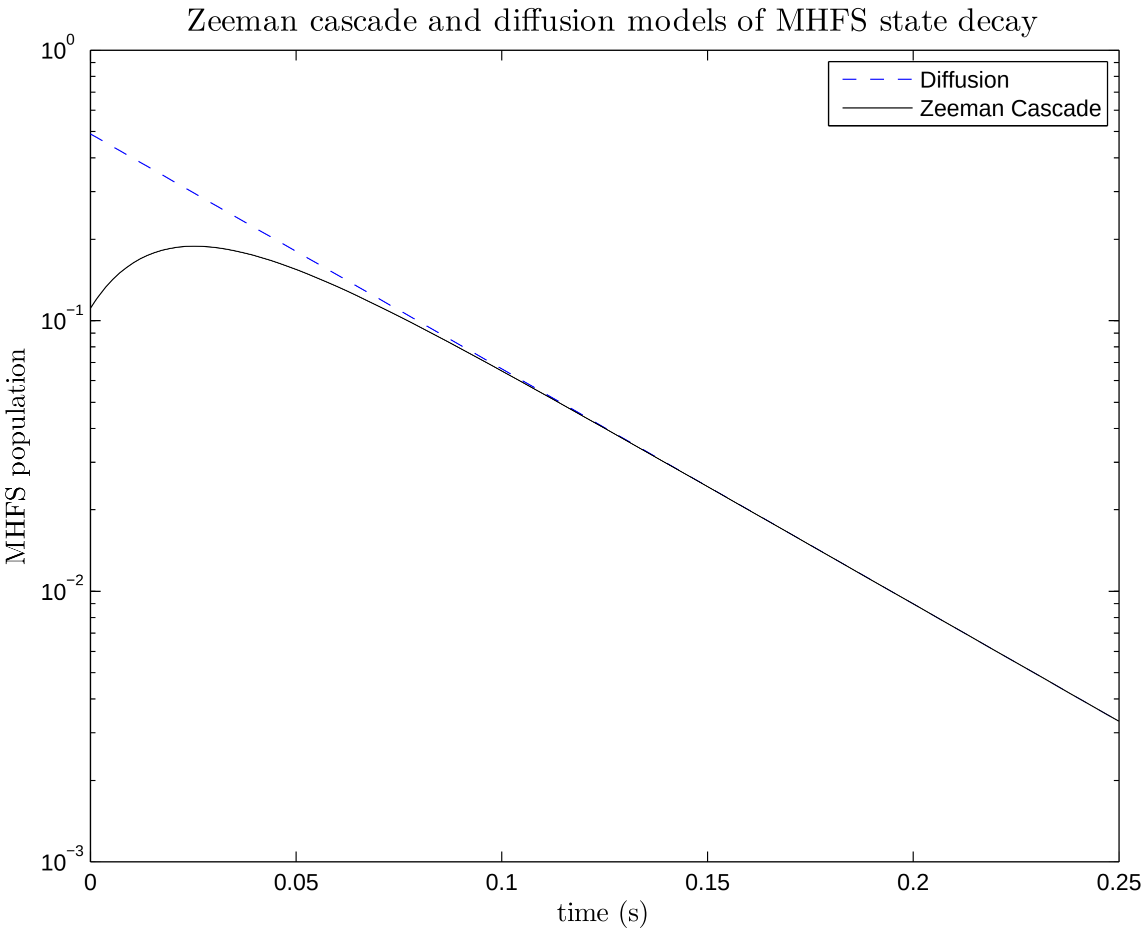

Figure 2-11: The MHFS Zeeman Cascade simulation is plotted with a simple diffusion model. After 7-8 Zeeman relaxation lifetimes diffusion describes the MHFS decay to an accuracy of better than 10 %. The selection rules assume all Zeeman relaxation rates are equal. For $\Delta m_J = \pm 1$ selection rules it takes 12-13 zeeman relaxtion times to reach the 10 % agreement level.

The MLFS atoms initially decay via a combination of Zeeman relaxation and diffusion. After many Zeeman relaxation lifetimes a thermal population of MLFS atoms is established which decays at the diffusion rate alone. The dominant effect of thermal excitation on MLFS atoms is an alteration of their initial decay. After ablation all Zeeman states are equally populated. Thus the thermal excitation rate at $t = 0$ is nonzero and counteracts the MLFS atom loss caused by Zeeman relaxation and diffusion. This causes the initial MLFS state decay rate to be lower than the intrinsic rate, which would apply at $T << (g_J \mu_B B)/k_B$. This increase in MLFS lifetime can be misinterpreted as a decrease in the Zeeman relaxation rate. This error in judgement results in an underestimate of the inelastic collision cross section and a subsequent overestimate of $\gamma$. For our experimental conditions of $\sim$ 1K atoms in a 0.8 Tesla magnetic field the effect can change the apparent Zeeman relaxation lifetime by as much as 50 %.

The $m_J = J - 1$ state most efficiently thermally populates the $m_J = J$ MLFS state because it is the nearest energy state. All lower Zeeman levels will thermally excite into the $m_J = J$ state, but the ratio of Boltzmann factors between $m_J = J$ and $m_J = J - 1$ is the smallest, so thermal excitation is strongest for this transition. The transition rate between the $m_J = J$ and $m_J = J - 1$ states is largest when we assume $\Delta m_J = \pm 1$ for Zeeman relaxation. Therefore thermal effects are largest for $\Delta m_J = \pm 1$ selection rules. As the $m_J = J - 1$ population decays via Zeeman relaxation and diffusion, the thermal excitation rate into the $m_J = J$ state decreases. If $\Delta m_J = \pm 1$, the $m_J = J - 1$ atoms relax at a lower rate (see Figure 2-6) and thermal effects are more dramatic. If all relaxation rates are assumed to be equal, a direct path to all lower energy states is open. In this case the relaxation of the $m_J = J - 1$ state is more rapid (see Figure 2-5) and thermal effects are less pronounced. A clear differentiation between the two assumptions is demonstrated in Figure 2-12. The MLFS lifetime is clearly longer when $\Delta m_J = \pm 1$ is enforced. The MLFS decay for the more realistic selection rule assumption is also plotted and falls between the two extreme cases. This is a graphic representation of Equations (2.57), (2.62), and (2.65).

We compare the Zeeman cascade simulation with our experimental observations of MLFS state decay by treating the simulation as if it were data. Experimental MLFS lifetimes are measured by fitting the decay of the MLFS resonant absorption signal to an exponential curve (see Section 3.3.5 for more details). Simulated MLFS decay can be fit to exponential lifetimes in an identical manner. Repeating the simulation for several temperatures and fitting the results to an exponential decay makes it possible to quantify the change in predicted $\tau_{MLFS}$ as a function of temperature. Figure 2-13 shows the result for the three selection rule assumptions discussed above. For the parameters of the simulation, thermal excitation changes $\tau_{MLFS}$ appreciably at temperatures above 200 mK for $\Delta m_J = \pm 1$ while the effect does not become

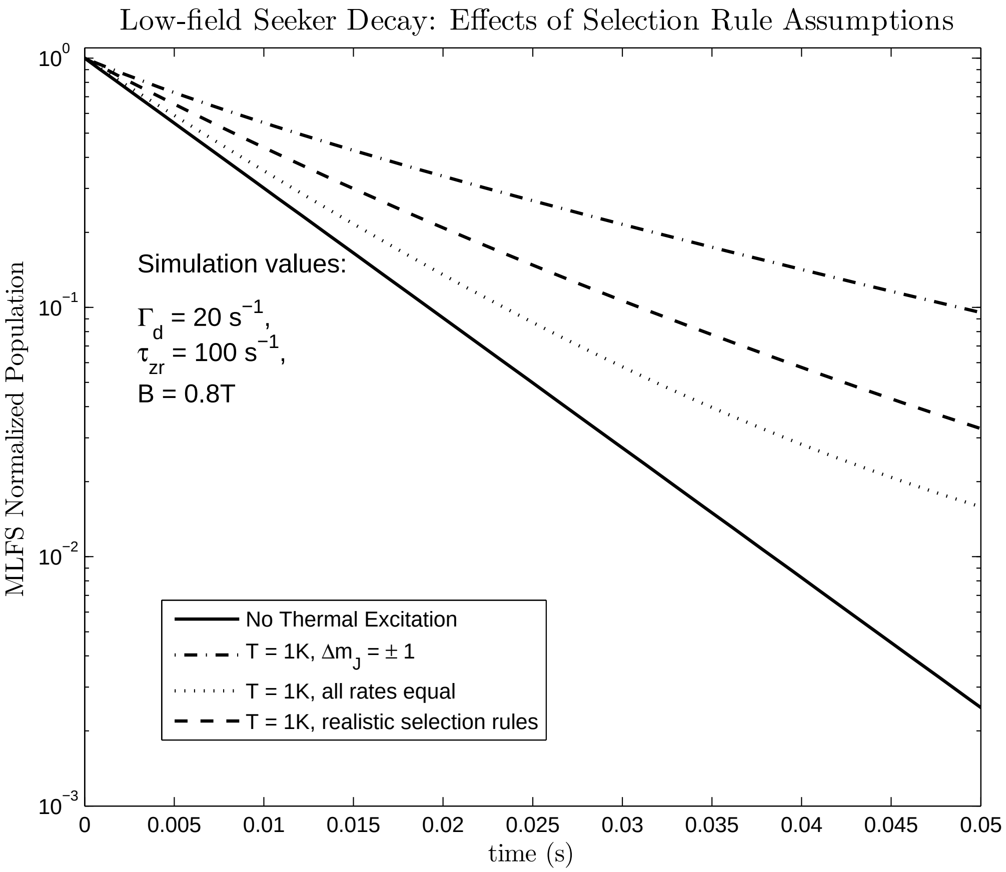

Figure 2-12: Effects of Zeeman relaxation selection rule assumptions on MLFS lifetime. At finite temperature, the selection rule $\Delta m_J = \pm 1$ clearly predicts the slowest decay for MLFS atoms.

significant until $T > 1K$ when the Zeeman relaxation rates are assumed to be equal for all transitions.

When diffusion losses dominate MLFS state dynamics thermal excitations do not play an important role; collisional excitations do not prevent atoms from diffusing to the walls. We therefore expect thermal effects to play their largest role when the diffusion lifetime is much larger than the observed MLFS lifetime. When $\tau_d$ becomes longer than $\tau_{zr}$, the dynamics are dominated by Zeeman relaxation. Thermal excitations alter MLFS dynamics as described in the previous sections. At very high buffer gas densities $\tau_d$ gets much longer than $\tau_{zr}$. In this regime care must be taken to properly interpret the measured decay of the MLFS atoms. We introduce atoms into the cell via laser ablation of metallic samples. We typically wait 5-10 ms to

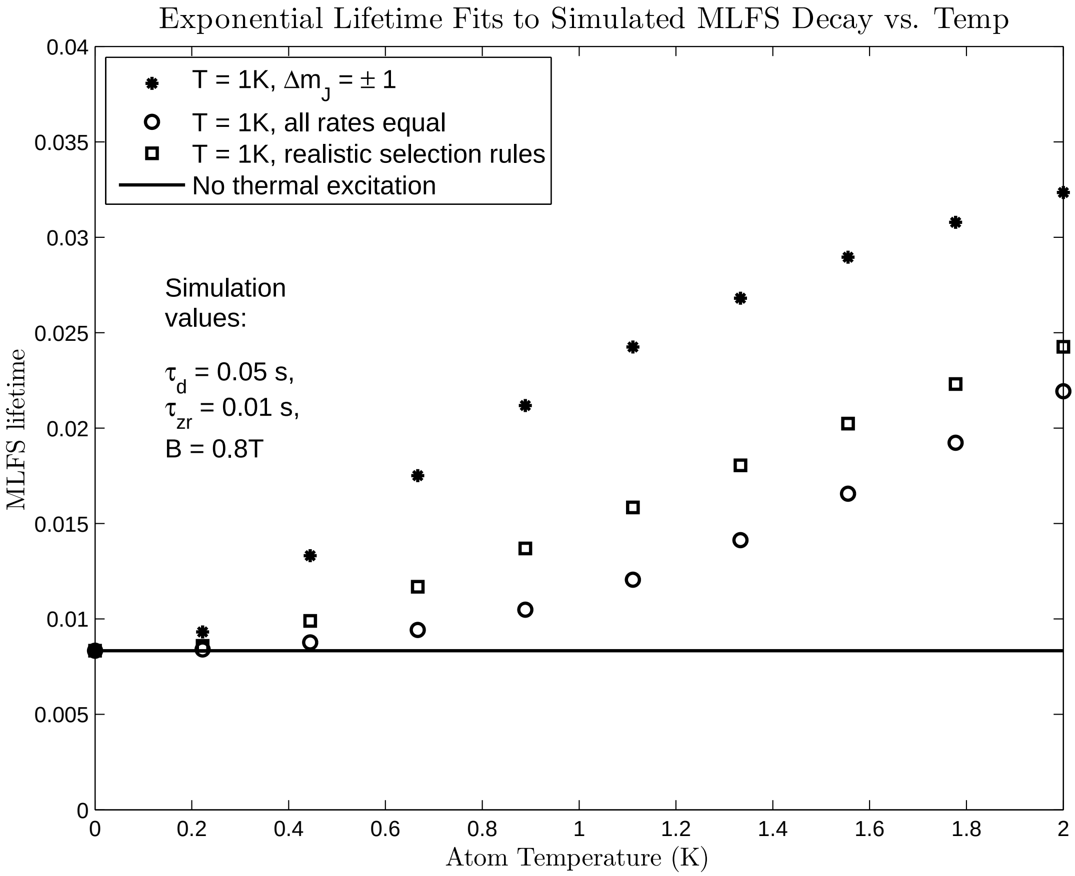

Figure 2-13: Temperature dependence of simulated nickel MLFS lifetimes. For $\Delta m_J = \pm 1$ Zeeman relaxation the predicted deviation from zero temperature behavior becomes apparent for temperatures below $1K$. The effect is clear but less dramatic when all transitions rates are assumed to be equal. Realistic selection rule behavior falls between the two extremes.

make sure the sample is fully thermalized and measure MLFS decay in the time window between 10 ms and 50 ms after ablation. If the Zeeman relaxation timescale is faster than 5-10 ms, the approach of the sample toward thermal equilibrium will be rapid. In thermal equlibrium the MLFS sample will decay at the diffusion rate. It is possible that by the time we start measuring the MLFS decay we are no longer measuring pure Zeeman relaxation behavior but a mixture of Zeeman relaxation and diffusion. This causes an apparent decrease in the MLFS decay rate compared to pure Zeeman relaxation rate. We therefore cannot measure Zeeman relaxation rates at values of $\tau_d$ corresponding to very high buffer gas densities. The limiting value of $\tau_d$ depends on which selection rule for Zeeman relaxation is assumed. The worst case scenario occurs when all Zeeman translation rates are equal because thermal equilibrium is established most rapidly. Figure 2-14 demonstrates how increasing $\tau_d$ leads to a deceptive measurement of $\tau_{MLFS}$. The effect is much less drastic when realistic selection rules are used, but it is possible that MLFS decay rates measured at our highest values of $\tau_d$ are perturbed by this effect.

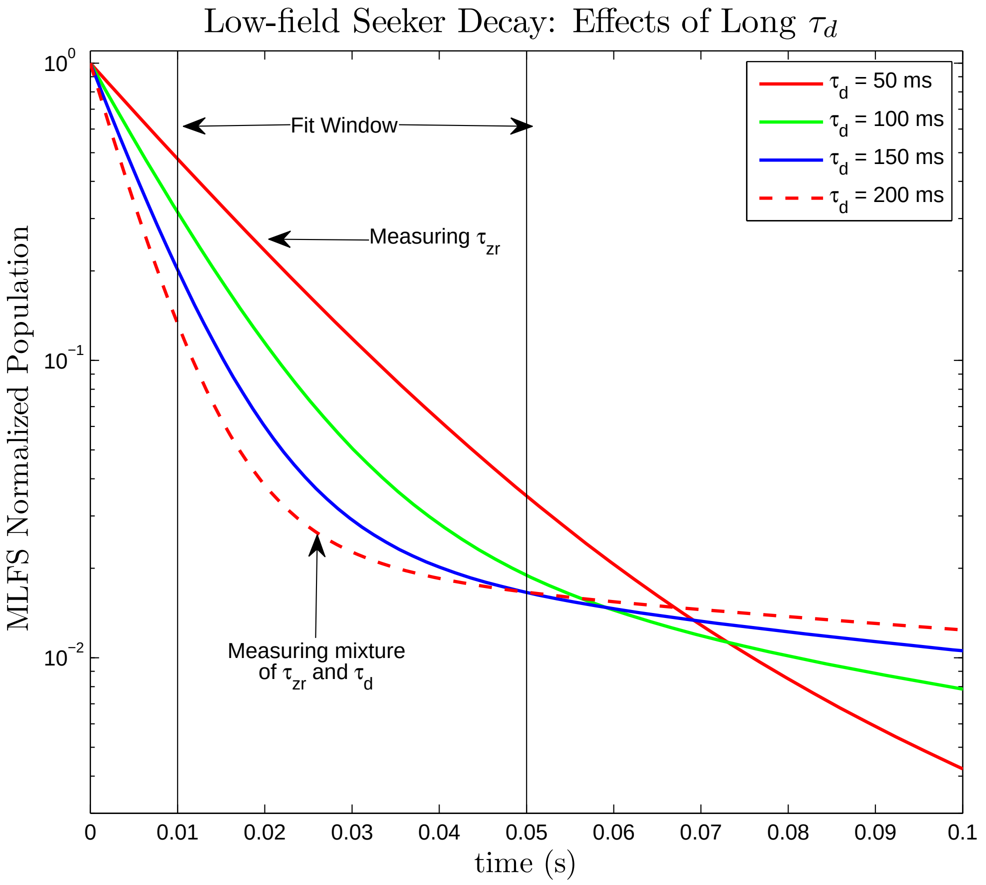

Figure 2-14: At high values of $\tau_d$ Zeeman relaxation occurs rapidly. As the sample approaches thermal equilibrium the measured decay of the MLFS state becomes a combination of Zeeman relaxation and diffusion. The worst case scenario occurs when all Zeeman transition rates are equal because the approach to thermalization is most rapid.

As described in Section 2.2, in order to determine $\gamma$ without a direct knowledge of the buffer gas density we must make a series of measurements of $\tau_{MLFS}$ vs. $\tau_d$. It is worthwhile to examine the expected effects of collisional excitation on these measurements by using our Zeeman Cascade model to simulate a data set.

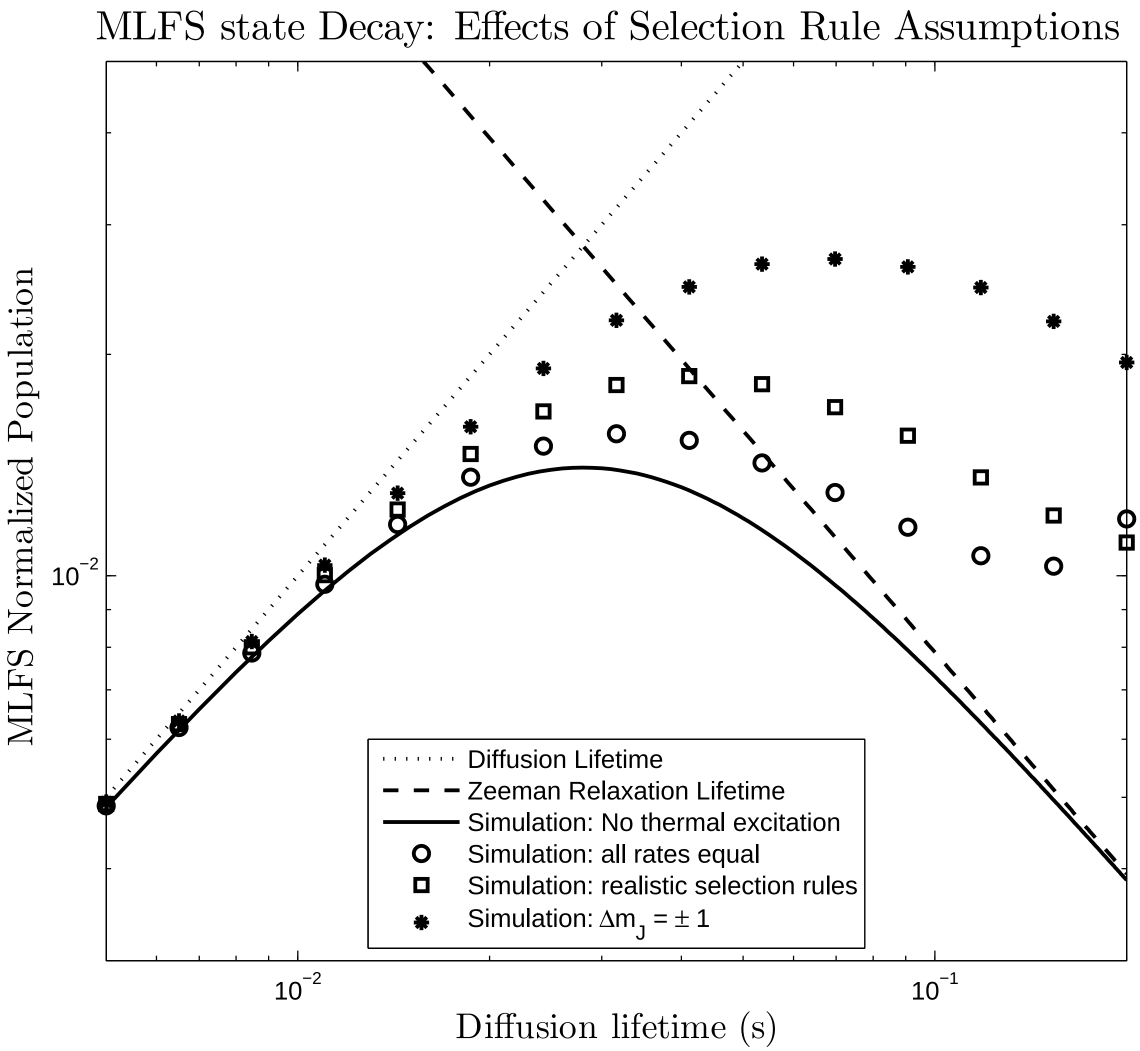

Figure 2-15: Simulated data using Zeeman cascade model. Without thermal excitation we reproduce the plot found in Figure 2-1. Thermal excitations cause an increase of $\tau_{MLFS}$ when the diffusion lifetime is $\geq$ the Zeeman relaxation lifetime. Simulations of this type are compared to data in Chapter 4 to determine a value of $\gamma$ for nickel.

A single data point ($\tau_{MLFS}$ at a single value of $\tau_d$) can be simulated with our Zeeman Cascade model by calculating the MLFS dynamics. The simulation inputs are $\tau_d$, temperature, selection rule assumption, and $\gamma$. $\Gamma_{zr}$ is calculated from the input parameters using (2-15). The simulation output is a MLFS decay curve which we fit to an exponential function to determine the simulated value of $\tau_{MLFS}$. A complete data set of $\tau_{MLFS}$ vs. $\tau_d$ can be created by generating data points for several values of $\tau_d$. Figure 2-15 shows a simulated data set for T = 1K atoms in a B = 0.8T field with an assumed $\gamma$ of $10^4$. When all Zeeman relaxation rates are assumed to be equal, the apparent MLFS lifetime actually starts to increase at large values of $\tau_d$. This occurs because we start measuring $\tau_d$ instead of $\tau_{zr}$ as discussed in the previous paragraph. By comparing our measurements of $\tau_{MLFS}$ vs. $\tau_d$ to Zeeman Cascade simulations we can determine the value of $\gamma$. In Chapter 4 this procedure is used to find $\gamma$ for nickel.

# Chapter 3

# Apparatus and Methods

We have constructed a buffer gas apparatus capable of thermalizing atomic clouds to sub-Kelvin temperatures. Although the apparatus is used primarily for atom trapping experiments, it has great flexibility and we are also able to study collisions at cold temperatures in constant magnetic fields. This chapter describes the apparatus, the spectroscopic methods used to study atomic collisions, and the laser systems developed to probe the atomic transitions.

## 3.1 Overview of the Experimental Methods

The major features of our approach are as follows. The experiments are performed in an experimental cell linked to a dilution refrigerator in a cryogenic apparatus. Buffer gas can be introduced into the cell from a reservoir, and if necessary removed rapidly by a specially designed high speed valve. The atoms to be studied are introduced into the chamber by laser ablation of metallic foil targets. The atoms are monitored by absorption spectroscopy from a laser beam that is introduced through a window in the bottom of the cell and retro-reflected to a detector. The cell is located in a pair of magnetic coils that can be operated in parallel (Helmholtz configuration) or in opposition (anti-Helmholtz) to make a trapping field. In the following sections we describe the major elements of the experiment: the cryogenic system, the experimental cell, lasers and optics, and explain our methods.

## 3.2 Cryogenic Apparatus

The apparatus has been specifically designed to advance buffer gas loading technology to the point of trapping a 1 $\mu_B$ species and thermally isolating it by removing the buffer gas. However, the flexibility of both the apparatus and the buffer gas method have made the studies presented in this thesis possible. A detailed description of all aspects of the experimental apparatus will not be presented here but can be found in the theses of other members of the group. The thesis of Nathan Brahms discusses our method of rapid buffer gas removal using a cryogenic valve and pumping sorb [19]. Nathan's thesis also describes the heat links used to thermally connect the experimental cell to the mixing chamber. Bonna Newman's thesis describes the design of a bucking coil which is installed in series with our superconducting magnet and prevents eddy current heating during magnet ramps by nulling the magnetic field at the copper mixing chamber plate [20].

After presenting a brief overview of the cryogenic apparatus we constructed for buffer gas cooling, I will describe in detail the design of the experimental cell used for these measurements and also for our group's recent demonstration of 1 $\mu_B$ trapping of atomic silver, copper, and lithium [19, 21].

We refer to the dilution refrigerator with its ancillary equipment, the cryostat, buffer gas loading system, and experimental cell collectively as the cryogenic apparatus. The cryogenic apparatus consists of several subsystems. They are listed briefly below with further details to follow:

1. The dilution refrigerator and associated vacuum spaces provide the cryogenic environment necessary to thermalize atoms to magnetically trappable temperatures.

2. The experimental cell and heat links to the refrigerator provide a region cold enough to implement buffer gas loading of atoms into a magnetic trap. Thermalized samples are studied spectroscopically in this region.

3. A cryogenic valve seals the top of experimental cell to maintain buffer gas pressure. The valve can be opened quickly by a room temperature actuation system to expose a pumping sorb. This allows rapid removal of the buffer gas after thermalization is complete.

4. A small vacuum chamber (the "waiting room") heat sunk to the 4K bath houses a charcoal sorb that is loaded with buffer gas. Heating the sorb to greater than $10K$ drives buffer gas through plumbing lines and into the experimental cell.

5. A superconducting magnet provides up to 4T trapping field. It can be run in Helmholtz or anti-Helmholtz configuration. A bucking coil nulls magnetic fields at the mixing chamber to prevent eddy current heating during magnet ramps.

6. Beam manipulation optics and detectors necessary for absorption spectroscopy are mounted to the bottom of the cryogenic dewar. Optical windows heat sunk to 300K, 77K, 4K, and $T_{cell}$ are integrated into cryogenic apparatus.

Figure 3-1 shows the apparatus with all subsystems installed.

### 3.2.1 Dilution refrigerator and vacuum systems

Our experimental cell is thermally anchored to the mixing chamber of an Oxford Instruments Kelvinox 400 dilution refrigerator. With our experimental systems installed the typical base temperature of the mixing chamber is $\sim$ 30 mK for a still power of 8 mW. The refrigerator and cell are located inside a vacuum space (inner vacuum chamber or IVC) surrounded by a liquid helium bath. The IVC vacuum is maintained using indium seals to join the sections of the vacuum can. All seals are made using .040 inch indium o-rings [44]. The IVC is separated into upper and lower cylindrical sections. The upper section is offset from the main axis of the cryostat. The offset is a leftover feature from a previous design and for our purposes is undesirable.

The upper IVC houses the refrigerator, buffer gas delivery system, heat links, and valve actuation mechanisms. The original IVC supplied with the refrigerator did not

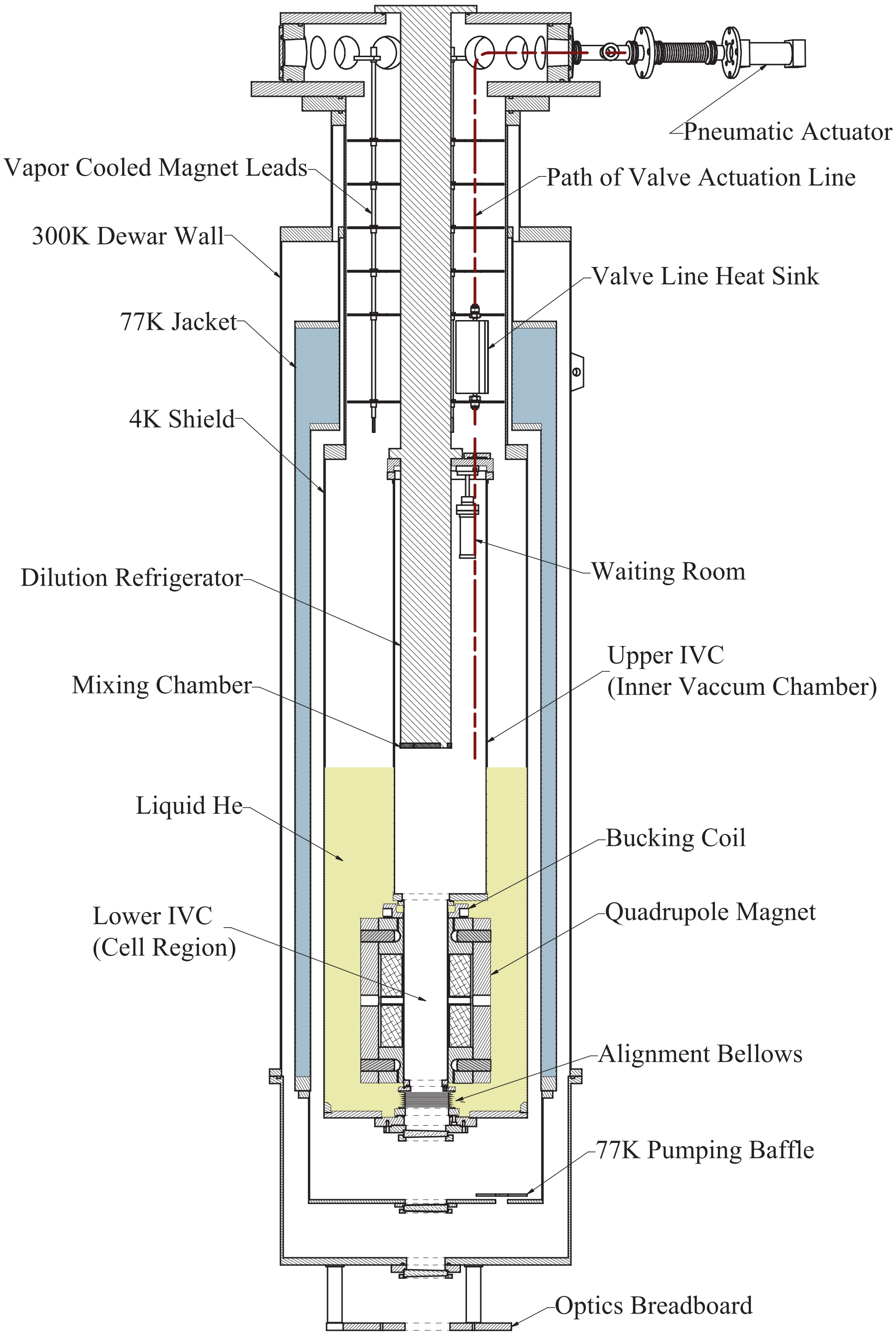

Figure 3-1: Schematic of cryogenic apparatus.

provide space for the these added complications, so a new aluminum IVC can was constructed.

The lower IVC houses the experimental cell. The 40 mm bore of the superconducting quadrupole magnet fits tightly around the IVC bottom. For trapping experiments the magnetic trap depth must be maximized so it is advantageous to keep the magnet as close as possible to the cell wall. For this reason the IVC bottom diameter is matched closely to the diameter of the magnet bore and the radial clearance between the cell and the IVC bottom wall is $< 2$mm. There is an inherent risk in making the cell-IVC clearance small. If a “touch” between the cell and the 4K IVC develops, the resulting heat load prevents the cell from reaching the designed base temperature. It is possible to maintain tight radial clearances while avoiding touches by constraining the cell's radial motion using standoff rings as described in [45, pp. 101-102]. Standoffs are attached to both the cell top and bottom and prevent the cell from touching the IVC as the system thermally contracts during cooldown or shifts position during valve actuation.

### 3.2.2 Optical access

We use laser light both to introduce atoms samples via ablation and to study atomic samples spectroscopically. Optical access to the apparatus is from beneath the cryostat, so the beam path must pass through the 4K region but not the 4K bath itself. The optical windows therefore must seal both the inner and outer vacuum chambers as shown in Figure 3-2. A welded metal bellows connects the IVC bottom to an adaptor plate. The adaptor plate seals the IVC vacuum space from the 4K bath space using two indium seals. The first seal connects the adaptor plate to the 4K cold plate. The second connects the plate to a 3 inch window. A series of four windows are thermally anchored at 300K, 77K, and 4K and $T_{cell}$. Windows heat sunk in this manner minimize heat loads due to blackbody radiation from room temperature.

Each window is cut with a 3° wedge to separate window reflections from the retroreflected probe laser during spectroscopy. All windows except the cell window are fused silica. The cell window is sapphire. Both window materials are transparent to the UV frequencies used to probe atomic transitions, but the thermal conductivity of sapphire is roughly a factor of 5 larger than fused silica [46, pp 58-59]. The increased thermal conductivity of the cell window prevents absorption of the laser beam from creating a hot spot in the center of the cell window.

The species of interest is introduced into the buffer gas via laser ablation using a single $\sim$ 10 mJ, 5 ns pulse from a frequency doubled Nd:YAG laser at 532 nm. The atomic precursors are metallic foils roughly 4 mm square. They are epoxied to a sample holder located near the top of the cell. Within a few ms after ablation thermalization with the buffer gas has occurred and the atomic sample is available for study. A retroreflecting UV-enhanced aluminum mirror is mounted into the center of the sample holder. The probe laser is steered onto the retroreflecting mirror from the optical breadboard mounted below the dewar. The return beam is steered onto a photomultiplier tube mounted onto the optical breadboard beneath the dewar. All optics needed to condition the YAG laser for ablation and the probe laser for absorption spectroscopy are mounted upside down on this breadboard. This includes mirrors, beam splitters, telescopes, photomultiplier tubes, etc. Additional details of the spectroscopy and ablation setup are found in section 3.3.

### 3.2.3 Superconducting magnet

The custom made magnet is similar to the Mark V magnet described in [47]. It consists of two coaxial superconducting coils wound with NbTi/Cu wire. The magnet operates at currents up to 100A, yielding 4T trap depths. When energized in an anti-Helmholtz configuration (trapping) the force between the coils can exceed 30 metric tons. A carefully designed titanium cask provides the mechanical strength to manage these forces. We typically use 97 amp currents because we have seen it quench occasionally at or around 100A. However, all but one or two of these quench events occurred while attempting to ramp the fields down rapidly during evaporative cooling experiments. If the fields remain static, 100A currents pose no problem. A bucking coil is mounted above the primary magnet. It is connected electrically in series with the main magnet and nulls the magnetic field at the copper mixing chamber. This

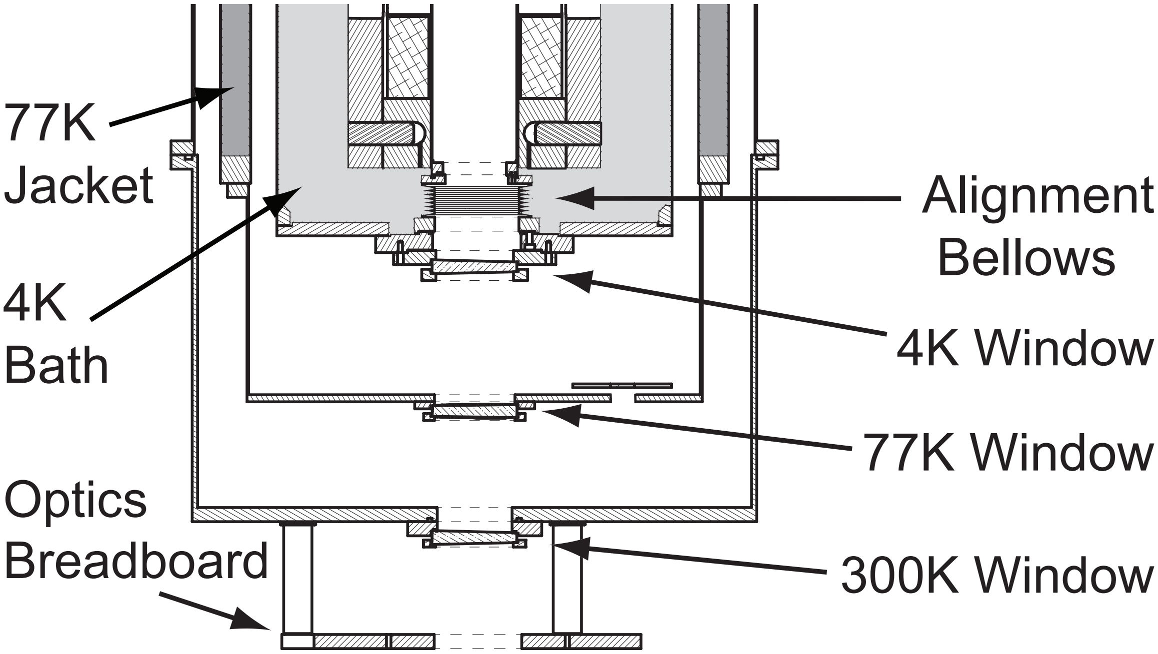

Figure 3-2: Heat sinking of optical access windows. The alignment bellows completes the IVC vacuum space by joining the lower IVC to the 4K cold plate.

minimizes eddy current heating of the mixing chamber during magnet ramps. [20].

The coils can also be run in Helmholtz geometry to generate nearly constant fields in the cell. Figure 3-3 shows the Helmholtz field profile in the cell for a current of 8 A. This Helmholtz field geometry has been used for all of the experiments detailed in Chapter 4.

### 3.2.4 Buffer gas delivery system

The ability to load a predictable amount of buffer gas into the cell is a essential for our experiments. A small copper vacuum chamber (the waiting room) serves as a buffer gas storage tank from which buffer gas can be loaded into the cell. The waiting room which is mounted to the inner surface of the IVC top contains 1.34 grams of charcoal sorb and can store $\sim$ 500 STP cc's of buffer gas. In practice we load only 200 STP cc's of $^3$He into the 50 cc waiting room. This guards against overpressuring the waiting room during an accidental rapid sorb warmup. The waiting room sorb is loaded with $^3$He from a room temperature gas handling system. The room temperature buffer gas

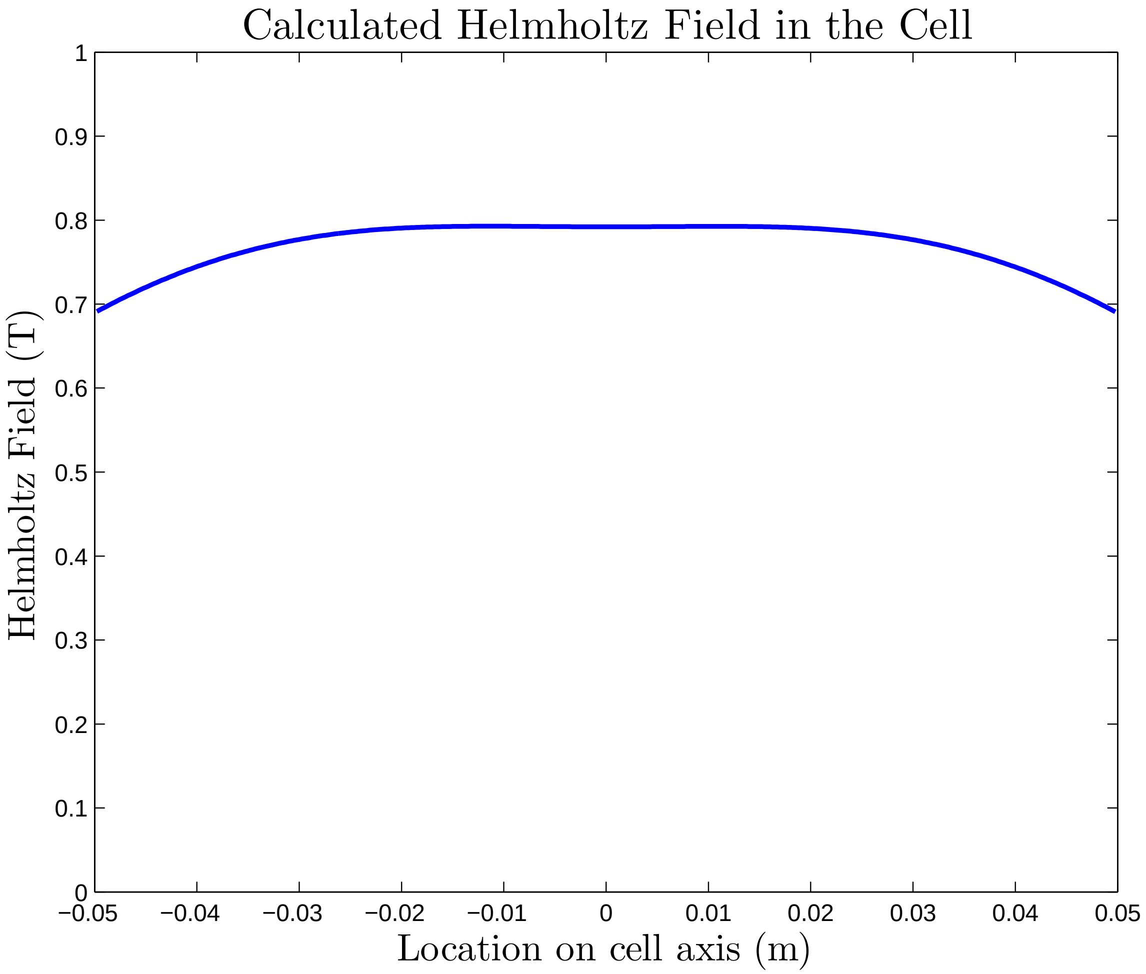

Figure 3-3: Plot of the magnetic field along the cell axis in the Helmholtz magnet configuration for a current of 8 A. The variation of field with position introduces magnetic broadening on the observed spectra.

is sent through a helium cold trap to freeze out impurities. It is then allowed to be cryopumped through a stainless steel vacuum line into the waiting room sorb. Sorb loading typically has to be done only once every few months.

Buffer gas is loaded into the cell by applying a voltage pulse across a 35W, 10Ω resistor attached to the waiting room. A brass washer inserted between the copper waiting room and the IVC creates a thermal resistance such that the heater pulse can raise the waiting room temperature to greater than 13K for voltages less than 2V. With each heater pulse, buffer gas is driven from the sorb and flows into the cell through a vacuum line. In our system a 90 second heater pulse raises the waiting room temperature to between 10-15 K provides a highly reproducible method of loading buffer gas into the cell.

Often several measurements must be taken at the same buffer gas density. It is important in this case that the buffer gas density does not drop between subsequent experimental runs. A constant density must remain in the cell without being pumped back into the waiting room sorb. To this end, an impedance 1/4 inch long and .015 inches in diameter is placed at the entrance of the cell. During loading the pressure across the impedance is great enough for the buffer gas to flow quickly into the cell. However, during experiments, the buffer gas pressure across the impedance is low and the time constant for buffer gas leaving the cell is approximately a half hour.

### 3.2.5 Valve and pumping sorb

As discussed in Section 2.1, background buffer gas causes trapped atoms to escape. In addition, background gas provides a thermal link between the trapped atoms and the walls of the experimental cell. This heat source frustrates efforts to evaporatively cool trapped atoms below the cell wall temperature. For these reasons the buffer gas must be removed after the trap is loaded and the atoms have thermalized. One method of buffer gas removal used in past experiments is simply to allow the cell to cool [29, 40, 45, 48]. This works for atoms with magnetic moments greater than or equal to 3 $\mu_B$ but to trap 1 $\mu_B$ atoms the buffer gas must be removed rapidly [17]. The thermal time constant of a typical buffer gas apparatus is longer than the required evacuation time, so simply allowing the cell to cool does not work.

Our apparatus design incorporates a fast cryogenic valve that can be opened to expose a pumpout sorb. In order to remove the buffer gas on the required time scale, the valve is designed with a large pumping aperture and a rapid openening time. Figure 3-4 displays a schematic of the cryogenic valve and experimental cell. The cell consists of two sections. The lower section is the trapping section. The upper section contains a valve chamber and a charcoal sorb pumping region for removing unwanted buffer gas. The sections are separated by a G10 shelf with a 1.3 inch diameter circular aperture. A polished alumina valve seat is epoxied to the top surface of the shelf. A flat teflon boot presses against the seat to seal off the trapping region from the pump region. $^3$He buffer gas hold times are greater than a half hour and are limited by the impedance to the waiting room and not the cryogenic valve. The valve is designed for $^3$He but we tried to use $^4$He as well with very little success. The hold times for $^4$He in the cell were too short to reliably measure. The cause for the short hold times was almost certainly superfluid flow either through the waiting room impedance or through the valve.

A custom designed spring maintains static compression of the boot against the seat under normal circumstances to provide a vacuum seal between the trapping and pumping regions. The valve boot is threaded into a Vespel shaft [49]. A 3/64 inch diameter wire pull rope is connected to the top of the valve shaft inside the cell. A pneumatic actuator at room temperature pulls the rope and lifts the valve boot greater than 1 inch off of the valve seat to expose the pumping sorb. The opening time is adjusted by throttling the exhaust of the pneumatic actuator. The minimum opening time is $\sim$ 40 ms. If the buffer gas is pumped out too rapidly, the resulting "wind" drives trapped atoms from the cell [17]. The valve speed is set empirically for each atom to the maximum pumpout speed attainable that avoids wind loss.

The pumping speed of the sorb is limited by the valve aperture to $\sim$ 10 l/s. During our previous attempts to evaporatively cool lithium, the pump sorb was thermally anchored to the cell wall at $\sim$ 100 mK. The background densities achieved in this case were not sufficiently good to evaporatively cool our trapped lithium samples [20]. There has been anecdotal evidence in other buffer gas experiments that a sorb is a more efficient pump when heated to $>$ 1K. [50] For this reason the sorb is now heat sunk to the stainless steel top of the valve chamber and can be heated with a resistive heater. A thorough study of the effectiveness of this change has yet to be performed.

### 3.2.6 Copper wire cell

The previous systems are described in more detail elsewhere [20, 21] so the discussion of each has been brief. In this section I present a detailed description of the experimental cell. An experimental cell suitable for 1 $\mu_B$ trapping and cooling has two primary design constraints. First, its temperature must be low enough to enable

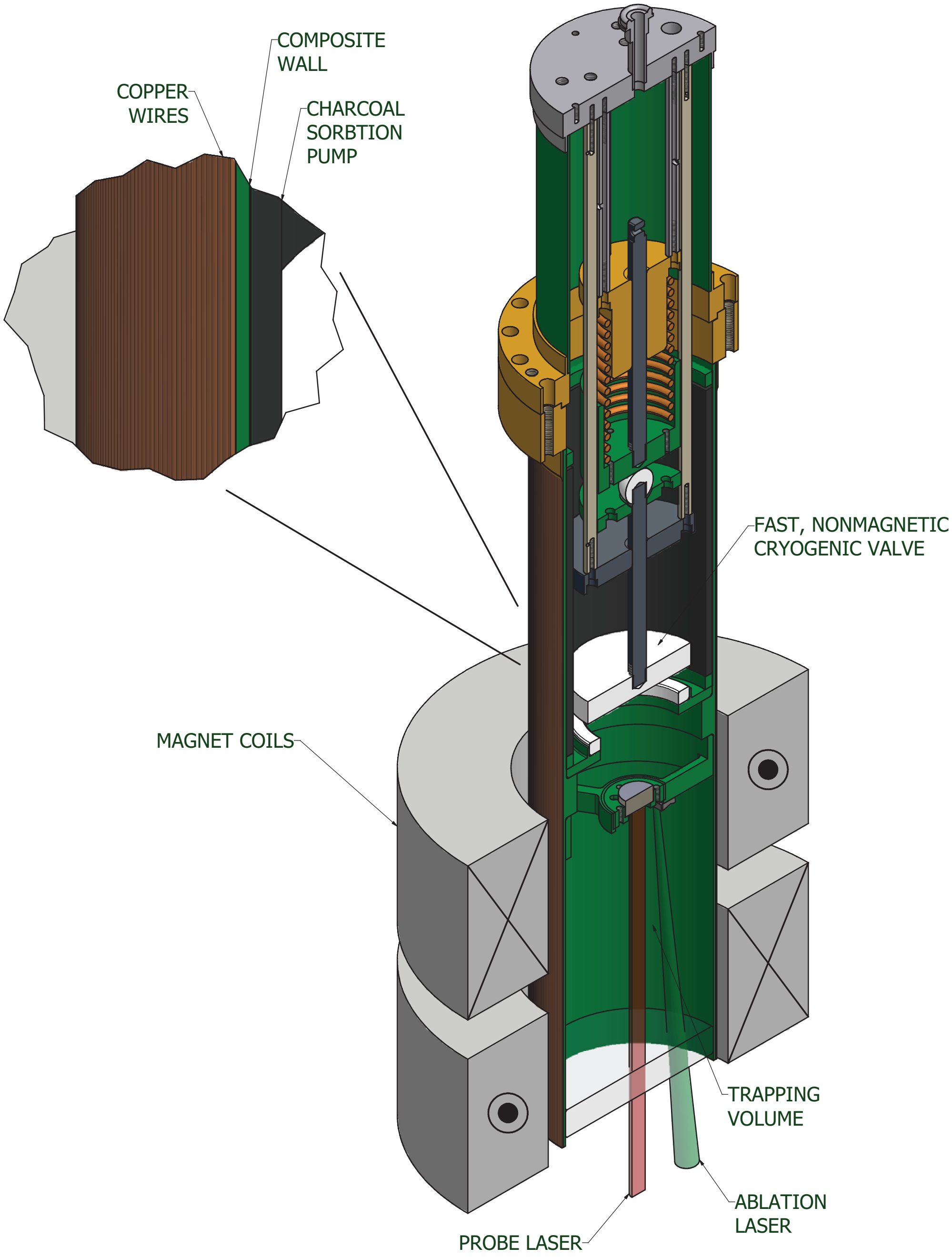

Figure 3-4: Wired cell with valve apparatus and magnet. The valve is normally closed. A wire rope connects the valve shaft to a room temperature pneumatic actuation system. The speed of valve opening can be changed by throttling the exhaust of the pneumatic actuator. Opening the valve exposes the charcoal pumping sorb to pump out the buffer gas. Thermal conduction along the cell wall is provided by $\sim$ 1000 0.25 mm wires running vertically along the outside of the cell. They are electrically insulated from each other to prevent eddy current heating during magnetic ramps.

loading of 1 $\mu_B$ atomic species into the magnetic trap. This was achieved for the first time in our apparatus using an oxygen-free high purity copper (OFHPC) cell [19]. OFHPC is used widely in cryogenics due to its extremely low thermal resistance [46]. Maintaining an extremely cold cell temperature also results in better final background buffer gas pressure which minimizes trapped atom loss. Lithium trapped lifetimes of $> 200$s had been observed in the previous run when the cell temperature was $\sim 100$ mK. Once the hurdle of trapping is overcome, the next step is evaporative cooling. Evaporative cooling requires lowering the magnetic trapping field to allow energetic atoms to escape from the trap [51, 52]. In an OFHPC cell it is impossible to ramp the magnetic fields quickly. Currents induced in the cell wall during magnetic ramps cause heating that raises the temperature of the cell. This drives helium off the walls and causes trapped atoms to be lost rapidly. As a result, evaporative cooling could not be attempted and a new cell design compatible with magnetic ramping had to be designed and built. Our studies of lithium lifetime versus cell temperature revealed that for cell temperatures $> 220$ mK, lithium loss became rapid. As a result, the second design constraint for the new cell was that eddy current heating during magnetic ramps must not raise the cell temperature above 200 mK. To be on the safe side we decided to keep the thermal gradient along the cell wall to less than 50 mK.

There were two dominant heat loads on the OFHPC cell. The first was a thermal link to the 4K IVC wall through the kevlar strings of the standoff rings (30 $\mu W$ each). The second was heat flow through the valve chamber walls from the stainless steel valve suspension plate heat sunk to the still. Neither the standoffs nor valve suspension system could be changed in the design of the new cell. Therefore the same heat loads had to be considered in the new cell design. The heat from the valve plate and upper standoff ring is deposited at the cell top near the heat link to the refrigerator. This heat is carried away by the refrigerator and does not establish a temperature gradient along the length of the cell. In constrast, the heat load from the lower standoff must be carried up the length of the cell and will cause a temperature gradient between the cell top and bottom. Any eddy current heat deposited during the ramp will cause an additional heating of the cell. The total temperature increase caused by these two heat loads must not raise the cell temperature above 200 mK.

### Cell design options: superfluid helium vs. copper wires

The two design constraints are somewhat at odds with one another. First, the cell wall must have excellent thermal conductivity along its length to keep the cell cold. This is why OFHPC was used in the first cell. The first constraint implies that copper might be useful in the design. Second, currents induced in cell material during magnet ramps are a heat load. Perhaps having copper in the design should be avoided altogether.

It is possible to design a cryogenic cell with good thermal transport along the walls using absolutely no copper. The hydrogen BEC apparatus relied upon the high thermal transport of superfluid liquid helium to thermally connect the cell top and bottom. A double walled G10 cell was constructed with a 2.2 mm space between the inner and outer walls [6]. During operation, the space between the two walls of the cell was filled with superfluid helium that provided adequate thermal transport along the cell [6]. Buffer gas experiments have used a similar design [36, 53]. However, this design comes with a heavy price in both design complexity and operational convenience. Consider the following nontrivial complications: constructing superfluid leak-tight vacuum spaces, thermally connecting the helium to the mixing chamber via sinter fins, designing/plumbing the jacket fill line, and filling/emptying the jacket each run. In addition, using a double walled cell decreases the inner diameter of the cell which decreases the trap depth compared to a single walled cell. For these reasons a jacketed cell design is undesirable.

An alternative design uses copper wires expoxied to the outside of a cylindrical cell body [54]. Eddy currents are minimized by using a low thermal conductivity cell body material and electrically insulated wires to prevent circumferential eddy currents around the cell. Eddy current heating within the individual wires must be controlled, however.

Given the two possibilities for cell design, a comparison of their thermal qualities is necessary to determine the best option.

### Cell design: thermal analysis

The rate of heat flow $\dot{Q}$ through a material of cross sectional area $A$ and length $L$ is

$$\dot{Q} = A\kappa\nabla T = \frac{A}{L}\kappa\Delta T \tag{3.1}$$

where $\kappa$ is the thermal conductivity[1]. Phonons are the fundamental excitations responsible for thermal transport in superfluid helium. Copper's conduction electrons are responsible for its thermal transport. The quantum statistics of bosonic phonons and fermionic electrons impact the effective thermal conductivity at low temperatures, resulting in $\kappa \propto T^3$ for helium and $\kappa \propto T$ for copper [46].

At room temperature the thermal resistivity of copper is dominated by electron-phonon scattering. At cryogenic temperatures the electron-phonon scattering is frozen out and electron-impurity scattering determines the resistivity. The residual resistivity ratio RRR is the ratio of 300K to 4K thermal resistivities and is a measure of the purity of the copper. The RRR of high purity copper can exceed 1000. A crude four wire resistance measurement was made on a long section of the magnet wire used in our cell [56]. The RRR of the wire was $\sim 100$. The thermal conductivity of 4K copper is $\kappa_{Cu} \simeq (RRR/76)T\ [W/cm \cdot K]$ [46, p. 66].

The MIT ultracold hydrogen jacketed cell achieved a thermal conductance $\dot{Q}/\Delta T = 5T^3\ [W/K]$ [6]. Given the cross sectional area of the superfluid jacket and the length of the cell, Equation 3.1 yields $\kappa_{He} \sim 120T^3\ [W/cm \cdot K]$. The effective thermal conductivity of a jacket of superfluid helium is proportional to its thickness $d$: $\kappa_{He} = \kappa_{He0}d$ [46]. This results in an expression for the MIT jacketed cell effective thermal conductivity: $\kappa_{He} \sim 500dT^3\ [W/cm^2 \cdot K]$.

---

[1] This equation does not apply to liquid helium below the $\lambda$ point. The thermal transport is due to internal convection of the normal and superfluid components of the liquid, not energy transport between neighboring atoms. However, an effective thermal conductivity will exist for a particular geometry [55].

The following effective thermal conductivity expressions can now be compared:

$$\kappa_{He} = 500\ dT^3\ [W/cm \cdot K] \tag{3.2}$$

$$\kappa_{Cu} = \frac{RRR}{76} T\ [W/cm \cdot K]. \tag{3.3}$$

Because of the different power law dependence on $T$, the effective thermal conductivity curves for copper and helium cross. At temperatures above this crossing point the effective thermal conductivity of the helium will be higher than the thermal conductivity of copper. At lower temperatures the fundamental excitations involved in the helium heat transport freeze out and the effective conductivity is lower than that of copper. The temperature at which the thermal conductivities are equal depends on both the $RRR$ of copper and the jacket thickness. For example, when RRR = 100 for copper and the jacket is 2.5 mm thick the thermal conductivities are equal at $\sim 100$ mK. This is approximately our operating temperature. Figure 3-5 plots the temperatures at which $\kappa_{Cu} = \kappa_{He}$ for a range of copper RRR's and helium jacket thicknesses. Assuming the total cross sectional area of the jacket and the copper wires is equal, the thermal conduction of both cells will be comparable. The trap depth should be maximized, which requires keeping the jacket or copper wire as thin as possible. This design constraint favors using copper since $\kappa_{Cu}$ is independent of the thickness of the copper wire whereas $\kappa_{He}$ falls as the jacket thickness decreases[2]. Both conduction and effective conductivity fall as the helium jacket thickness is decreased.

Mechanical considerations are also important. Connecting wires to the mixing chamber is much simpler for a wired cell compared to a jacketed cell. The wires can be welded to a copper plate and bolted to the mixing chamber. Thermally connecting a jacketed cell to the mixing chamber requires thermally connecting the helium to some manner of metal heat link. This is difficult due to the large Kapitza boundary

---

[2] The terminology in this section can be confusing. Thermal conductivity $\kappa$ appears in the relationship between heat flow and temperature gradient: $\dot{Q} = A\kappa\nabla T$. Thermal conduction $C$ is the ratio between heat flow and temperature difference: $\dot{Q} = C\nabla T$. Therefore $C = A\kappa/L$. Conduction of the copper falls as the wire diameter is reduced; conductivity does not.

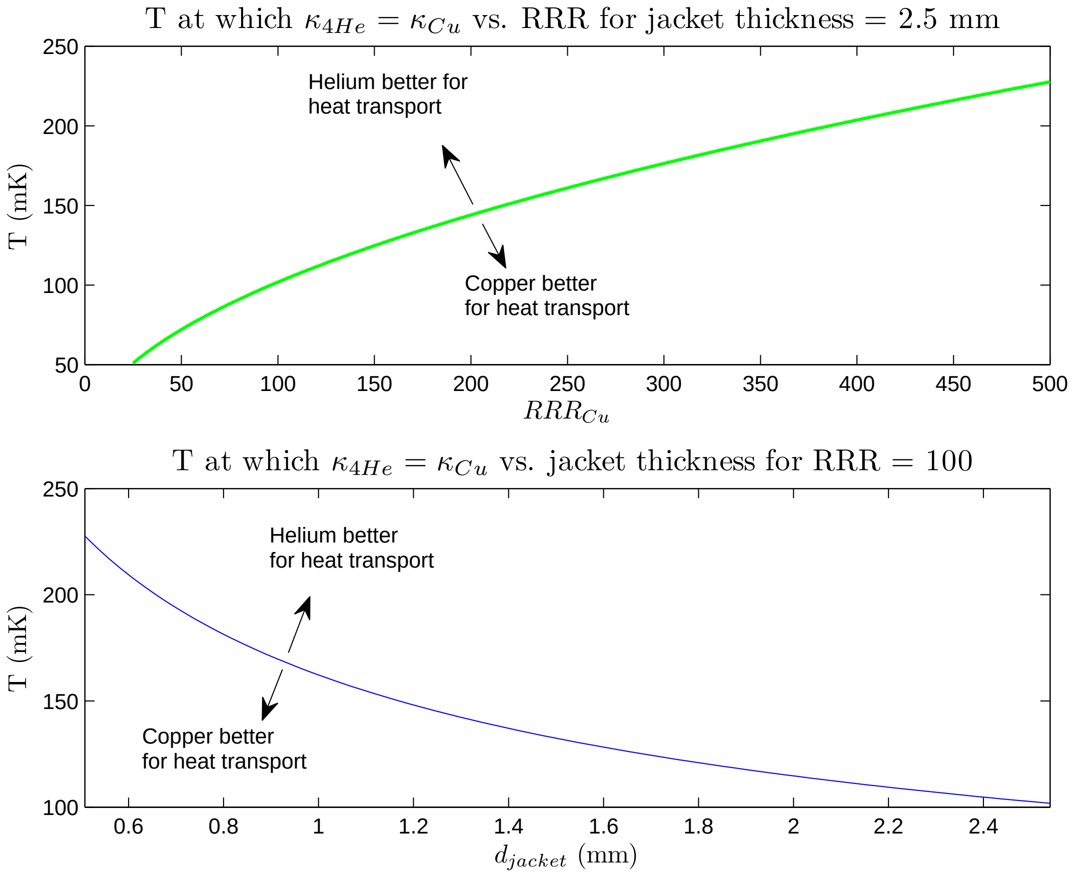

T at which $\kappa_{4He} = \kappa_{Cu}$ vs. RRR for jacket thickness = 2.5 mm

T at which $\kappa_{4He} = \kappa_{Cu}$ vs. jacket thickness for RRR = 100

Figure 3-5: Helium and Copper thermal conductivities as a function of temperature. The copper RRR is assumed to be 100 which is a lower estimate of the RRR of the copper used in our cell. The helium effective conductivity assumes a jacket thickness of 2.5 mm. Under these condition copper has a higher thermal conductivity below ∼ 100 mK than a helium jacket.

resistance between superfluid helium and a metal surface (a concise discussion of this issue is found on p. 51 of [6] with more information found in [46]). As a result, a very large effective surface area is required to make an adequate thermal connection. As a result, an array of sinter-covered metal fins extending from the metal heat link into the superfluid helium is needed [6, 53].

For the above reasons we adopted a wired cell design. Ideally we could use as much copper as was used in our previous 7.6 cm diameter .125 cm wall thickness cell. This would require 4700 0.25 mm or 1200 0.5 mm copper wires in multiple layers. A single layer of wires is more desirable from both a construction and trap depth

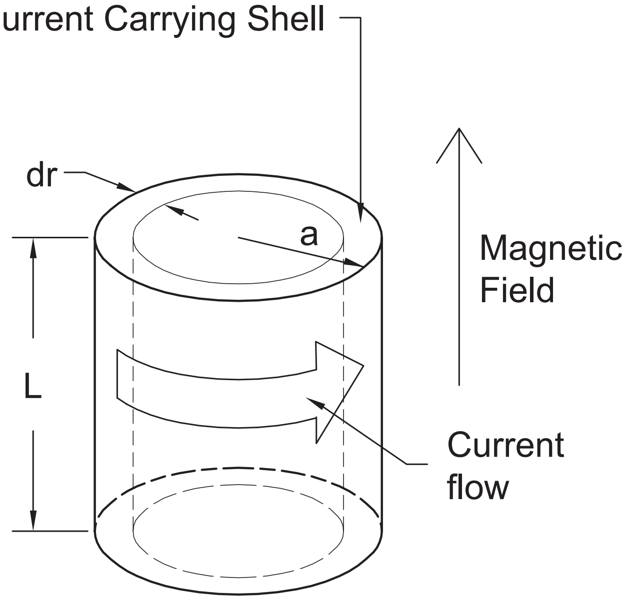

Figure 3-6: Eddy currents generated in a single wire. Changing magnetic flux captured in the wire induces currents which generate heat. Each current carrying shell of thickness $dr$ contributes to the heating.

maximization standpoint so long as there is enough copper to remove the 30 $\mu$W heat load from the bottom standoff without creating a $> 50$ mK gradient across the cell. If a single layer of 0.25 mm wires is used, full circumferential coverage of the 7 cm outer diameter of the cell requires 860 wires. For 860 0.25 mm wires, RRR = 100, L = 11 inches, and a 30 $\mu$W heat load, the calculated temperature drop across the cell is 15 mK and is within our design limit. Before implementing this design, we must confirm that the expected eddy current heating for this geometry is tolerable.

### Eddy Currents in Cell Wires

Consider an electrical conductor in the presence of a changing magnetic field. According to Lenz's law, currents will be induced in the conductor to oppose the change in magnetic field. The induced voltage $V = \dot{\Phi}_B = \dot{B}A$ where $B$ is the magnetic field and $A$ is the enclosed by a loop of current. This results in a deposited power $P = V^2/R$ where R is the resistance of the current loop. Because the induced voltage

$\propto A$, a continuous current path around the circumference of a copper cell leads to large eddy currents and unacceptable heating. However, the magnetic flux captured by a small wire is many orders of magnitude lower and the eddy current heating can be managed with a proper design. Figure 3-6 shows the geometry for a single copper wire of length L and radius a. The wire consists of an infinite number of current carrying shells of thickness $dr$ at radius $r$. Each shell captures magnetic flux in an area $A = \pi r^2$. If $\rho$ is the electrical resistivity of the wire, each current loop has a resistance $dR = \frac{\rho 2\pi r}{drL}$. The power generated in a single wire is

$$dP_{ec} = \frac{\dot{B}^2 (\pi r^2)^2 L}{\rho 2\pi r} dr \tag{3.4}$$

$$P_{ec} = \int_0^a dP = \frac{\pi a^4 L \dot{B}^2}{8\rho}. \tag{3.5}$$

The component of the magnetic trapping field parallel to the cell wires is not uniform along the length of the cell wall. The power deposited during the ramp is therefore found by averaging (3.5) over the length of the cell and multiplying by the number of wires. For 860 0.25 mm wires in an anti-Helmholtz trapping field and a current ramp rate of 5 amps per second (the fastest ramp rate used in experiments) the resulting eddy current power is 5 $\mu W$. Assuming the worst case scenario that this power is dumped into the cell bottom, this will increase the gradient across the cell by only 3 mK. Since $P_{ec} \propto r^4$, doubling the wire radius to 0.5 mm would result in a temperature gradient of $\sim$ 50 mK. Add this to the 30 $\mu$W heat load from the standoffs and the total temperature gradient is outside of our design parameters.

Based on the above design discussion, the cell was constructed using a single layer of 0.25 mm wires. Construction details are described in Appendix A. The wired cell includes both the trapping and pumpout sorb regions. Wires are affixed to the outer cell wall with Stycast 1266. Each wire has an extra 20 inches of length beyond the top of the cell. All wires are bundled together at the top of the cell in a pigtail. The electrical insulation is stripped off the end of the pigtail and the bare wires are crimped together in a copper tube and welded to a copper plate. The plate is polished and attaches with 4 × 8-32 screws to a “mixing chamber clamp” which is bolted to the mixing chamber. The top of the G10 cell body is epoxied into a cylindrical brass flange. The valve assembly has a mating brass flange. An indium seal between the brass flanges joins the valve to the wired cell. The brass flange has tapped holes which accommodate ruthenium oxide thermometers [57] and resistive heaters. An additional copper wire braid heat link (details in [19]) connects the brass flange to the mixing chamber clamp, providing additional heat conduction between the cell and the mixing chamber. The 2.656 inch 3° wedge sapphire window is epoxied into the cell bottom with Stycast 1266 (see Figure 3-4). The window is recessed a few millimeters to accommodate a ruthenium oxide thermometer which is epoxied to the inner cell wall just below the window. Figure 3-7 shows a picture of the wired cell connected to the valve apparatus and heat sunk to the mixing chamber.

### Cell Thermal Performance

The temperature of the cell is measured by Lakeshore calibrated ruthenium oxide thermometers [57] attached to the top and bottom of the cell. The measured steady state base temperatures during the first run with this cell was $\sim$ 115 mK at the cell top and $\sim$ 160 mK on the cell bottom. This is a 45 mK gradient compared to the designed 15 mK gradient but still satisfies the goals of $<$ 50 mK gradient and cell temperature $<$ 200 mK. There are a few possible reasons for the discrepancy. The heat load from the lower standoff might be larger than the 30 $\mu$W. The copper wire RRR could have decreased due to thermal stresses experienced during cooldown. Thermometer mounting is another viable explanation. The bottom thermometer is epoxied near the cell window on the inside of the cell body. The cell top thermometer is screwed down to the brass adapter ring which connects the valve apparatus to the cell. The thermal path between the thermometers contains the brass adaptor ring, a few mm G10, and some epoxy joints. This additional resistance can easily account for the discrepancy in thermometer readings. We saw a similar effect with our OFHPC cell where the measured temperature difference between the top and the bottom of the cell was 100 mK due to a poor thermal connection between the bottom of the cell and the thermometer.

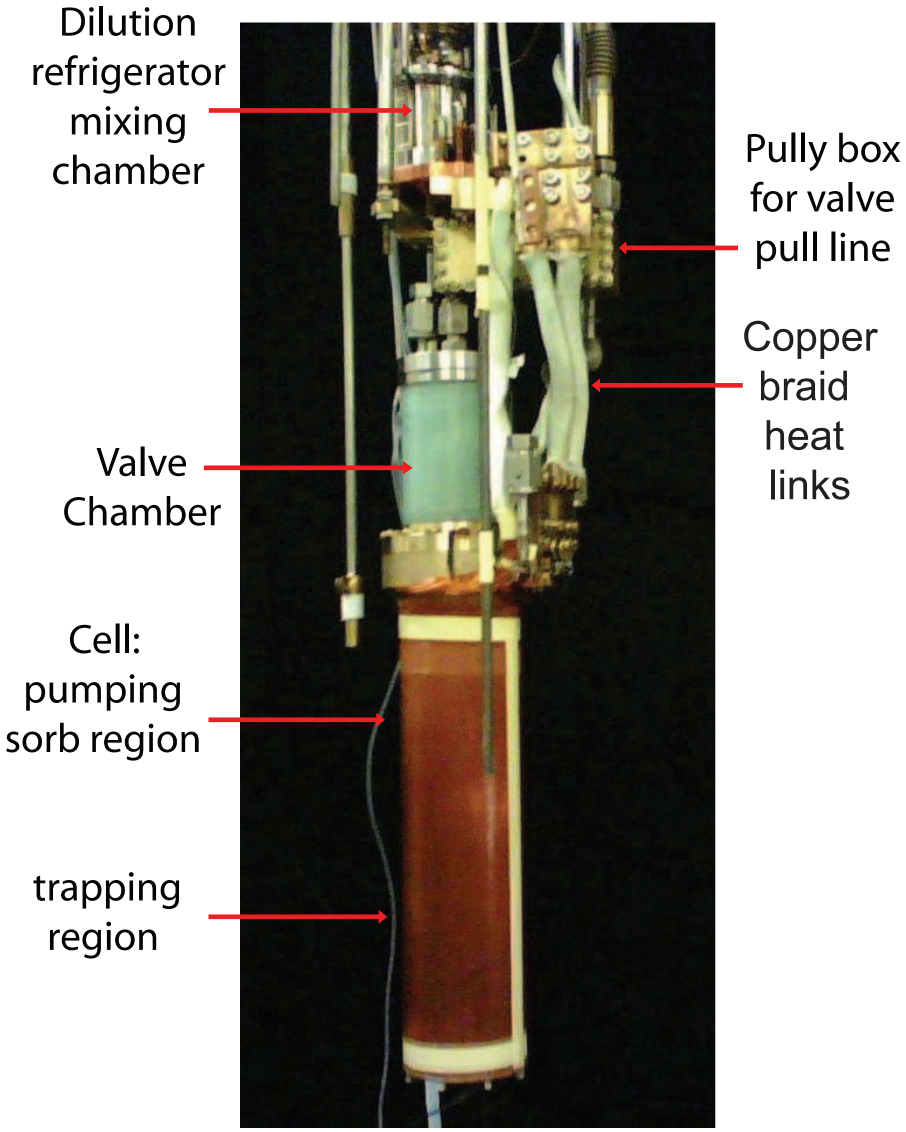

Figure 3-7: Photograph of mixing chamber, wired cell, and heat links.

The wired cell was used in two different "cooldowns" of the apparatus. Table 3.1 lists the temperatures at the top and bottom of the cell, the top and bottom of the copper braid heat link, and the mixing chamber for both experimental runs. Before the second cooldown, additional bolts were added to the connection between the mixing chamber clamp and the mixing chamber. The temperature difference between the top of the heat link and the mixing chamber is determined by the quality of the thermal connection between the cell clamp and the mixing chamber. The additional bolts on the connection during the second run decreased the temperature difference

| Location | Run 1 Temp (mK) | Run 2 Temp (mK) |
|---|---|---|
| Cell Bottom | 165 | 185 |
| Cell Top | 115 | 130 |
| Heat Link Bottom | 98 | 81 |
| Heat Link Top | 95 | 78 |
| Mixing Chamber | 27 | 27 |

Table 3.1: Temperature measurements at points between the cell bottom and the mixing chamber for two runs using the wired cell. Additional bolts were added to the mixing chamber clamp between the two runs, producing a better thermal link to the top of the heat link. The connection between the heat link and the top of the cell was worse in the second run. More care must be taken on that joint in the future.

from $\sim$ 70 mK to $\sim$ 50 mK. The temperature drop along the heat link was $<$ 5 mK during both runs. The temperature drop across the cell wires was $\sim$ 50 mK for both runs. The temperature difference between the bottom of the heat link and the top of the cell increased by $\sim$ 35 mK between the runs, so the overall cell temperature was $\sim$ 15 mK warmer during the second run. Future runs should pay particular attention to this joint. Ideally more bolts should be added. At the very least special care must be taken to tighten the bolts thoroughly.

Ideally a measurement of the thermal conduction of the cell wires vs. temperature would have been performed. This requires applying a series of known heat loads on the cell bottom and measuring the thermal gradient across the cell. Unfortunately the number of wires available for heaters and thermometry inside the IVC is limited. Installing a heater on the bottom of the cell was not the highest priority and this eliminated the possibility of measuring the cell conduction vs. temperature. However, the thermometry indicates that the thermal conduction along the cell wall is reasonably close to the design target. The cell described here was successfully used to load lithium into a magnetic trap with lifetimes comparable to those attained in the OFHPC cell [20].

We attempted evaporative cooling against a surface by reducing the coil current in either the top or the bottom coil. This moves the center of the trap either up towards the mirror or down towards the window while maintaining tighter confinement of the cloud than if the currents in both coils are ramped down together. Magnet ramps were implemented with ramp rates of up to 5 A/s. Even at the most rapid ramp rates of 5 A/s the cell temperature remained below our design limit of 200 mK. The top of the cell reached 190 mK during ramps to the window and 185 mK during ramps to the mirror.

## 3.3 Spectroscopic Methods

To study the properties of our atomic samples we need to measure the atomic density, lifetime, and temperature. The frequency dependent absorption of a probe laser beam as it passes through the sample can be used to find these properties. For our measurements we have a particular interest in measuring the properties of the most low-field seeking (MLFS) Zeeman state. As explained in Section 2.2, the ratio of elastic to inelastic cross sections $\gamma$ is determined by measuring the lifetime of the MLFS Zeeman state at several different buffer gas densities. To make this measurement the laser must be resonant with the MLFS Zeeman level and out of resonance with all other Zeeman states. In other words, we must fully resolve the spectrum of the MLFS state from other $m_J$ states. This is done by applying a uniform magnetic field that splits the Zeeman levels and allows us to isolate the MLFS peak from the peaks of neighboring $m_J$ states. We also measure the lifetime of the sample at zero magnetic field when the $m_J$ levels are degenerate. At zero-field the only atom loss mechanism is diffusion through the buffer gas to the cell wall. The diffusion lifetime $\tau_d$ of the atoms is proportional to the buffer gas density, so measuring $\tau_d$ provides a relative measurements of buffer gas density. We use our data set of $\tau_{MLFS}$ vs. $\tau_D$ to determine $\gamma$. The zero-field spectrum is also used to determine atom temperature because the thermal motion of the atoms affect its linewidth. In the following sections we describe the spectroscopic methods used to make these measurements. First we describe our experimental method of measuring the absorption of a laser beam in the atomic cloud. We then explain how the measured signal is used to find atomic density, temperature, and lifetime. This is followed by a description of the laser systems used for these measurements.

### 3.3.1 Spectroscopy setup

Atomic absorption is measured by sending the laser beam through the atomic cloud. A decrease in the intensity of the beam after it has passed through the cloud is the signature of absorption. A schematic of the spectroscopy setup used to perform these measurements is shown in Figure 3-8.

Optical access into the cryogenic apparatus is limited to a single port through the bottom. Beam steering optics mounted to the bottom of the dewar direct the laser into the cell. The beam retroreflects from a mirror at the top of the cell and the exiting light is detected on a photomultipler tube (PMT, Hamamatsu H6780-04 [58]). The frequency of the laser is tuned to the atomic resonance of interest. The laser frequency is scanned repeatedly over the atomic resonance as atoms are introduced into the cell via laser ablation. When the atoms absorb resonant laser light, the PMT signal decreases. In principle, a decrease in the detected power level on the PMT is the atomic absorption signal. However it impossible to differentiate between atomic absorption and probe beam amplitude noise due to laser power fluctuations, vibrations of the apparatus, shot noise, etc. These sources of noise can be $> 10$ % and would severely limit our experimental sensitivity.

Many of these sources of noise can be minimized in the following manner. We refer to the probe beam PMT signal as $S$. A fraction of the laser beam power is split off before being sent into the cryogenic apparatus. This pickoff beam is steered onto a second PMT. This photodetector signal is the reference $R$. Common mode noise due to laser amplitude fluctuations is removed by computing the transmission $S/R$. However, additional noise is inevitably added to the probe beam after the reference beam has been split off. Vibrations in the cryogenic apparatus introduce jitter on the probe beam which translates into amplitude noise in the case of position dependent losses or position dependent amplification on the PMT face. We have had some success mitigating the latter by using a beam diffuser in front of the PMT to make the beam profile more uniform, but nothing can be done to remove the position dependent losses. These sources of noise appear on $S$ but not on $R$, so they are not

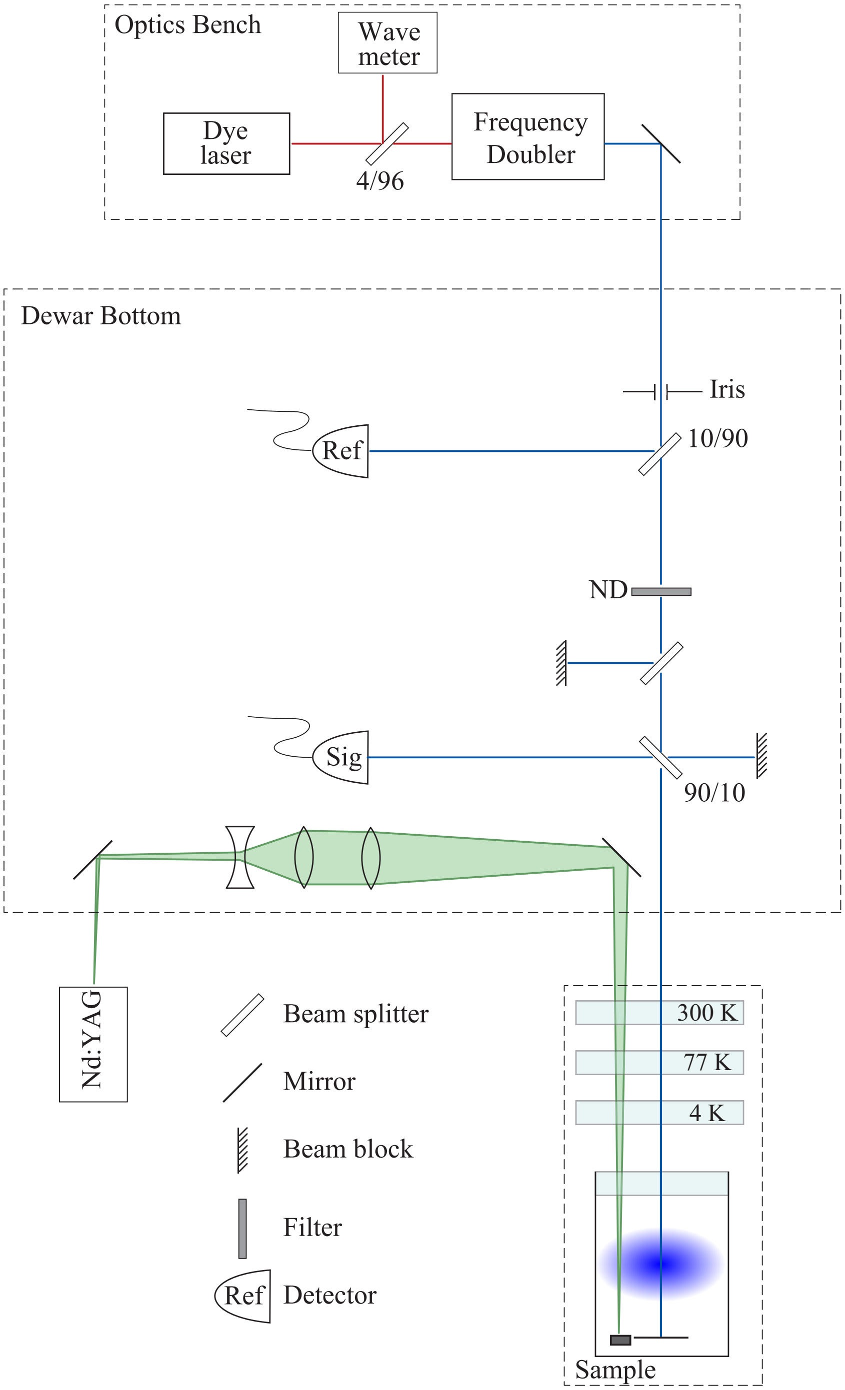

Figure 3-8: Optics setup for spectroscopy. The metallic sample is ablated by a Nd:YAG pulse to produce at atomic cloud. The probe beam is aligned to pass through the cloud. It is retro-reflected on the cell mirror and the return beam is aligned onto a photomultiplier tube (PMT). Before the probe beam is sent into the apparatus, a portion of its power is sent to a reference PMT. The absorption signal is obtained by dividing the signal detector voltage by the reference detector voltage.

removed by calculating $S/R$. For more details see the discussion in [48, pp. 19-23].

Although $S/R$ should equal 1 when no atoms are in the cell, there is some observed dependence on laser frequency. We extract temperature and density information from the frequency dependence of atomic absorption, so this baseline $B(\nu)$ must be removed. $B(\nu)$ is measured by scanning the laser and recording $S(\nu)/R(\nu)$ before introducing atoms into the cell. Several baseline scans are averaged together. $T$ is the ratio of the light intensity $I$ transmitted through the cloud to the light intensity $I_0$ sent into the cell: $T = I/I_0$. The transmission $T$ through the atomic cloud is calculated as $S(\nu)/(B(\nu)R(\nu))$. Performing this operation guarantees that when no atoms are in the cell $T$ equals 1 for every value of $\nu$. Any absorption due to atoms results in a decrease of $T$. The absorption signal $A = 1 - T$ is nonzero only when atoms in the cell absorb the laser light.

### 3.3.2 Photon absorption and optical depth

We relate the absorption signal $A$ to atom temperature and density by reviewing the theory of photon absorption near a two-level atomic resonance. The topic has been presented thoroughly elsewhere for two level systems [59] and multilevel atoms [60], so no detailed description of either case is presented. It is instructive, however, to highlight a few principles specific to understanding absorption in our experiments where the spectroscopy is performed in a magnetic field.

In the lab we measure the attenuation of the laser beam as it passes through the atomic cloud. We therefore seek an expression for the expected change in the intensity $I$ of the beam after it travels a distance $z$ through the cloud of density $n_{atoms}$. The desired relationship is derived as follows:

$$\dot{I} = -c\sigma_\gamma n_{atoms} I \tag{3.6}$$

$$\frac{dI}{dz} = -n_{atoms}\sigma_\gamma I. \tag{3.7}$$

$$\frac{I}{I_0} = exp(-n_{atoms}\sigma_\gamma z) \tag{3.8}$$

$$\ln\left(\frac{I}{I_0}\right) = -n_{atoms}\sigma_\gamma z = -OD \tag{3.9}$$

where $c$ is the speed of light, $I_0$ is the input intensity, $OD$ is the optical depth for the transition, and $\sigma_\gamma$ is the cross section for photon absorption. Inserting the absorption $A$ into (3.9) we see that $OD = -\ln(1-A)$.

We now have a relationship between the measured absorption and the atomic density which seems simple, but there is hidden subtlety. First, the density of atoms in the cloud can vary with position $n(\vec{r})$ which leads to a position dependent absorption. Second, the resonant frequency $\omega_0$ is Zeeman shifted in a magnetic field $B$:

$$\Delta\omega_0 = \frac{\Delta\mu B}{\hbar} \tag{3.10}$$

where $\Delta\mu$ is the difference between the ground and excited state magnetic moments. Third, the absorption cross section $\sigma_\gamma$ depends on several concepts which we shall considered in more detail.

For a two-level system, the cross section as a function of angular frequency $\omega$ is

$$\sigma_\gamma(\omega) = \frac{3}{2\pi}{\lambda_0}^2 \frac{(\Gamma/2)^2}{(\omega-\omega_0)^2 + (\Gamma/2)^2} \tag{3.11}$$

where $\omega_0$ and $\lambda_0$ are the resonant angular frequency and wavelength, $\Gamma$ is the natural linewidth. Equation (3.11) assumes that the polarization of the photon is optimized for driving the particular transition. This is true for the two level atom because the polarization of the laser is parallel to the induced dipole moment in the atom. For multilevel atoms the polarization of the laser will affect the probability to drive a transition and (3.11) must be multiplied by additional factors.

Each photon carries one unit of angular momentum which it imparts to the atom when absorbed. An arbitrary polarization can be represented as a linear combination of orthogonal angular momentum states $|1, q\rangle$ where $q$ is the projection of the photon angular momentum onto the beam propagation axis. The value of $q$ is 0 for linearly polarized light, 1 for left-hand circularly polarized light, or -1 for right-hand circularly polarized light.

Consider a transition from a ground state $\left|J_g, m_{J_g}\right\rangle$ to an excited state $|J_e, m_{J_e}\rangle$. The probability to drive the transition $P_{g\to e}$ depends upon polarization in two ways. First, $P_{g\to e}$ is related to the Clebsch-Gordon coefficient: $P_{g\to e} \propto \left\langle J_g, m_{J_g}; 1, q | J_e, m_{J_e}\right\rangle^2$. This relationship arises from the quantum properties of angular momentum addition of the ground state atom and the photon and indicates that the transition probability is zero unless $q + m_{J_g} = m_{J_e}$. Following the notation in [53] we call this factor $C_m$. A second effect arises because the quantization axis for photon angular momentum is along the beam propagation direction whereas the quantization of the atomic angular momentum is along the magnetic field. Therefore the beam axis must be projected onto the magnetic field axis in order to calculate how much of the incoming laser polarization can drive a particular atomic transition. This factor depends upon the location of the beam in the cell for nonuniform magnetic fields. We label this factor $C_p(z, \rho, \varphi)$ where $z$ is the location along the cell axis, $\rho$ is the distance from the cell axis, and $\varphi$ is the azimuthal angle.

Putting all these considerations together, we find the following expression taken from [53, p. 154] for the optical depth for a beam of cross sectional area which is small compared with variations in atomic density. It is necessary to integrate along the beam path due to the position dependence of the factors described above.

$$OD\left(\omega, \rho, \varphi\right) = \frac{3{\lambda_0}^2}{2\pi} \cdot C_m \cdot \int dz \frac{C_p\left(B\left(z, \rho, \varphi\right)\right) n\left(r, \rho\right) \left(\Gamma/2\right)^2}{\left(\Gamma/2\right)^2 + \left(\omega - \omega_0 - \frac{\Delta\mu \cdot B(z,\rho,\varphi)}{\hbar}\right)^2} \tag{3.12}$$

The optical depth for the entire beam is obtained by integrating over the beam profile. We now have a relationship for OD that depends upon the following parameters: atomic density, beam position, laser frequency, light polarization, and magnetic field.

The scheme for translating the above concepts into a spectrum simulation using these parameters as inputs has been described by Weinstein [53] with a few additional considerations specific to measurements in anti-Helmholtz fields discussed by Brahms[19]. Experimental absorption data is fit to the simulated spectrum by performing a least squares fitting routine to obtain atomic density. Fitting for temperature is discussed in the next section.

### 3.3.3 Zero-field spectroscopy: temperature fitting

Modeling the Zeeman relaxation behavior of the MLFS requires accurate knowledge of temperature. In the simple model presented in Section 2.2, our expression for $\gamma$ in 2.29 depends linearly on T: $\gamma \propto \overline{v}^2 \propto T$. Furthermore, thermal effects on the Zeeman Cascade model detailed in Section 2.3 significantly impact the interpretation of observed MLFS lifetimes. For these reasons, accurate knowledge of atomic temperature is needed.

Each atomic transition has a natural linewidth $\Gamma$ even at zero temperature, resulting in a Lorentzian absorption profile centered at $\omega_0$ as in Equation 3.11. Atomic motion at nonzero temperature causes the resonant frequency to shift: $\omega^{'} = \omega_0 - \vec{k} \cdot \vec{v}$ for a photon with momentum $\hbar\vec{k}$ and an atom with velocity $\vec{v}$. This results in a mapping of the Boltzmann velocity distribution onto the intensity profile for absorption. The Doppler profile describes the distribution of resonant frequencies. At each resonant frequency there is a Lorentzian absorption profile. The total absorption at a single angular frequency $\omega$ is the summation all the individual Lorentzian contributions centered at all possible resonant frequencies $\omega^{'}$. Mathematically this operation is performed by convolving the Doppler and Lorentzian distributions. The result is the Voigt profile [61, p. 70]:

$$I(\omega) = C \int_0^\infty \frac{exp\{-(((c/v_p)(\omega_0 - \omega)/\omega_0))^2\}}{(\omega - \omega')^2 + (\Gamma/2)^2} d\omega^{'} \tag{3.13}$$

$$C = \frac{\Gamma n c}{2 v_p \pi^{3/2} \omega_0} \tag{3.14}$$

where $n$ is the atomic density, $c$ is the speed of light, and $v_p$ is the most probable velocity $\sqrt{2k_BT/m}$. The above model has $v_p$ as a temperature dependent parameter. The temperature of the atomic cloud is extracted by fitting the experimentally obtained absorption spectra to (3.13). These spectra are taken at zero magnetic field to avoid magnetic broadening.

The accuracy of our temperature measurement is affected in two ways. First, magnetic broadening of the spectrum will be misinterpreted as Doppler broadening. We measure the atomic spectrum when no current is flowing in the magnet. However, once the magnet has been ramped up and down it stores trapped fluxes. A magnetic field is therefore present even when the current through the coils is zero. Typical fields due to trapped fluxes along the bore of a magnet similar to ours have been measured and are on the order of 10 gauss [47]. We now compare the frequency shifts induced by a 10 gauss field with the Doppler width. This represents a worst case estimate of the effect on our temperature measurement. A more careful treatment would be in order if we could carefully measure the residual fields in our cell. Since we do not have that information, the following will suffice to illustrate the effect.

For Nickel atoms ($g_J = 1.25$) a 10 gauss field causes a frequency shift of for a $\Delta m_J = \pm 1$ transition of $\Delta\nu_B = \pm g_J \mu_B B/h \sim \pm 18$ MHz. The magnetic splitting between $m_J = \pm\ 1$ lines $= 2\Delta\nu_B \sim 36$ MHz. The splitting between intermediate Zeeman levels will be less than this. However, as a worst case estimate we assumed that this splitting leads to a magnetic broadening of $\sim 36$ MHz. The Doppler width [61, p. 68]

$$\Delta\nu_D = \nu_0\sqrt{8k_BT\ln 2/(mc^2)} \tag{3.15}$$

is 67 MHz at a cell temperature $T_{cell} \sim 300$ mK. $T_{cell} \geq 300$ mK for all of our experiments. The atoms can not be colder than the temperature of the cell wall, so this represents the minimum possible Doppler width in our system. The ratio of these widths is $\Delta\nu_B/\Delta\nu_D \sim 0.5$. We now assume the total width $\Delta\nu_{tot} = \sqrt{(\Delta\nu_D)^2 + (\Delta\nu_B)^2}$. The change in predicted temperature associated with the magnetic broadening is found

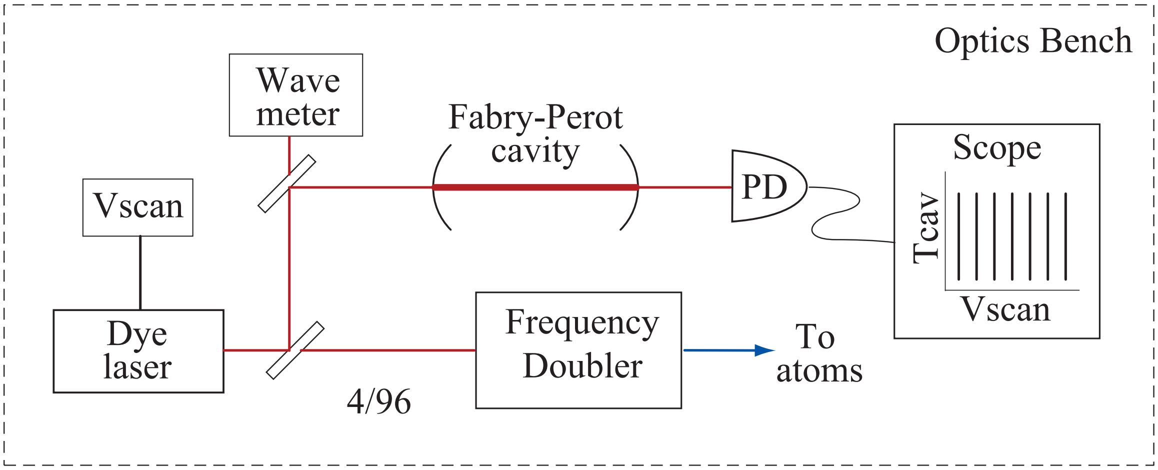

Figure 3-9: Schematic of the voltage to frequency conversion setup. A portion of the fundamental frequency is sent through a confocal Fabry-Perot cavity. The transmission peaks are recorded during spectroscopy. The peak spacing of 150 MHz is used to assign a frequency excursion to a change in scan voltage.

by solving (3.15) for $T$ and replacing $\Delta\nu_D$ with $\Delta\nu_{tot}$. This procedure predicts $T \sim$ 400 mK, so the magnetic broadening causes an overestimate of the temperature of 30%. The effect at $T = 1$K is below 10%. The temperature that we measure may be systematically higher than the actual temperature, but the effect will not be greater than $\sim$ 25%.

The second effect on measured temperature concerns the voltage to frequency conversion of our laser scans. The laser is scanned with a sine wave from a signal generator (see Section 3.4.2 for details). This scan voltage is recorded for each experimental run and the spectrum is generated by plotting optical depth versus scan voltage. If we wish to fit the spectrum for temperature to a Voigt profile we must convert the voltage scan to a frequency excursion. Although the laser control box has a nominal voltage to frequency conversion, it is of limited accuracy and we need a better method.

A confocal Fabry-Perot cavity (FPC) provides a means of calibrating our frequency scans. A FPC consists of two identical reflective mirrors separated by a distance $L$ equal to their radii of curvature. In this geometry the resonator exhibits an array of equally spaced transition peaks separated by the free spectral range $\Delta_{fsr} = \frac{c}{4L}$ where $c$ is the speed of light [62]. We use a cavity with $L = .5$ meters ($\Delta_{fsr} = 150$

MHz) as an optical ruler to calibrate our voltage to frequency conversion. Figure 3-9 shows the setup. A small fraction of the dye laser fundamental frequency output is split off before the resonant doubler and sent through the FPC. Cavity transmission is detected on a photodetector and recorded during data acquisition. Each data file thus contains arrays of laser scan voltages $V$, the transmission $T$ through the FPC, and the atomic optical depth $OD$. The FPC transmission vs. scan voltage is shown for a single sweep of the laser in Figure 3-10. In software, the location of each cavity peak is located and indexed. The laser voltage corresponding to each peak is identified and assigned an absolute frequency in multiples $\Delta_{fsr}$. We now are in possession of a "lookup table" of frequency versus voltage which is used to interpolate frequency values $\nu$ for *every* recorded voltage point. Plotting $OD$ versus $\nu$ yields a frequency calibrated absorption spectrum that we can use to accurately fit for atomic temperature.

### 3.3.4 Zero-field spectroscopy: measure diffusion lifetime

A measurement of the lifetime of atoms in our cell at zero-field provides a relative measurement of buffer gas density. The lifetime of the atoms at zero-field is determined by their diffusion through the buffer gas to the cell wall. The diffusion lifetime $\tau_d$ is proportional to the buffer gas density in the cell (see Equation 2.4). A measurement of $\tau_d$ is therefore a relative measurement of $n_{BG}$.

To make the lifetime measurement we use the following procedure. The frequency of the laser is tuned to the atomic resonance of interest. The laser frequency is scanned repeatedly over the atomic resonance as atoms are introduced into the cell via laser ablation. Each scan over the resonance yields an absorption spectrum similar to the nickel spectrum shown in Figure 3-11. A spectrum is measured for each sweep of the laser, resulting in a series of spectra separated in time by half the laser scan period.

An optical depth (OD) data point is generated for each spectrum by integrating the signal over the entire spectrum and subtracting off a "baseline" portion of the laser scan where the OD is zero. This procedure removes noise as frequencies lower

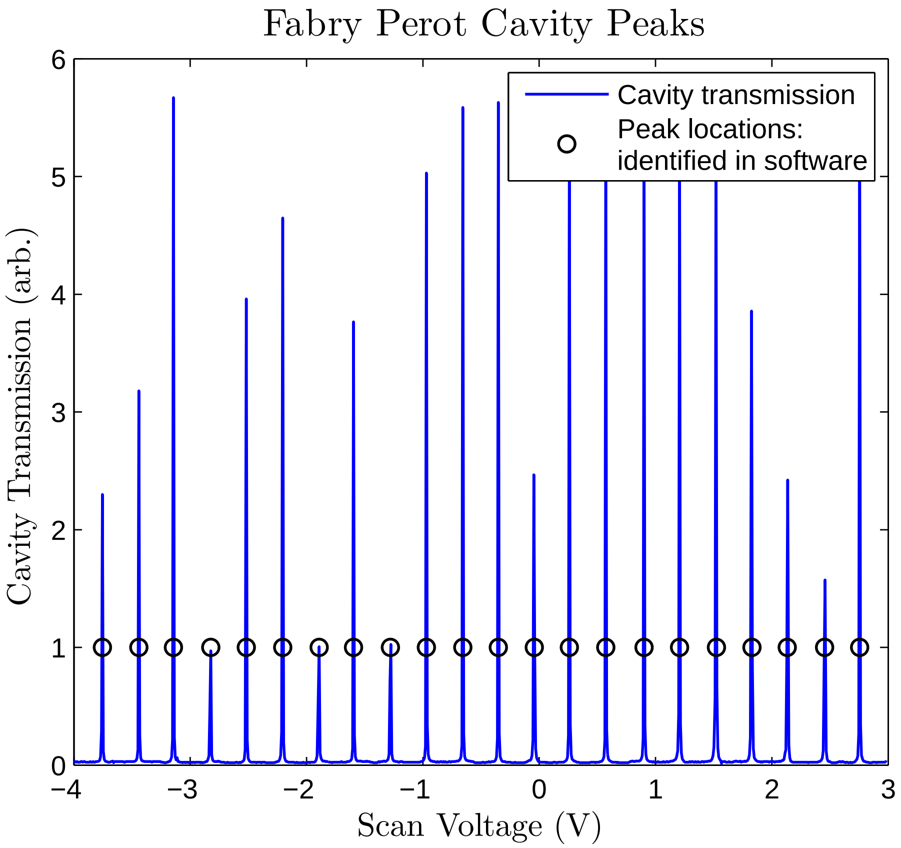

Figure 3-10: Fabry-Perot peaks used for frequency calibration. Cavity transmission is plotted versus scan frequency. In software the locations of the peaks are identified. The peaks measurements are not the same height because they are scanned over quickly. Since the peak spacing is known to be 150 MHz, we can assign a known frequency excursion to the voltage interval between each cavity peak. Interpolation between these points calibrates the entire voltage scan.

than the laser scan rate. In Figure 3-11 the portion of the scan that is integrated is shown in red and the baseline portion is shown in black. The OD decreases as a function of time due to atom loss from the cell. We fit the decay in OD to a single exponential decay function to determine the lifetime $\tau$. We repeat the procedure to measure $\tau$ several times and average the values together determine $\tau_d$. The time resolution of the measurement is the inverse of the laser scan rate. Scanning slowly results in poor time resolution. Therefore measuring short diffusion lifetimes requires scanning the laser quickly. The laser has a limited scan rate so some diffusion lifetimes are too short to measure while scanning the laser. It is also possible to measure $\tau_d$

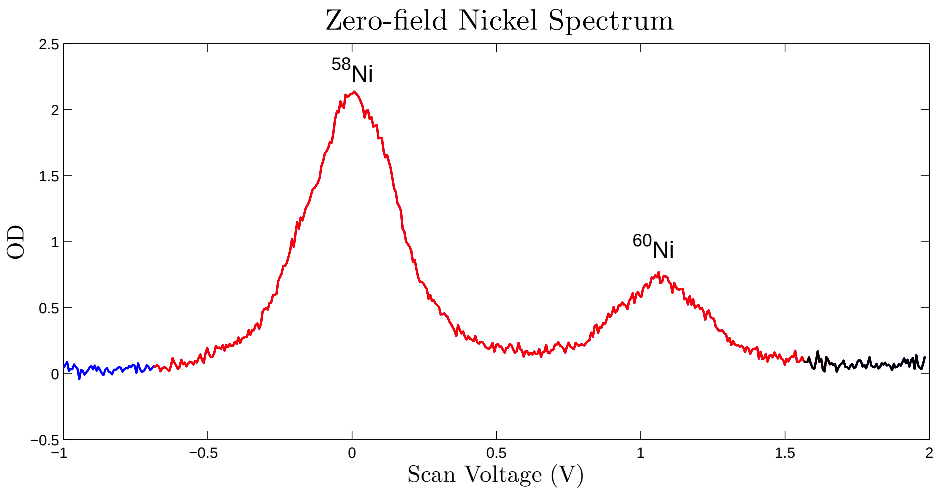

Figure 3-11: Zero-field nickel spectrum. We characterize the optical depth of the sample by integrating over the spectrum (red portion) and subtracting off the average of a nonresonant section of the scan (black portion). This "baseline subtraction" method removes noise at frequencies lower than our scan rate. By scanning over the resonance repeatedly we track the decay of the optical depth as a function of time to find $\tau_d$.

by parking the laser at the peak of the atomic transition and observing the decay of the OD. However, with this method we cannot remove low frequency noise because no baseline subtraction is possible.

### 3.3.5 Spectroscopy in constant field: resolving the $m_J = J$ transition to measure $\tau_{MLFS}$

To measure $\tau_{MLFS}$ we must fully resolve an MLFS absorption peak. This is accomplished by turning on a Helmholtz magnetic field which Zeeman shifts the electronic energy levels. As a result, the zero-field spectrum splits into multiple lines which are shifted relative to the zero-field resonance.

Consider a transition from an $m_J$ ground state with g-factor $g_J$ to an $m_J + \Delta m_J$ excited state with g-factor $g_J{}'$ The Zeeman induced frequency shift $\Delta\nu_Z$ due to a magnetic field $B$ is found by subtracting the excited and ground state Zeeman shifts in 2.10.

$$\begin{aligned}\Delta\nu_Z &= ((g_J{'}(m_J + \Delta m_J) - g_J m_J))\mu_B B \\ &= (g_J{'}\Delta m_J + (g_J^{'} - g_J)mJ)\mu_B B \\ &= (g_J{'}\Delta m_J + (\Delta g)m_J)\mu_B B. \end{aligned} \tag{3.16}$$

Selection rules require $\Delta m_J = 0, \pm 1$. There are two contributions to the shift. The first term, $g_J{'}\Delta m_J \mu_B B$, arises from the difference in slope between an $m_J$ ground state and an $m_J \pm 1$ excited state. It is nonzero only when $m_J$ changes, i.e. $\Delta m_J = 0$ transitions are not shifted. The second term, $\Delta g m_J \mu_B B$ appears due to a difference in the g-factors of the ground and excited states. This causes the slopes to be unequal even when $m_J$ is equal for the ground and excited state[3]. For the cobalt, iron, and nickel transitions studied, $\Delta g / g_J{'} << 1$. Therefore, for $\Delta m_J = \pm 1$ transitions most of $\Delta\nu_Z$ is due to the first term. This large frequency shift is independent of the value of $m_J$. In contrast, there is an $m_J$ dependence in the second term. This differential shift results in an equally spaced array of transitions corresponding to the various $m_J$ states.

Figure 3-12 shows a simulation of the overall effect of a 1 Tesla Helmholtz field on the $a^3F_4 \rightarrow y^3G_5$ transition in nickel. The simulation was generated using the method described in Section 3.3.2. Nickel is a $J = 4$ atom so there are 9 $m_J$ states. The linewidth for each transition is assumed to be the natural linewidth. The figure is only meant to illustrate the method of resolving the MLFS line, so the linewidths do not reflect those observed in the experiment. The observed linewidths are $\sim$ 200-300 MHz due to additional Doppler and magnetic broadening.

The upper plot shows the $\Delta m_J = \pm 1, 0$ transitions. They are separated by $\sim$ 17 GHz at 0.8T. The lower plot is a zoomed-in view of the $\Delta m_J = 1$ transitions. The 9 transitions correspond to the 9 values of $m_J$. Each spectrum is fully resolved.

We tune our laser to the strongest available MLFS state transition peak. The

---

[3] With the obvious exception of the $m_J = 0 \rightarrow m_J = 0$ transition where both states have zero slope.

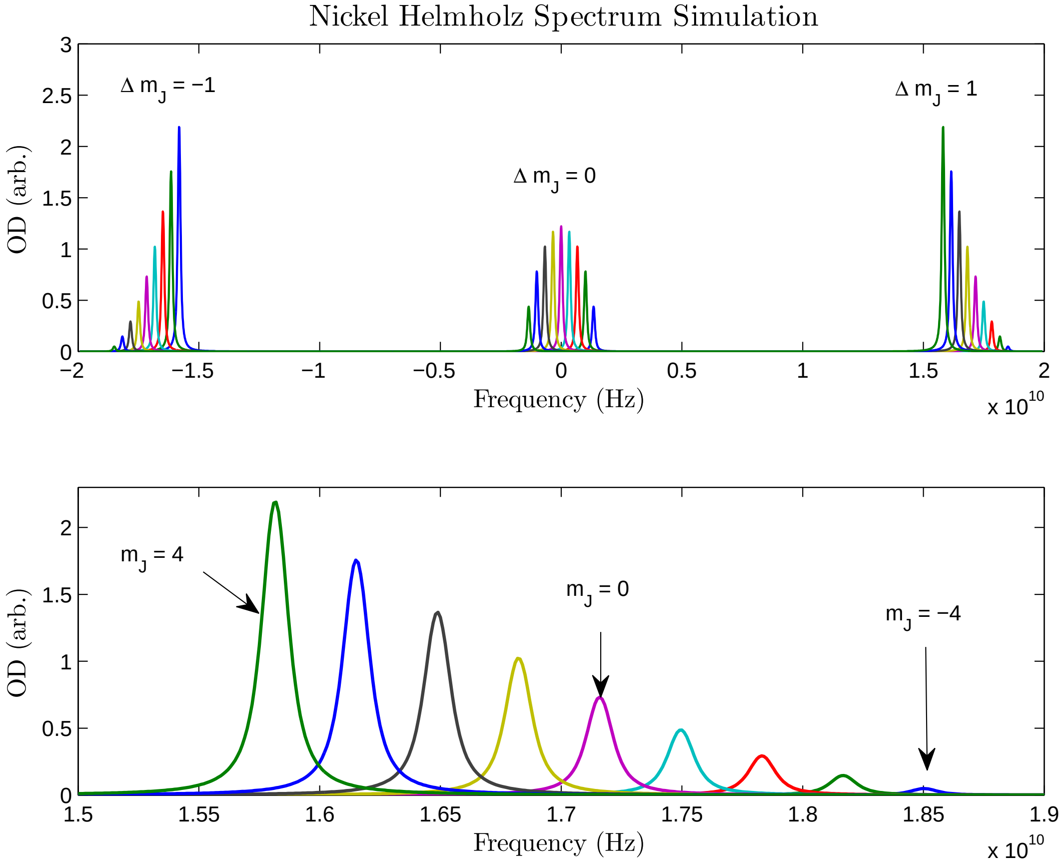

Figure 3-12: Simulated Ni spectrum in 1T Helmholtz field. The upper plot shows the large splitting between the $\Delta m_J = 0, \pm 1$ transitions. The lower plot zooms in on the $\Delta m_J = 1$ transition to show the evenly spaced array of lines associated with the various $m_J$ states. By tuning the laser to the $m_J = 4$(-4) line we can probe the MLFS(MHFS) state population.

optical depth is largest for the $\Delta m_J = 1$ peak due to Clebsh-Gordon coefficients (see Section 3.3.2). The lifetime is measured using the zero-field lifetime procedure described in the previous section with the following caveat. The Zeeman relaxation rate is high and the atoms leave the cell before we can scan the laser repeatedly over the resonance peak. We park at the peak of the resonance and do not scan the laser. This allows us to resolve lifetimes longer than the inverse of our data-taking rate. However, we lose the advantage of subtracting the laser scan baseline, thus degrading our signal to noise.

Using the above procedure we can also study the dynamics of the $m_J = -J$ most high-field seeking (MHFS) state. Diffusion to the walls is the only loss mechanism for the MHFS state. Zeeman relaxation obviously does not occur since the MHFS state is the lowest energy state. For each buffer gas density we measure $\tau_{MHFS}$ and compare it with $\tau_d$. If they are not approximately equal we must look for a systematic effect on lifetime not accounted for in our models presented in Chapter 2.

## 3.4 Laser Systems

### 3.4.1 Ablation

A Q-switched frequency doubled Nd:YAG laser [63] is focused onto the target of interest. Pulses at 532 nm with energy between 5-20 mJ and pulse lengths of $\sim 5$ ns deposit their energy in the target, causing the expulsion of atoms, clusters, and ions from the precursor. The process for optimizing the yield of neutral atoms during ablation is highly empirical and varies by species. We have found it advantageous for most metallic species to focus the laser as tightly as possible onto the metal foil precursor. We accomplish this by expanding the Nd:YAG beam size to several centimeters in a telescope before focusing it onto the target with a 1 meter lens. This creates a smaller spot size at the target and produces larger yields. The focusing lens is on a translation stage and can be moved along the beam path to adjust the location of the focus. The lens can be translated a few centimeters without appreciably changing the ablation yield. For much of our lithium work we did not expand the beam but simply focused the output of the laser onto the target with the 1 m lens. The lithium yields did not improve significantly with the beam expanded setup.

### 3.4.2 Frequency doubled dye lasers

The iron, cobalt, and nickel optical transitions studied are between 230 nm and 350 nm. Frequency doubled dye lasers are used to generate all required ultraviolet frequencies. Dye lasers use organic dyes in solution as the active laser medium. Many dyes are available which cover a wavelength range from roughly 300 - 1300 nm [64].

Because dye gain curves span dozens of nanometers they are often used as highly tunable radiation sources. Table 3.2 shows our dye laser configurations and their operating frequency ranges.

Table 3.2: Dye laser systems and accessible wavelengths

| Dye | Pump Power/Wavelength | Output Wavelength Range |
|---|---|---|
| DCM | 10W/532 nm | 620 - 700 nm |
| Coumarin 480 | 4.5W/406 nm | 470 - 505 nm |
| Coumarin 460 | 4.5W/406 nm | 455 - 500 nm |

We operate two systems, a Coherent 699-21 and a Coherent 899-21 [65]. They are different generations of the same product and operate on the same principle. Dye is dissolved in solvent and stored in a reservoir. A pump draws the dye mixture out of the reservoir and sends it through a precisely machined dye nozzle [66]. The dye jet exiting the nozzle is a free-space flat liquid surface. The pump laser is focused onto the dye jet, causing it to fluoresce brightly. A ring cavity defines the oscillating mode. Intercavity thick and thin etalons allow only a single longitudinal mode. Intercavity transducers include a mirror mounted on a piezo, a Brewster plate, and a thick and thin etalon. Adjusting drive voltages to each of these elements alters the path length of the cavity. The laser is frequency stabilized by tuning the path length such that the frequency stays resonant with an external Fabry-Perot cavity. The resulting linewidth of less than 1 MHz is much narrower than the atomic transitions studied. The laser frequency is scanned by adjusting the optical path length within the stabilization cavity. A Brewster plate is located in the beam path within the Fabry-Perot cavity. The tilt angle of the plate can be varied with a drive voltage. This changes the optical path length inside the cavity which shifts the frequency location of the zero of the locking error signal. The transducers in the laser keep the laser locked to the cavity as the Brewster plate angle changes. Driving the inter-cavity plate with a triangle or sine wave causes the laser to scan repeatedly over the same frequency range. We sweep the laser frequency by driving the Brewster plate with a triangle or sine wave from an SRS DS345 function generator [67].

The 699 has an optics set optimized for Coumarin 480 dye. It is pumped with 4.5

W of 406 nm light from a krypton ion laser. We have used both a Coherent Innova 200 and a Coherent Sabre laser as a pump. Typical output power for Courmarin 480 is $\sim$ 400 mW. The wavelength is tunable between 470-505 nm with a peak in power at $\sim$ 485 nm. Coumarin 460 can also be used in the 699 system with output powers of $\sim$ 200 mW, and tunable wavelength range between 450-500 nm, and a peak in power at $\sim$ 470 nm.

The 699 output is frequency doubled with a Coherent MBD200 resonant frequency doubler. In this system, the 699 output is coupled into a resonant cavity. One of the cavity mirrors is mounted to a piezo which is controlled by a Hansch-Couillaud locking signal [68] to keep the cavity resonant with the incoming fundamental light. A beta barium borate (BBO) [69, p. 98] nonlinear crystal is placed at the focus of the cavity. This maximizes the intensity in the crystal which makes doubling conversion more efficient. Output powers range between 1-10 mW depending on input fundamental frequency and power. A dichroic on the output of the doubler separates the doubled and fundamental frequencies. The output beam is steered from the optics table to the cryogenic dewar. An iris selects the central, uniform intensity portion of the beam to use in spectroscopy.

The Coherent 899 system operates with DCM laser dye [64] and is tunable between 620-690 nm. It is pumped with a 10 W diode-pumped solid state Spectra Physics Millenia at 532 nm. It was used primarily to study trapped copper and silver. However, it was also used briefly to probe nickel and cobalt.

The 899 system does not use a resonant doubler but instead single passes a 5mm × 5 mm × 10 mm lithium iodate ($LiIO_3$) crystal [70]. The crystal is AR coated for 650 nm on the input and 325 nm on the output. Single passing is more convenient than resonant doubling because it does not require simultaneously maintaining the dye laser and doubler lock while scanning the laser for spectroscopy. The DCM dye system has three advantages over the Coumarin dye laser which make single-pass frequency doubling easier than in the Coumarin system. First, its output power is higher. The increase in power is due mostly to the increased pump power. Since the doubling is proportional to $I^2$, this results in more effective doubling. Second, the efficiency of doubling is higher in $LiIO_3$ at 650 nm than in BBO at 486 nm by more than a factor of 3 (calculated from [69, p.50]). Third, the fluorescent cards we use to trace UV beam paths[4] are much brighter at 325 nm than at 240 nm, so even in the absence of more efficient doubling we can run the experiments with less UV power at 325 nm than at 240 nm. We obtain conversion efficiencies of $\sim 0.05$ %/W, yielding roughly 100 $\mu$W for 450 mW fundamental. The fundamental light is filtered out using 3mm of Schott color glass UG11 which absorbs strongly between 410-660 nm but is highly transparent between 390-250 nm [71]. The UV beam diverges quickly in one dimension after exiting the crystal, producing an output beam with a high aspect ratio. We correct for this by sending the beam through a cylindrical lens. The beam is spatially filtered by focusing it through a 50 $\mu$m pinhole. The central airy ring from the pinhole diffraction pattern is collimated to $\sim 0.5$ cm before it is sent to the dewar breadboard for use in spectroscopy.

Our doubling schemes are summarized in Table 3.3.

Table 3.3: Dye laser doubling schemes

| Dye | Doubling Scheme | Doubled Power |
|---|---|---|
| DCM | single passed $LiIO_3$ crystal[70] | 100 $\mu$W |
| Coumarin 480 | Coherent MDB200 resonant doubler | 10-20 mW |
| Coumarin 460 | Coherent MDB200 resonant doubler | 1-5 mW |

---

[4] We have found that a cotton fiber paper works best for this purpose.

# Chapter 4

# Studies of Nickel, Iron, and Cobalt

Measurements of the ratio of elastic to inelastic collisions $\gamma$ were attempted for the transition metals Iron, Cobalt, and Nickel. These elements fall in the first group of transition metals between manganese and copper, both of which have been magnetically trapped in a buffer gas apparatus [11, 21]. A full 4s shell surrounds the valence d electrons of each species. Thus they are "submerged" shell atoms and the interaction anisotropies in collisions with helium buffer gas atoms should be small as has been found for other transition metals [28, 39]. The suppression of the interaction anisotropy results in a large values of $\gamma$, making cobalt, iron, and nickel good candidates for loading into a magnetic trap using the buffer gas cooling method. The large magnetic moments of Fe, Co, and Ni make them easier to trap than the transition metals previously studied. Nickel has been specifically identified as a transition metal likely to have a large value for $\gamma$ [41]. Table 4.1 lists pertinent information for each atom.

| Atom | Configuration | Ground State Term | Magnetic Moment ($\mu_B$) |
|---|---|---|---|
| Fe | [Ar].$3d^6.4s^2$ | $^5D_4$ | 6.005 |
| Co | [Ar].$3d^7.4s^2$ | $^4F_{9/2}$ | 6.003 |
| Ni | [Ar].$3d^8.4s^2$ | $^3F_4$ | 5.002 |

Table 4.1: Electronic properties of iron, cobalt, and nickel.

Each species presented challenges that were overcome with varying degrees of success. Our method for obtaining a value for $\gamma$ does not require direct knowledge of the buffer gas density in the cell. However, this lack of knowledge comes at a price. We must measure $\tau_{MLFS}$ as a function of $\tau_d$. Each $\tau_{MLFS}$ measurement is performed by spectroscopically studying a MLFS state absorption line. Cobalt's rich hyperfine structure made it impossible to isolate MLFS state spectral features. It was therefore impossible to measure $\tau_{MLFS}$ and $\gamma$ could not be found. Nickel studies successfully found a value for $\gamma$ by fitting $\tau_{MLFS}$ vs. $\tau_d$ to models presented in Chapter 2. However, thermal excitation into the MLFS state significantly complicated the nickel analysis compared to previous work with transition and coinage metals [21, 39]. Iron Zeeman relaxation rates were extremely rapid and we never observed a region in buffer gas density where diffusion losses dominated Zeeman relaxation losses. As a result we could not match the data to our models to find a value for $\gamma$. We could, however, set an upper limit.

## 4.1 Cobalt Zeeman Relaxation

Although cobalt's electronic configuration may be favorable for buffer gas trapping and possibly evaporative cooling, the atom has two undesirable features: high electronic angular momentum ($J = 9/2$) and nuclear spin ($I = 7/2$) and a relatively small hyperfine interaction ($\sim 450$ MHz [72]). The resulting high multiplicitiy of states is unfavorable for any applications that requires a pure population, and the high density of Zeeman states prevents observing fully resolved spectra. In spite of these drawbacks, we carried out a study of cobalt to gain experimental experience and to see what we might learn from unresolved relaxation measurements.

The Hamiltonian for an atom with electronic angular momentum $J$ and nuclear spin $I$, hyperfine constant $a$, nuclear g-factor $g_I$, and electronic g-factor $g_J$ in a magnetic field $B$ is

$$H_Z = a\vec{I} \cdot \vec{J} + g_J \mu_B \vec{J} \cdot \vec{B} + g_I \mu_B \vec{J} \cdot \vec{B}. \tag{4.1}$$

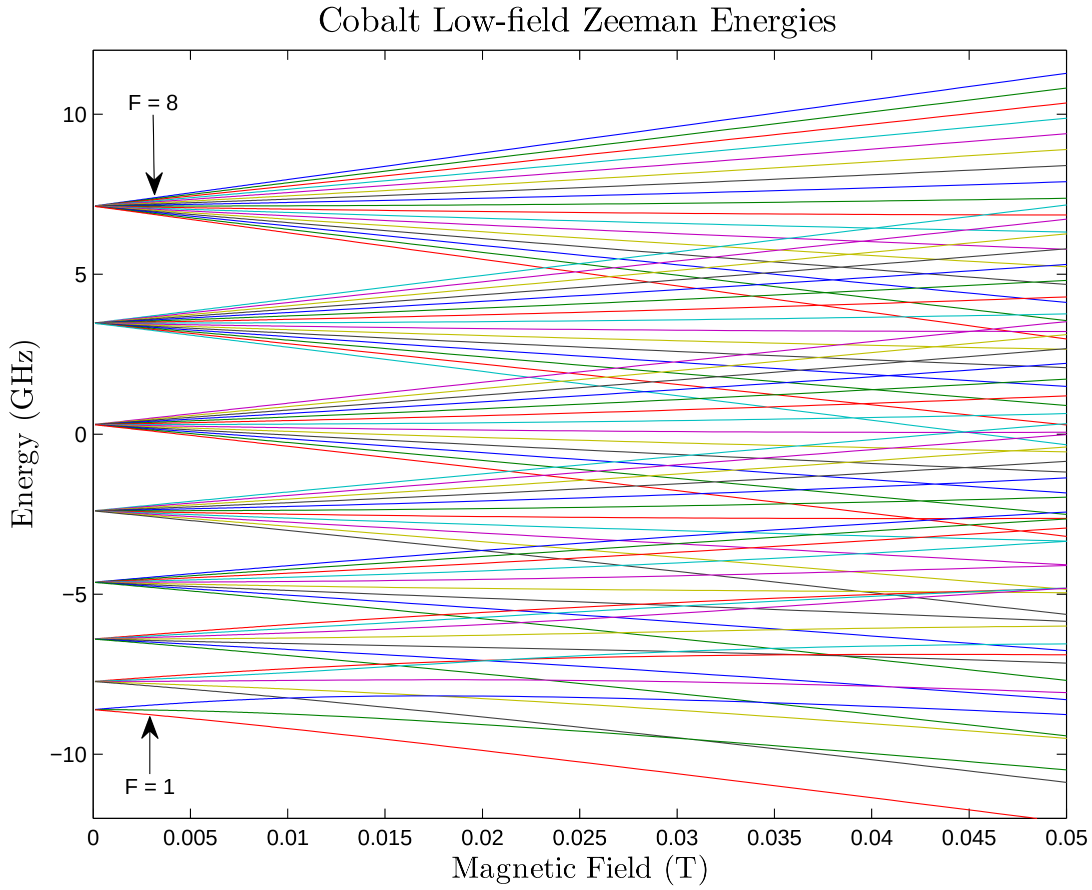

Figure 4-1: Zeeman structure of cobalt at low-field. F is a good quantum number at very low fields. As the interaction with the external field becomes approximately equal to the hyperfine interaction levels start to cross and F is no longer a good quantum number.

Diagonalizing this Hamiltonian[1] is a straightforward task, and the matrix elements in the uncoupled $|J, m_J; I, m_I\rangle$ basis are found in [29, pp. 41-42]. The resulting energy levels as a function of magnetic field are shown in Figures 4-1 and 4-2.

The quantum numbers used to describe Zeeman levels of a species with hyperfine structure depend on the strength of the interaction with the external field relative to the internal interactions. The low-field limit occurs when the interaction between the

---

[1] $a\vec{I} \cdot \vec{J}$ is the magnetic dipole hyperfine interaction commonly referred to as the "hyperfine a" coefficient. There is also a "hyperfine b" coefficient associated with a magnetic quadrupole term in Cobalt. For details see [29, pp. 39-44]. This has been taken into account in the Zeeman state simulation but the details will not be discusses further in this section. The purpose of this section is to demonstrate the high multiplicity of the cobalt spectrum in a magnetic field, which is easily shown without displaying complex hyperfine b terms in the formulas.

nuclear and electronic moments $a\vec{I}\cdot\vec{J}$ is stronger than the interaction of the moments with an external field. In this regime, $\vec{F}=\vec{I}+\vec{J}$ is a good quantum number and takes on values $F = J+I, J+I-1\ldots|J-I|$. Each $F$ manifold contains $2F+1$ states with magnetic projection quantum numbers $m_F = -F, -F+1\ldots F$. The interaction with the external field results in a Zeeman shift

$$E_Z(B) = g_F m_F \mu_B B \tag{4.2}$$

$$g_F \approx g_J \frac{F(F+1) - I(I+1) + J(J+1)}{2F(F+1)} \tag{4.3}$$

The cobalt electronic ground state manifold contains states $F$ = 8,7,. . . 1. Figure 4-1 shows the low-field behavior. There are 80 states. As the field strength increases, the $|F, m_F\rangle$ states begin to cross and $F$ is no longer a good quantum number.

In the high-field limit both the nuclear and electronic moments couple to the external field and $I$ and $J$ are good quantum numbers instead of $F$. The dominant interaction $E_Z(B) = g_J m_J \mu_B B$ is between the electronic angular momentum and the external field. However, the hyperfine interaction perturbs these energy levels with an energy splitting equal to $a m_J m_I$. The left side of Figure 4-2 plots cobalt energy levels out to the high field regime. There are 10 energy level slopes attributed to the 10 $m_J$ states. Within each $m_J$ manifold there are 8 states corresponding to different values of $m_I$ as shown on the right side of Figure 4-2.

| Atom | Ground State | Excited State | Wavelength (nm) | $g_{Jg}$ | $g_{Je}$ | Einstein A ($s^{-1}$) |
|---|---|---|---|---|---|---|
| Co | $a^4F_{9/2}$ | $z^4D_{7/2}$ | 341.36 | 1.32 | 1.425 | $1.2 \times 10^7$ |
| Co | $a^4F_{9/2}$ | $x^4G_{11/2}$ | 240.80 | 1.32 | 1.291 | $3.6 \times 10^8$ |
| Co | $a^4F_{9/2}$ | $x^4F_{9/2}$ | 242.57 | 1.32 | 1.319 | $3.2 \times 10^8$ |
| Fe | $a^5D_4$ | $x^5F_5$ | 248.40 | 1.495 | 1.390 | $4.9 \times 10^8$ |
| Ni | $a^3F_4$ | $z^3D_3$ | 337.05 | 1.25 | 1.3 | $1.8 \times 10^8$ |
| Ni | $a^3F_4$ | $x^3D_3$ | 234.63 | 1.25 | 0.840 | $2.2 \times 10^8$ |
| Ni | $a^3F_4$ | $y^3G_5$ | 232.07 | 1.25 | 1.226 | $6.9 \times 10^8$ |

Table 4.2: Optical transitions observed in Co, Fe, and Ni. All values taken from [73]

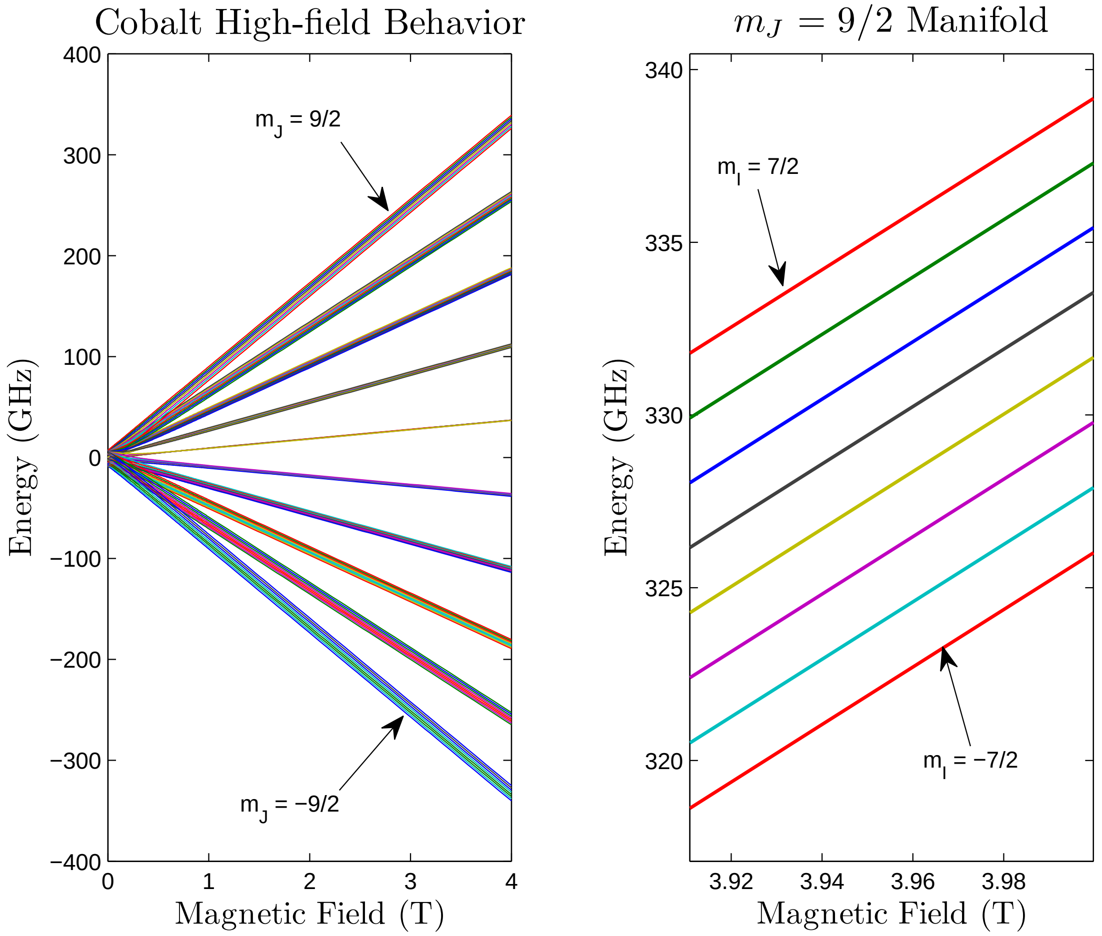

Figure 4-2: Zeeman structure of Cobalt in high magnetic fields. The energy splittings are dominated by the projection of the electronic angular momentum onto the external field so J is a good quantum number. Each of the 10 $m_J$ manifolds contain 8 states corresponding to different values of $m_I$.

The spectral lines observed in Co, Ni, and Fe are listed in Table 4.2. For most of our cobalt studies we observed the atoms by monitoring the $a^4F_{9/2} \rightarrow x^4G_{11/2}$ transition at 240.8 nm because of its large transition strength. The zero-field spectrum of this transition splits into many lines due to the 80 ground states. Figure 4-3 shows a simulation of the hundreds of lines in the Cobalt spectrum at a field of 1 Tesla. (It has been assumed that the excited state hyperfine constants are zero for simplicity.) The lower plot is a blow up of the $\Delta m_J = 1$ transitions. Transitions from the $m_J = J (m_J = -J)$ ground states are in blue(black). All other transitions are red. There are $\sim$ 240 transitions from the electronic ground state (80 ground states, $\Delta m_J = 0, \pm 1$ from each state). The optical depth of the individual lines will be reduced dramatically compared to the optical depth at zero-field. In addition to the loss of optical depth, the hyperfine induced splitting of each $m_J$ manifold causes absorption lines of different $m_J$ states to overlap. Notice in the lower plot of Figure 4-3 that only one of the $m_J = J$ absorption peaks is isolated from other $m_J$ states. Due to the overlap of lines and decreased OD for individual transitions we found it impossible to experimentally isolate an $m_J = J$ state peak.

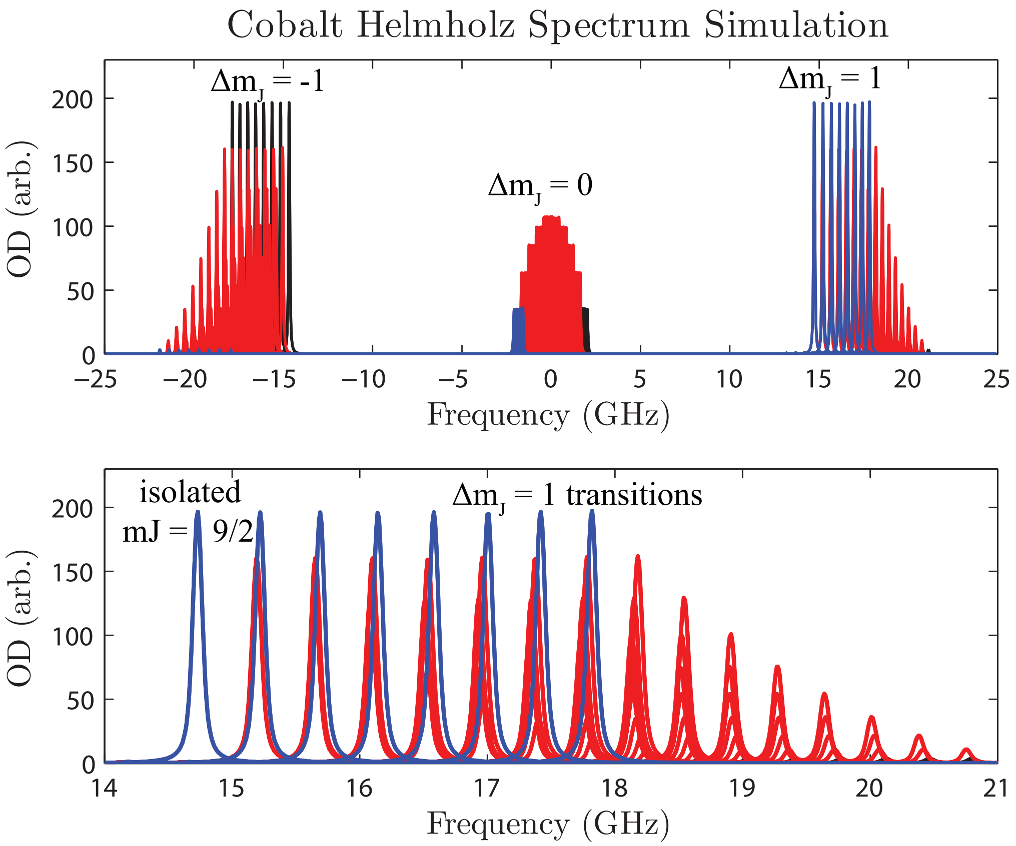

Figure 4-3: Cobalt in 1T Helmholtz Field. Transitions from the $m_J = J(m_J = -J)$ states are in blue(black). The $m_J = J$ line is split into several lines corresponding to different values of $m_I$. There is only one $m_J = J$ state transition that does not overlap with any other spectral line. Due to the large multiplicity of transitions in cobalt, the OD of the isolated transition will be lower at a given density than the $m_J = J$ lines in Fe and Ni. The linewidths of the above spectra include only the natural linewidths. In our experiment we have additional Doppler and magnetic broadening. The observed linewidths are $\sim$ 200-300 MHz.

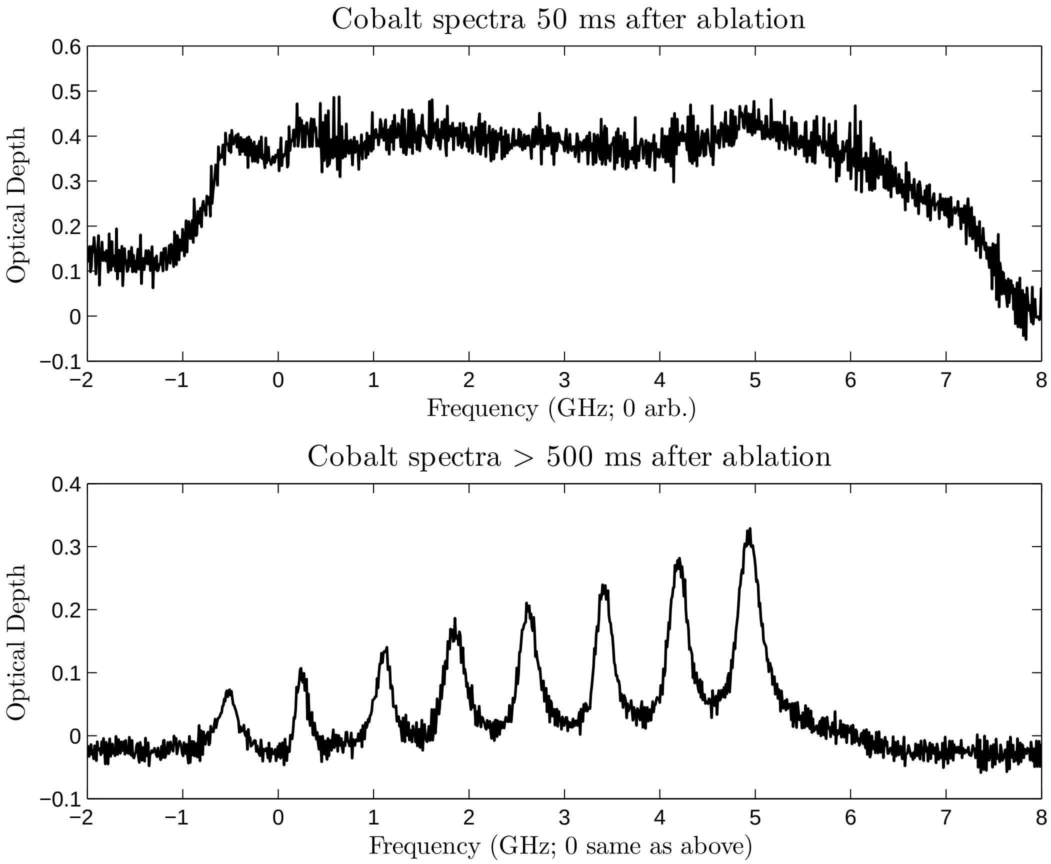

Figure 4-4: Zeeman relaxation of Cobalt in a 1.9T Helmholtz field. Immediately after ablation the $\Delta m_J = -1$ spectrum is very broad and mostly featureless due to the immense number of overlapping lines from the 10 $m_J$ manifolds. Clearly there is no isolated $m_J = J$ line. The lower plot shows the average of several spectra taken $>$ 500 ms after ablation. Zeeman relaxation has caused a population purification into the $m_J = -J$ state. The hyperfine interaction splits the $m_J = -J$ state manifold into 8 lines corresponding to the 8 $m_I$ states.

Figure 4-4 shows the observed cobalt spectrum for $\Delta m_J = -1$ transitions. The spectrum in the upper(lower) plot was take 50(500) ms after ablation. A nearly featureless absorption signature is observed 50 ms after ablation because there is population in all of the $m_J$ states and their spectral lines overlap. The flatness of the spectrum is a polarization effect. The magnetic field and probe beam wave vector are both pointed along the cell axis. In this geometry no $\Delta m_J = 0$ transitions occur. These require a polarization component along the magnetic field whereas our polarization is perpendicular to the magnetic field. The light entering the cell is a mix of right-handed $\sigma^-$ and left-handed $\sigma^+$ circularly polarized light. Only $\sigma^+(\sigma^-)$

polarization can drive the $\Delta m_J = 1(-1)$ transition. As can be seen in Figure 4-3, the splitting between the $\Delta m_J = 1$ and $\Delta m_J = -1$ transitions is tens of GHz. The laser can be tuned to center on either the $\Delta m_J = 1$ or the $\Delta m_J = -1$ peaks but not both. For the $\Delta m_J = 1$ transitions the $\sigma^+$ polarization component of the laser beam is absorbed, but the $\sigma^-$ component travels through the cloud unattenuated and will be detected on the PMT regardless of the density of the atomic sample. Assuming nearly linearly polarized light, there are roughly equal amounts of $\sigma^+$ and $\sigma^-$ polarizations and the maximum optical depth is therefore $\sim 0.5$ even when the density of atoms is high. We see this in the data for the early time behavior in the upper plot of Figure 4-4.

After waiting 500 ms we see clear features as shown in the lower plot of Figure 4-4. Zeeman relaxation from higher energy Zeeman states leads to an increase in population of the $m_J = -J$ states. The distinct spectral lines are the $m_J = -J$ transitions separated by the high-field hyperfine splitting. There are 8 clear features at long times corresponding to the 8 $m_I$ states. We therefore observe a purification of essentially all of the $m_J$ states into the $m_J = -J$ state as time progresses. The is evidence that higher energy $m_J$ states are Zeeman relaxing into the $m_J = -J$ state.

## 4.2 Nickel: Measurement of $\gamma$

Nickel has been proposed as a good candidate for trapping because the calculated interaction anisotropies are small [41], which suggests that $\gamma$ may be very high. Therefore its Zeeman relaxation rate for collisions with helium should be small and the MLFS state lifetime should be long enough to measure with our experimental procedure.

### 4.2.1 Measurement of nickel MLFS lifetimes

Nickel's spectrum in a magnetic field is relatively simple due to its lack of hyperfine structure. Only one of its naturally occurring isotopes, $^{61}$Ni, has nuclear spin (I = 3/2), and its natural abundance is only 1%. The most common isotopes, $^{58}$Ni,$^{60}$Ni,

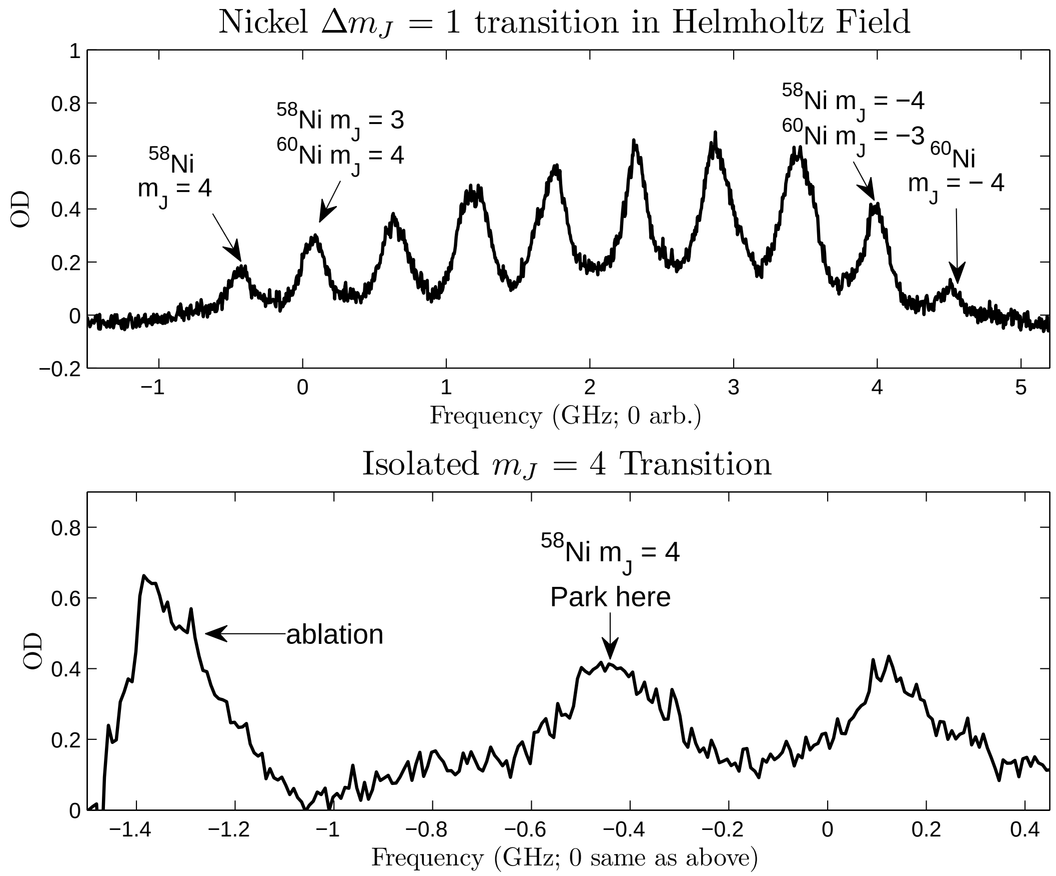

Figure 4-5: Nickel spectrum in Helmholtz field. Each isotope has 9 lines corresponding to the 9 $m_J$ states. The Zeeman and isotope shifts are roughly equal at 0.8T fields, causing lines of different isotopes to overlap. Measurements of MLFS state lifetime are performed by parking on the $m_J = J$ transition peak and measuring the optical depth versus time.

and $^{62}$Ni have no nuclear spin and natural abundances of 68%, 26%, and 4% respectively. Because the dominant isotopes have no nuclear spin, hyperfine effects are absent. Compared to cobalt, the nickel spectrum splits into fewer lines in a magnetic field, so the decrease in optical depth for each transition is less dramatic. The ground state splits into 9 lines for each isotope corresponding to the $m_J$ ground states. Figure 4-5 shows the observed $\Delta m_J = 1$ transitions. The appearance of 10 lines is understood by considering the isotope shifts. The Zeeman splitting at $B \sim 0.8$T is approximately equal to the isotope shift between $^{58}$Ni and $^{60}$Ni. As a result, transitions from the $^{58}$Ni $m_J$ state overlap with $^{60}$Ni transitions from the $m_J + 1$ state.

Only the $^{58}$Ni $m_J = J$ and $^{60}$Ni $m_J = -J$ states do not experience any overlap. The overall result is 10 absorption features, 8 of which contain transitions from two isotopes. We measure $\tau_{MLFS}$ by tuning the laser frequency to the fully resolved $^{58}$Ni $m_J = 4$ absorption peak and observing the decay of the absorption signal.

The lifetime of the most high-field seeking (MHFS) state should match the diffusion lifetime because it does not experience Zeeman relaxation loss. We confirm this experimentally by measuring $\tau_{MHFS}$ at each buffer gas density. To make the measurement we tune the laser to the MHFS fully resolved $\Delta m_J = -1$ transition because the Clebsch-Gordon coefficients for this transition are much larger than for the $\Delta m_J = 1$ transition (see discussion in Section 3.3.2).

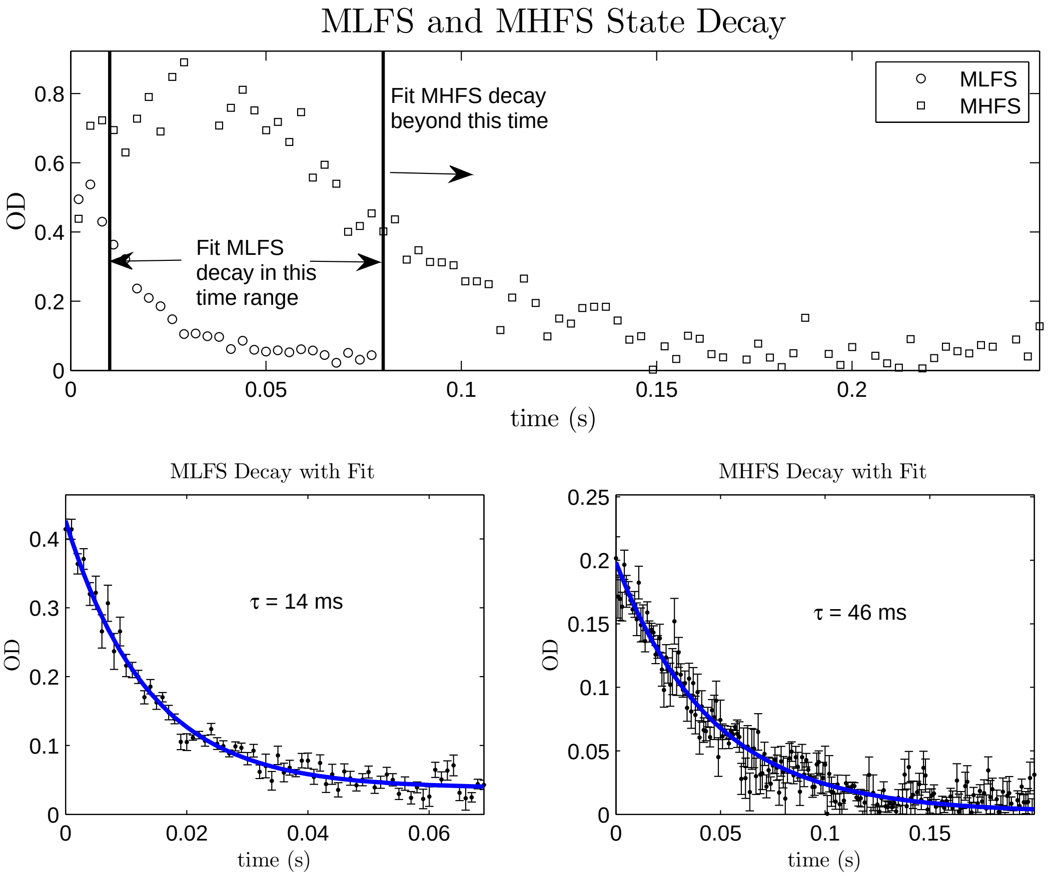

Figure 4-6: Nickel MLFS and MHFS decay with fits to lifetime. The MHFS state experiences an initial increase in optical depth because higher Zeeman states are relaxing into the MHFS state.

As described in Section 3.3.5, the preferred spectroscopic method is to scan the laser repeatedly over the resonance, average the optical depth over each spectrum, and subtract a baseline. This removes low frequency noise. The longest measured lifetime out of the $m_J = J$ state was $\sim$ 20 ms. Measuring lifetimes on this time scale is certainly possible but the laser cannot be scanned quickly enough to use the baseline subtraction method. Instead we park the laser frequency at the peak of the transition, measure the decay of the peak OD, and cope with the increased noise in the data. Figure 4-6 shows an example of MLFS and MHFS state decay with fits to a single exponential lifetime.

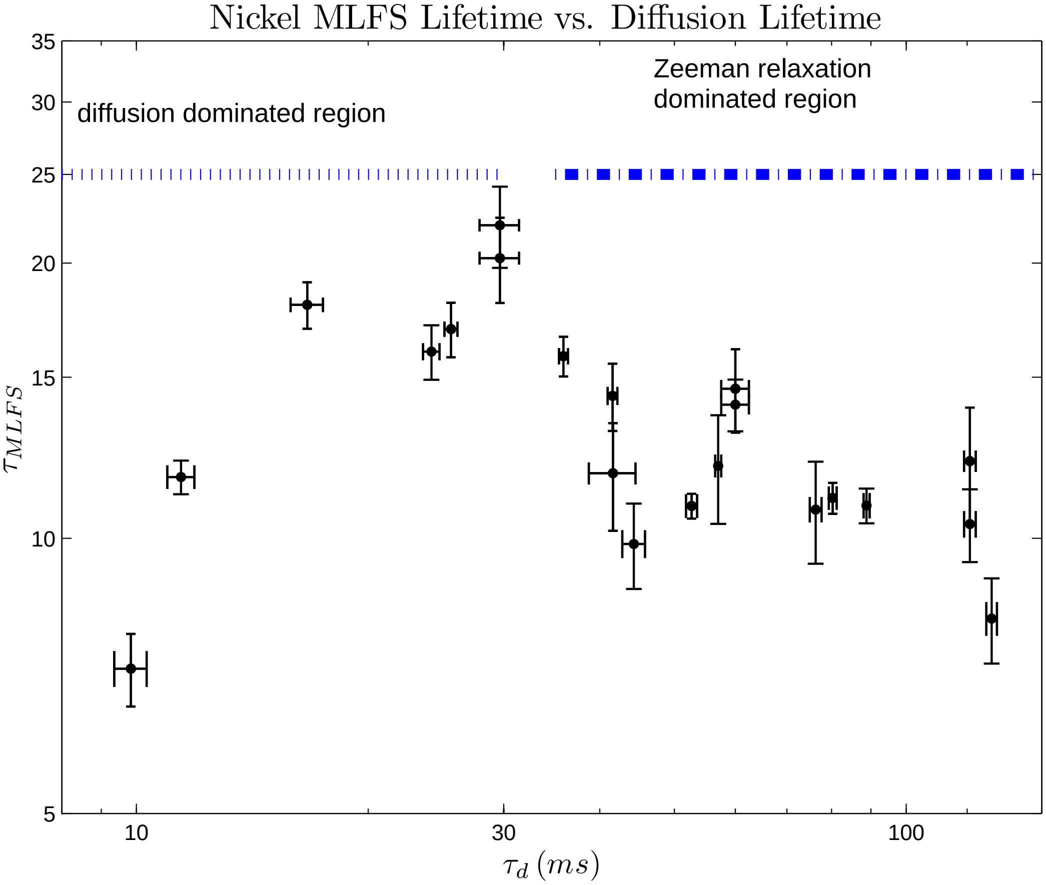

Figure 4-7: Nickel $\tau_{MLFS}$ vs. $\tau_d$. We observe a region at low $\tau_d$ where the MLFS state lifetime increases with $\tau_d$, a signature of diffusion to the walls. As $\tau_d$ increases to approximately 30 ms the Zeeman relaxation rate equals the diffusion loss rate. Increasing $\tau_d$ beyond this point causes the measured $\tau_{MLFS}$ to decrease.

As explained in Section 3.3.5, measurements of $\tau_{MLFS}$ and $\tau_{MHFS}$ were made at several buffer gas densities spanning an order of magnitude. Our buffer gas density is characterized by measurements of diffusion lifetime $\tau_d$ at zero-field as discussed in 3.3.4. Our model predicts that there should exist a low buffer gas density region in which diffusion losses dominate Zeeman relaxation losses. In this region, increasing buffer gas density should lead to an increase in the MLFS state lifetime. At high buffer gas densities Zeeman relaxation dominates and increasing buffer gas density should result in a decrease in MLFS state lifetime. We expect to observe a crossover region at intermediate buffer gas densities where the diffusion and Zeeman relaxation lifetimes are comparable. Observation of this crossover gives us confidence that we understand the physical processes involved in the measurement of $\gamma$. Figure 4-7 shows measured values of $\tau_{MLFS}$ vs. measured values of $\tau_d$. Below $\tau_d \sim 30$ ms the observed $\tau_{MLFS}$ increases as $\tau_d$ increases. This is evidence that atom loss is dominated by diffusion to the walls. At higher buffer gas densities, however, $\tau_{MLFS}$ levels out and begins to decrease. This is the transition region where Zeeman relaxation becomes dominant. These qualitative trends match the model and $\gamma$ can be determined. However, the scatter in the data and uncertainties in the Zeeman Cascade model described in Chapter 2 will limit the precision to which the measurement of $\gamma$ can be determined. We will return to these topics later.

### 4.2.2 Measurement of nickel temperature

We determine $\gamma$ by measuring the lifetime of the MLFS state as a function zero-field diffusion lifetime and comparing the measurements with the Zeeman Cascade model developed in Chapter 2. In order to correctly incorporate collisional excitations into the model we also need to measure temperature accurately. Temperature, density, and diffusion lifetimes are found by measuring the zero-field nickel spectrum. The density is proportional to peak height of the absorption signal. The lifetime is found by measuring the absorption as a function of time. We find temperature by fitting the zero-field spectrum to a Voigt profile as discussed in Section 3.3.3. Figure 4-8 shows the zero-field spectrum of the $a^3F_4 \rightarrow y^3G_5$ transition at 232 nm taken 50 ms after ablation. The density is $\sim 3 \times 10^9$ cm$^{-3}$ which corresponds to $3 \times 10^{11}$ Ni atoms in the cell. The temperature of the atoms is determined by fitting to a Voigt profile as discussed in Section 3.3.3.

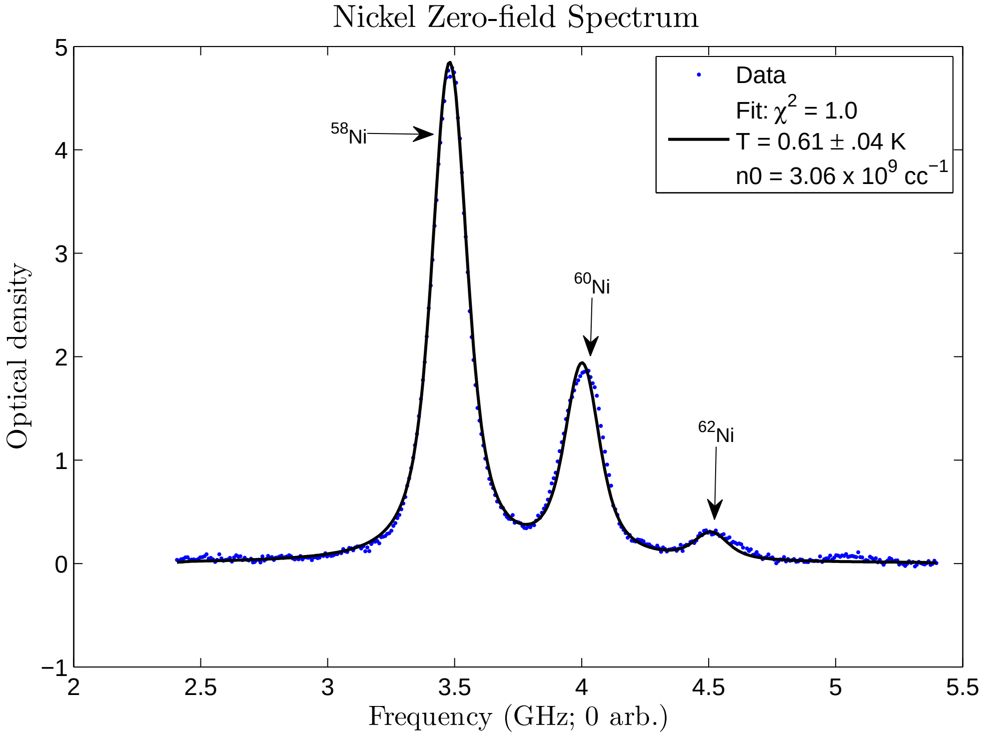

Figure 4-8: Nickel zero-field spectrum 50 ms after ablation. Temperature and density are found by fitting to a Voigt profile.

Temperatures were measured at three buffer gas densities. Figure 4-9 shows the temperature of the nickel atoms as a function of time in the cell. The observed temperature is $\leq$ 1K for all buffer gas densities used. As discussed in Chapter 2, thermal excitations into the MLFS state have the greatest impact at high buffer gas densities when the Zeeman relaxation rate is much faster than the diffusion rate. We therefore use the average temperature measured at the highest buffer gas density for the rest of the data analysis. These measurements are marked with squares in the figure. The average temperature is 750 mK which we assume is the best temperature to use in the Zeeman Cascade simulations. Clearly thermal effects must be included in the analysis because the nickel Zeeman energy spacing is 670 mK at the 0.8 T magnetic field used to resolve the MLFS absorption peak.

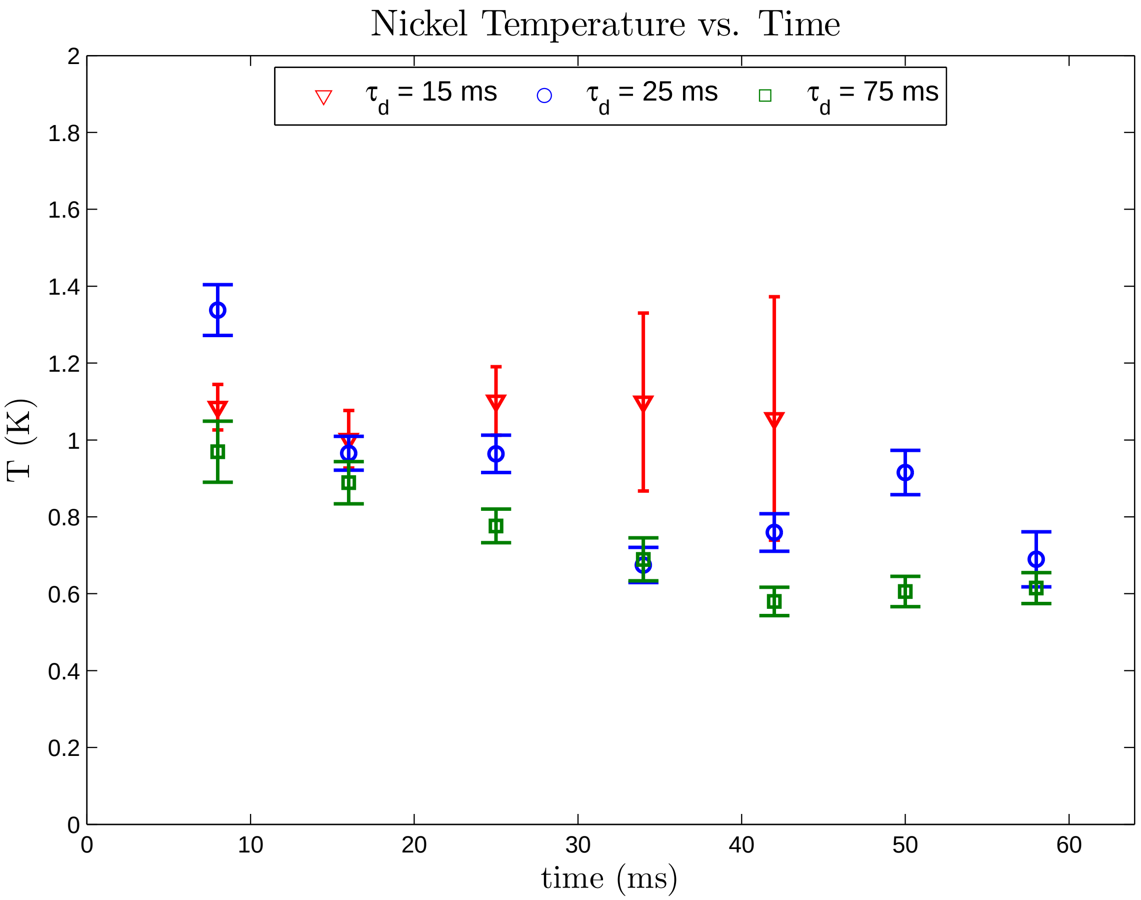

Figure 4-9: Nickel temperature versus time. Temperature measurements were made at 3 different buffer gas densities. The atoms cool only slightly over the time scale of our $\tau_{MLFS}$ measurements. The temperature is slightly higher at lower buffer gas densities.

### 4.2.3 Determination of $\gamma$

We fit our measurements of $\tau_{MLFS}$ vs $\tau_d$ to a Zeeman Cascade simulation with $\gamma$ as the only fit parameter. A detailed explanation of the Zeeman Cascade simulations is found in Section 2.3.6. The result of the fit is influenced by the choice of atom temperature and the "selection rules" used to model the Zeeman Cascade. We will explore these choices in due coarse, but for now we assume a temperature of 750 mK and the most realistic selection rules based on the literature (see Table 2.1).

Our data consists of a set values of $\tau_{MLFS}$ measured at several buffer gas densities corresponding to zero-field lifetimes $\tau_d$. For each value of $\tau_d$ in the data set, a Zeeman Cascade simulation is performed. Each simulation requires input values for

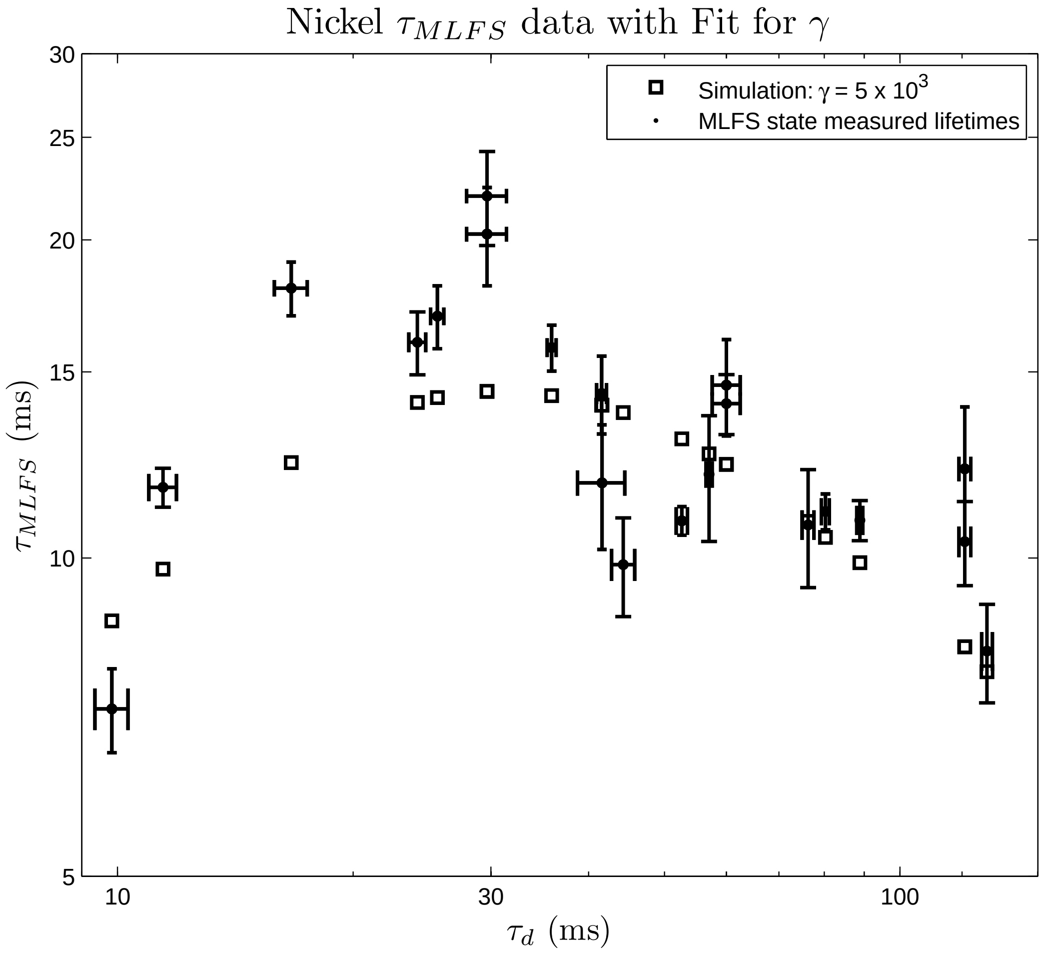

Figure 4-10: Nickel Data with fit to Zeeman Cascade simulation. The squares are the best fit simulations to the data, yielding a value of $\gamma = 5 \times 10^3$. Agreement with the model is poor for low values of $\tau_d$.

the diffusion rate $\Gamma_d$, the Zeeman relaxation rate $\Gamma_{zr}$, and atom temperature $T$. We use $T = 750$ mK obtained from fitting the zero-field spectrum and $\Gamma_d = 1/\tau_d$. The input value for $\Gamma_{zr}$ is calculated from Equation 2.26: $\Gamma_{zr} = (\overline{v}^2\tau_d\chi)/\gamma$ where $\overline{v} \propto T$ and $\chi$ is a known geometric factor. Each simulation therefore depends on the input parameter $\gamma$. We obtain experimental values for $\tau_{MLFS}$ by fitting the decay of the absorption signal to a single exponential function. The calculated MLFS state decay is fit to an exponential function in a similar manner to generate a simulated $\tau_{MLFS}$. This procedure generates a $\gamma$ dependent, simulated $\tau_{MLFS}$ for each value of measured $\tau_d$. A least squares fit of the data to these simulated data sets is performed to find the value of $\gamma$.

Figure 4-10 plots $\tau_{MLFS}$ data with the best fit we were able to achieve. The data displays the qualitative trends predicted by the model: a diffusion dominated region at low $\tau_d$ and a Zeeman relaxation dominated region at high $\tau_d$. The simulated results were achieved using $\gamma = 5 \times 10^3$. However, the quantitative agreement between the MLFS data and the model is not impressive. At low buffer gas densities where diffusion dominates the agreement with the Zeeman Simulation is quite poor.

Variations in the value of $\gamma$ determined by fitting the data to the simulations are caused by three effects. First, it is not possible to find a value of $\gamma$ that agrees well with the data at both the high $\tau_d$ and low $\tau_d$ regions and we have no reason to trust one region of the data over the other. Second, uncertainty in the atom temperature leads to uncertainty in the thermal excitation rates used in the simulations. Finally, the assumed selection rules for $\Delta m_J$ affect the thermal excitation rates between Zeeman levels. We address each topic in the following sections.

First let's examine the data set. The qualitative agreement between the trends in the data is in agreement with the model: a rise in $\tau_{MLFS}$ at low buffer gas densities followed by a decrease in $\tau_{MLFS}$ at high buffer gas densities. The MLFS state lifetimes are plotted with the MHFS state lifetimes in Figure 4-11. The clear differentiation between the MLFS state and MHFS state behaviors provides evidence that we are measuring Zeeman relaxation of the MLFS state. The MHFS state lifetimes are approximately $\tau_d$ as expected, whereas the MLFS state lifetimes decrease with increasing $\tau_d$. However, when the entire MLFS data set is fit to the Zeeman Cascade simulation, the agreement with the fit is better at high values of $\tau_d$ than at low values of $\tau_d$. We cannot simultaneously fit both regions well for any input value of $\gamma$. Figure 4-12 illustrates the problem. The data is plotted with two simulated data sets. The first uses our value of $\gamma = 5 \times 10^3$ while the second uses $\gamma = 1.1 \times 10^4$. Increasing $\gamma$ implies a decrease in the Zeeman relaxation rate. This raises the MLFS lifetimes for all values of $\tau_d$ and the agreement between the model becomes better in the diffusion dominated region. However, this results in poor agreement in the Zeeman relaxation dominated region. We cannot simultaneously obtain good fits in both regions. It is as if the transition between the diffusion dominated and Zeeman relaxation dominated

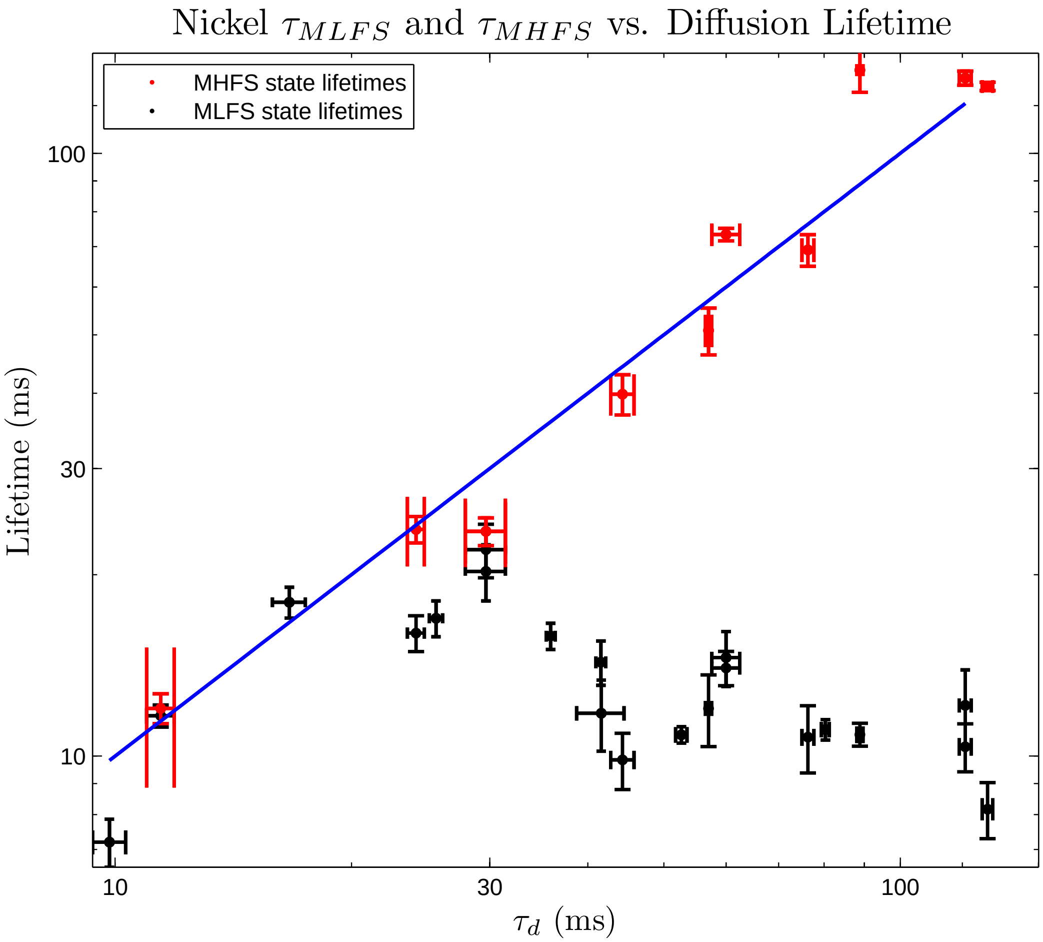

Figure 4-11: Nickel MLFS and MHFS data. The blue line has slope = 1 to demonstrate that the MHFS atoms leave the cell by diffusion as expected. The MLFS atoms decay quickly due Zeeman relaxation in the region of high $\tau_d$.

regimes occurs more rapidly than predicted by our model. Alternatively there is an unknown experimental artifact that is causing the agreement with the model to be poor in one of the regimes.

It is possible to quantify this problem by systematically ignoring data on the high $\tau_d$ end of the data set and refitting the remaining data to the model. In effect we are adding weights to the low $\tau_d$ end of the data set. Table 4.3 displays the result of this procedure. When we ignore all data taken at $\tau_d > 30\,ms$, the best fit for $\gamma$ changes from $5 \times 10^3$ to $1.1 \times 10^4$; roughly a factor of two difference. We do not have a convincing reason to prefer one value over the other, so we can only claim that a value of $\gamma$ between $5 \times 10^3$ to $1.1 \times 10^4$ is consistent with our data set. Arbitrarily

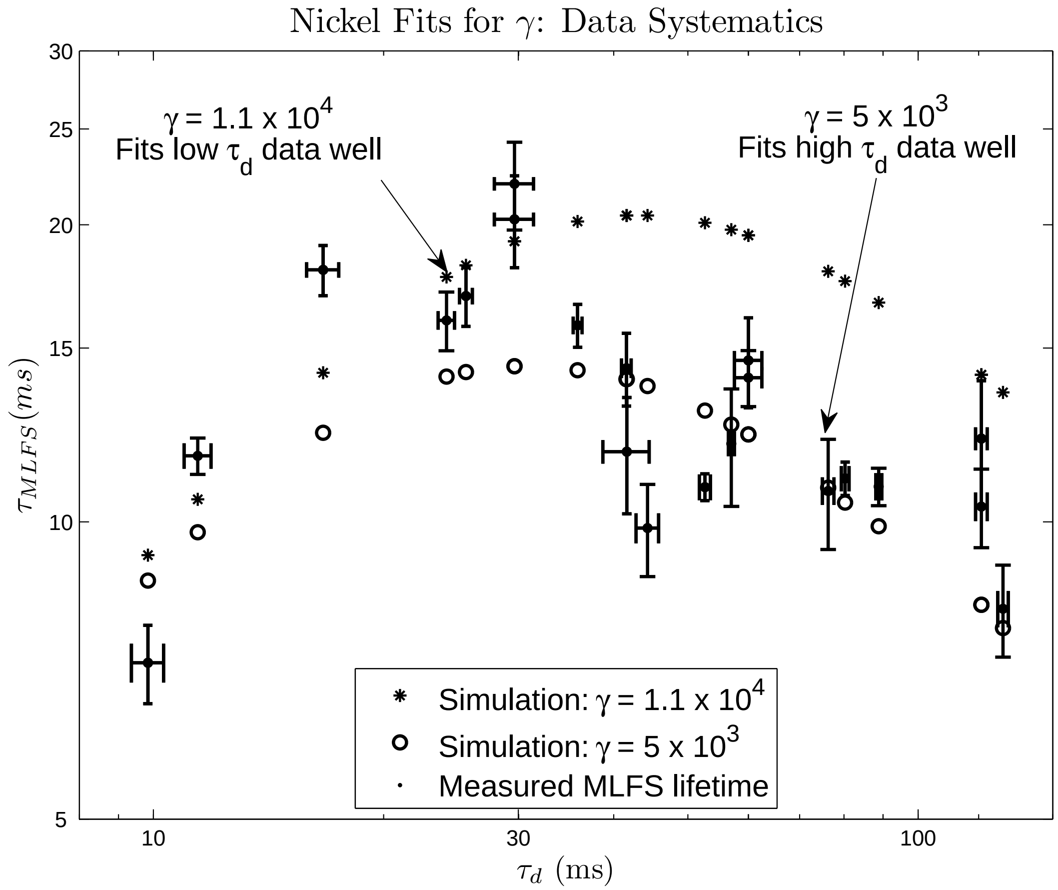

Figure 4-12: The above simulations assumed T = 750 mK and realistic selection rules. It is not possible to find a value of $\gamma$ that fits both the low $\tau_d$ and high $\tau_d$ regions of our data. There may be a systematic effect not fully understood that causes a deviation from the model in one of the regimes. This effect creates an uncertainty of a factor of 2 in the final value of $\gamma$.

| Data Ignored | Fit for $\gamma$ |
|---|---|
| None | $5 \times 10^3$ |
| $\tau_d < 100$ ms | $5 \times 10^3$ |
| $\tau_d < 70$ ms | $5 \times 10^3$ |
| $\tau_d < 50$ ms | $6 \times 10^3$ |
| $\tau_d < 40$ ms | $8 \times 10^3$ |
| $\tau_d < 30$ ms | $1.1 \times 10^3$ |

Table 4.3: Change in $\gamma$ due to omitting parts of the data when fitting to Zeeman Cascade Simulations. By omitting data in the high $\tau_d$ regime the fits more closely match the low $\tau_d$ regime.

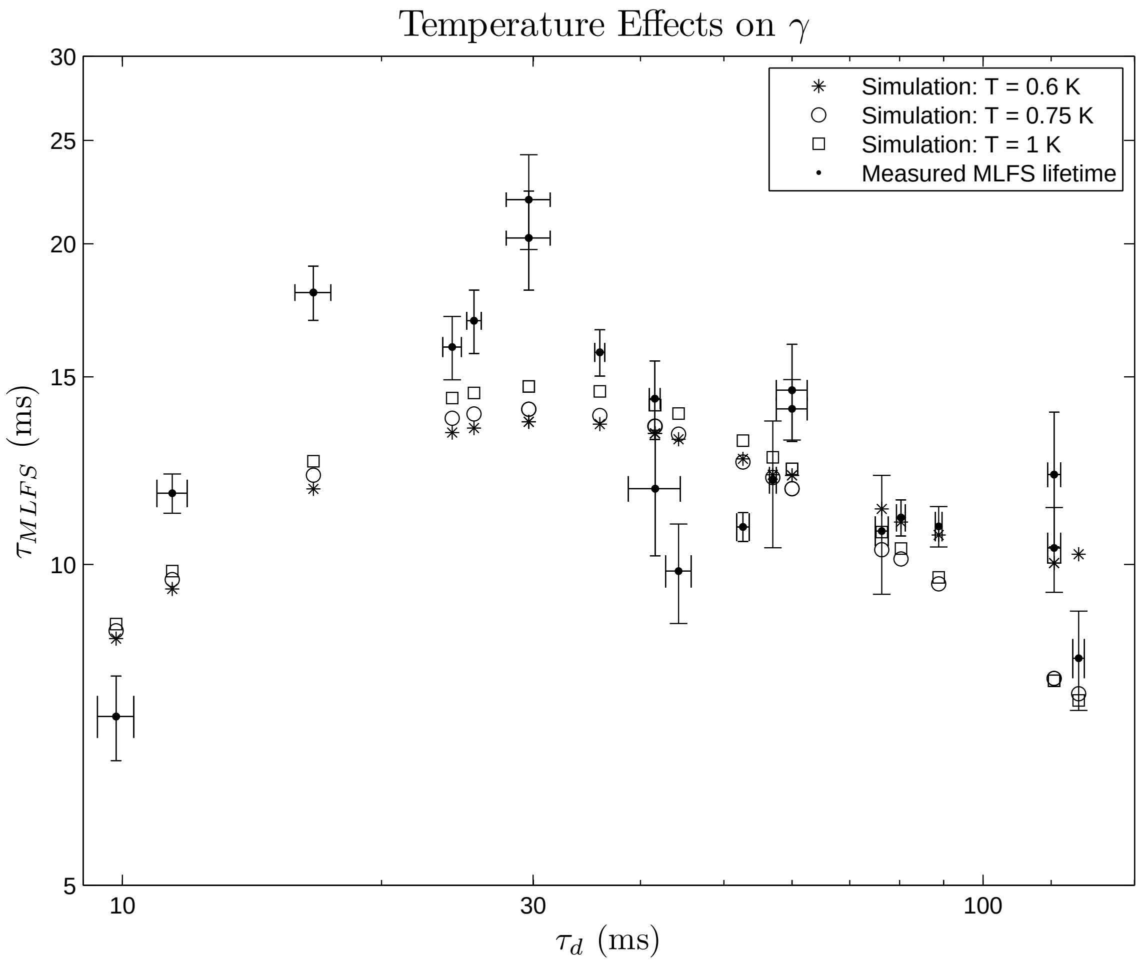

Figure 4-13: Temperature effects on $\gamma$. The curves were calculated assuming realistic selection rules and $\gamma = 5 \times 10^3$. Although changing temperature does change the predicted behavior, it is not significant compared to the effects of assumed selection rules and the poor quality of the fits to the data.

large values of $\gamma$ are consistent with the low $\tau_d$ region of the data because increasing $\gamma$ does not change the predicted behavior in the diffusion dominated regime. However, larger values of $\gamma$ are completely inconsistent with the high $\tau_d$ data.

We next explore the effect on the fit for $\gamma$ caused by uncertainties in atom temperature and Zeeman relaxation selection rules. The effect is quantified by systematically varying the temperature and selection rule inputs when we fit out data to Zeeman cascade simulations to determine $\gamma$. As described in the following paragraphs, we use 3 temperatures and 3 selection rules resulting in a total 9 fits for $\gamma$. The spread in the values of $\gamma$ obtained from these 9 fits determines the uncertainty.

The average measured temperature in Figure 4-9 is 0.75K while the temperature extremes are approximately 1K and 0.6K. Using these three temperatures as inputs into the simulation, the fit value of $\gamma$ changes by $\sim 1 \times 10^3$ for all selection rule assumptions as can be seen in Table 4.4. This effect is insignificant compared to the previously discussed uncertainty in $\gamma$ caused by the systematics in the data. Figure 4-13 shows the relatively small effect of changing temperature on the Zeeman simulation.

Finally we consider the effects of the assumed selection rules for Zeeman relaxation. It is energetically possible for the MLFS state to decay into any lower Zeeman state. However, the Zeeman relaxation rates into the lower lying states are not equal. It is more likely to change $m_J$ by 1 or 2 than by 7 or 8. There is no obvious expression for how the rates scale as $\Delta m_J$ increases. We refer to the relative scaling of the Zeeman relaxation rates as the "selection rules". Much insight is gained from the literature and the simulations assume a realistic estimate for the $\Delta m_J$ transition rates as discussed in Section 2.3. It was found in Section 2.3 that the collisional

| Thermal Effects Considered? | Temperature | Selection Rules | Fit for $\gamma$ | $\chi^2$ |
|---|---|---|---|---|
| Yes | 0.6K | From Literature | $5 \times 10^3$ | 143 |
| Yes | 0.6K | All Equal | $6 \times 10^3$ | 153 |
| Yes | 0.6K | $\Delta m_J = 1$ | $3 \times 10^3$ | 149 |
| Yes | 0.75K | From Literature | $5 \times 10^3$ | 145 |
| Yes | 0.75K | All Equal | $7 \times 10^3$ | 145 |
| Yes | 0.75K | $\Delta m_J = 1$ | $2 \times 10^3$ | 160 |
| Yes | 1.0K | From Literature | $5 \times 10^3$ | 141 |
| Yes | 1.0K | All Equal | $7 \times 10^3$ | 127 |
| Yes | 1.0K | $\Delta m_J = 1$ | $2 \times 10^3$ | 173 |
| No | 0.6K | N/A | $7 \times 10^3$ | 158 |
| No | 0.75K | N/A | $9 \times 10^3$ | 158 |
| No | 1.0K | N/A | $1.2 \times 10^4$ | 159 |

Table 4.4: Values of $\gamma$ extracted from fits of data to Zeeman cascade simulations under various temperature and selection rules assumptions. The $\chi^2$ for the fits are similar enough that it is difficult to identify a particular case as being clearly more correct that the others. We claim that $\gamma = 5 \times 10^3$ is the most probable value of $\gamma$ because it was determined from the data using the most realistic selection rules.

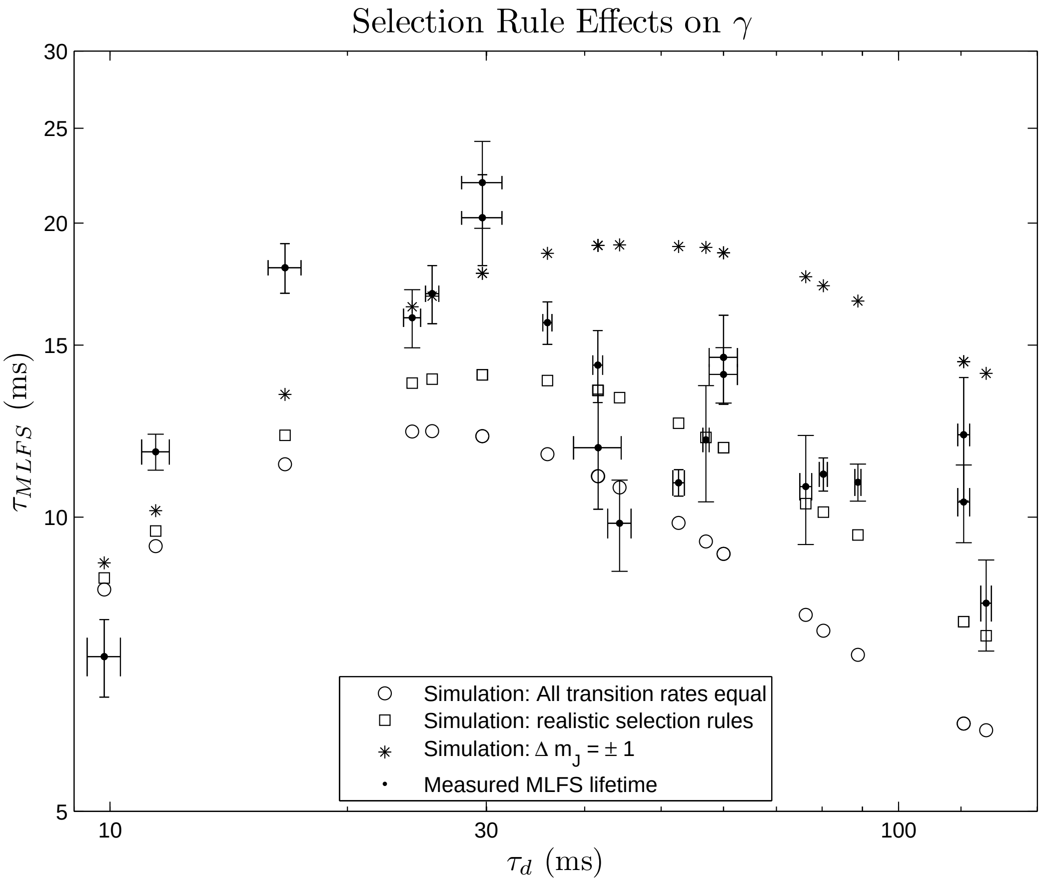

Figure 4-14: Effects of assumed selection rules on $\gamma$. In the above simulations we assume $\gamma = 5 \times 10^3$ and T = 750 mK. The behavior clearly depends on the assumed selection rules. The effect of collisional excitation on the value of $\gamma$ determined from our data depends upon which selection rules are assumed. Although we have guidance from the literature [26, 43] on realistic selection rules, we do not know them for sure. We use the extremes in selection rules ($\Delta m_J = \pm 1$; all transition rates are equal) to set a lower bound of $\gamma > 2 \times 10^3$.

excitation into the MLFS depends on which selection rule is assumed. Therefore the predicted decay rate out of the MLFS state depends on the assumed selection rules. This creates an uncertainty in the value of $\gamma$ determined by the fit of the data to the simulation.

Although the literature gives guidance in setting realistic selection rules it is impossible to quantify the accuracy of our guess. We therefore consider the effect on the fit value of $\gamma$ as we vary the selection rules. One extreme case is to impose a strict selection rule that $\Delta m_J = \pm 1$. The opposite extreme is to assume that the rates into all energetically allowed states are equal. We quantify the selection rule uncertainty by fitting the entire data set to the simulation while varying the selection rules. The result is shown in Table 4.4. The values of $\gamma$ vary between $2 \times 10^3$ and $7 \times 10^3$. We assign a lower bound of $\gamma > 2 \times 10^3$ based on this result. We show the effect graphically in Figure 4-14. Three simulations are plotted along with the data. Each simulation assumes a different selection rule with $\gamma = 5 \times 10^3$ and T = 750 mK. The choice of selection rule clearly affects the predicted MLFS behavior.

The data point at $\tau_d = 10ms$, $\tau_{MLFS} = 7ms$ consistently falls below all model predictions. There is no physical reason that the MLFS lifetime should be shorter than the zero-field diffusion lifetime. Perhaps the MLFS lifetime at such low values of $\tau_d$ is affected by an effect not considered in the model. The other data points for $\tau_d < 30ms$ consistently fall above the model predictions. We wondered if fitting for $\gamma$ after removing the $\tau_d = 10ms, \tau_{MLFS} = 7ms$ data point from the data set would improve the agreement between the rest of the low $\tau_d$ data region and the Zeeman cascade simulation model. We therefore replaced the $\tau_d = 10ms$, $\tau_{MLFS} = 7ms$ data point with two hypothetical data points at $\tau_d = 10ms$, $\tau_{MLFS} = 10ms$ and repeated

| Thermal Effects Considered? | Temperature | Selection Rules | Fit for $\gamma$ | $\chi^2$ |
|---|---|---|---|---|
| Yes | 0.6K | From Literature | $5 \times 10^3$ | 161 |
| Yes | 0.6K | All Equal | $6.5 \times 10^3$ | 163 |
| Yes | 0.6K | $\Delta m_J = 1$ | $2.5 \times 10^3$ | 177 |
| Yes | 0.75K | From Literature | $5.5 \times 10^3$ | 161 |
| Yes | 0.75K | All Equal | $7.5 \times 10^3$ | 155 |
| Yes | 0.75K | $\Delta m_J = 1$ | $2.5 \times 10^3$ | 187 |
| Yes | 1.0K | From Literature | $5 \times 10^3$ | 160 |
| Yes | 1.0K | All Equal | $8 \times 10^3$ | 143 |
| Yes | 1.0K | $\Delta m_J = 1$ | $2 \times 10^3$ | 218 |

Table 4.5: Value of $\gamma$ extracted from fits of data to Zeeman cascade simulations after replacing lowest $\tau_d$ data point with two hypothetical data points at $\tau_d = 10ms, \tau_{MLFS} = 10ms$. We wanted to see if the agreement between the low $\tau_d$ data region and the model could be improved if we ignored the lowest $\tau_d$ data point. There is very little difference between these results and the fits for $\gamma$ obtained when all of the data is included (see Table 4.4), and our limits on $\gamma$ are unaffected by the above analysis.

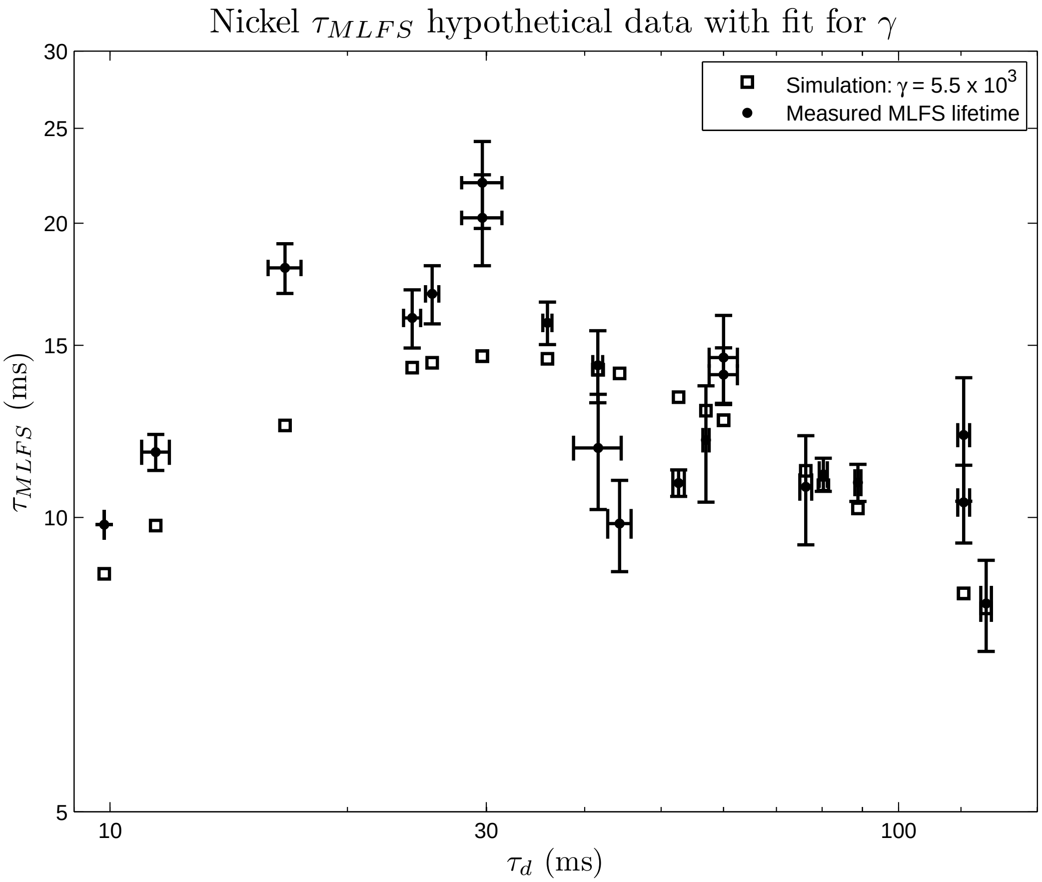

Figure 4-15: Nickel hypothetical data with fit to Zeeman Cascade simulation. The lowest $\tau_d = 10ms$, $\tau_{MLFS} = 7ms$ point from the data set has been replaced by two $\tau_d = 10ms$, $\tau_{MLFS} = 10ms$ points in an attempt to see if the agreement between the low $\tau_d$ region of data and the model can be improved. The squares are the best fit simulations to the data, yielding a value of $\gamma = 5.5 \times 10^3$. Agreement with the model is still poor for low values of $\tau_d$, and the best fit value for $\gamma$ is nearly identical to the value of $5 \times 10^3$ found using the original data set.

all of the previously described analysis by varying temperature and selection rules and fitting for $\gamma$. We hoped to see better agreement between the model predictions for $\tau_{MLFS}$ and the data at low $\tau_d$. The resulting fits for $\gamma$ are listed in Table 4.5. The results are nearly identical to the results in Table 4.4. The relative sizes of the $\chi^2$ values for the various fits are even similar. The agreement with the $\tau_d < 30ms$ region did not improve appreciably and the values of $\gamma$ are nearly indistinguishable from those obtained when the $\tau_d = 10ms$, $\tau_{MLFS} = 7ms$ data point was included. The bounds on $\gamma$ found in the previous paragraphs are not changed by this analysis. Figure

4-15 shows the hypothetical data set with the best fit value of $5.5 \times 10^3$ assuming realistic selection rules and T = 750 mK. It is nearly identical to Figure 4-10.

It is interesting to note that although it is the temperature of the atoms that causes the thermal excitation to occur, the larger source of uncertainty is in the selection rule assumptions. For our temperature range it is the selection rule assumptions that impact the perceived Zeeman relaxation rate. This can be understood as follows. Recall that $\Gamma_{zr} = (\overline{v}^2 \tau_d \chi)/\gamma$ where $\overline{v} \propto T$. As the temperature increases, the Zeeman relaxation increases proportional to temperature. However, this increase in the Zeeman relaxation rate with temperature is counteracted by the decrease in the perceived $\Gamma_{zr}$ due to collisional excitations. The overall effect causes the uncertainty of the fits caused by temperature to be less important than the uncertainty caused by selection rule assumptions and systematics in the data.

Finally, it is worth comparing our result to the unphysical case where all thermal effects are ignored. We can fit the data to the simple model presented in Section 2.2.3. The results are listed at the bottom of Table 4.4. Notice that inclusion of thermal effects universally lowers the value of $\gamma$. This occurs because thermal excitations decrease the overall loss rate from the MLFS state. As a result, the MLFS state lifetime is *longer* than it would be in the absence of thermal excitation[2]. The simple model assumes that the increase in $\tau_{MLFS}$ is attributed to the Zeeman relaxation process instead of thermal processes. It therefore underestimates the inelastic collision cross section, giving a falsely high value for $\gamma$. Figure 4-16 shows the best fit for $\gamma$ assuming T = 750 mK.

In summary, our data and analysis constrains the value of $\gamma$ for nickel-helium collisions to be between $2 \times 10^3$ and $1.1 \times 10^4$. The most significant sources of uncertainties are twofold. First, a value of $\gamma$ cannot be found that agrees well with the entire data set. Either the low $\tau_d$ region or the high $\tau_d$ region agrees with the simulation, but not both. Second, the assumed selection rules for Zeeman transitions used in the Zeeman Cascade simulations affect the value of $\gamma$ attained from the fit. A change in the assumed selection rule changes the predicted deviation of the MLFS

---

[2] This issue is discussed in greater detail in Section 2.3.6 and demonstrated in Figure 2-13.

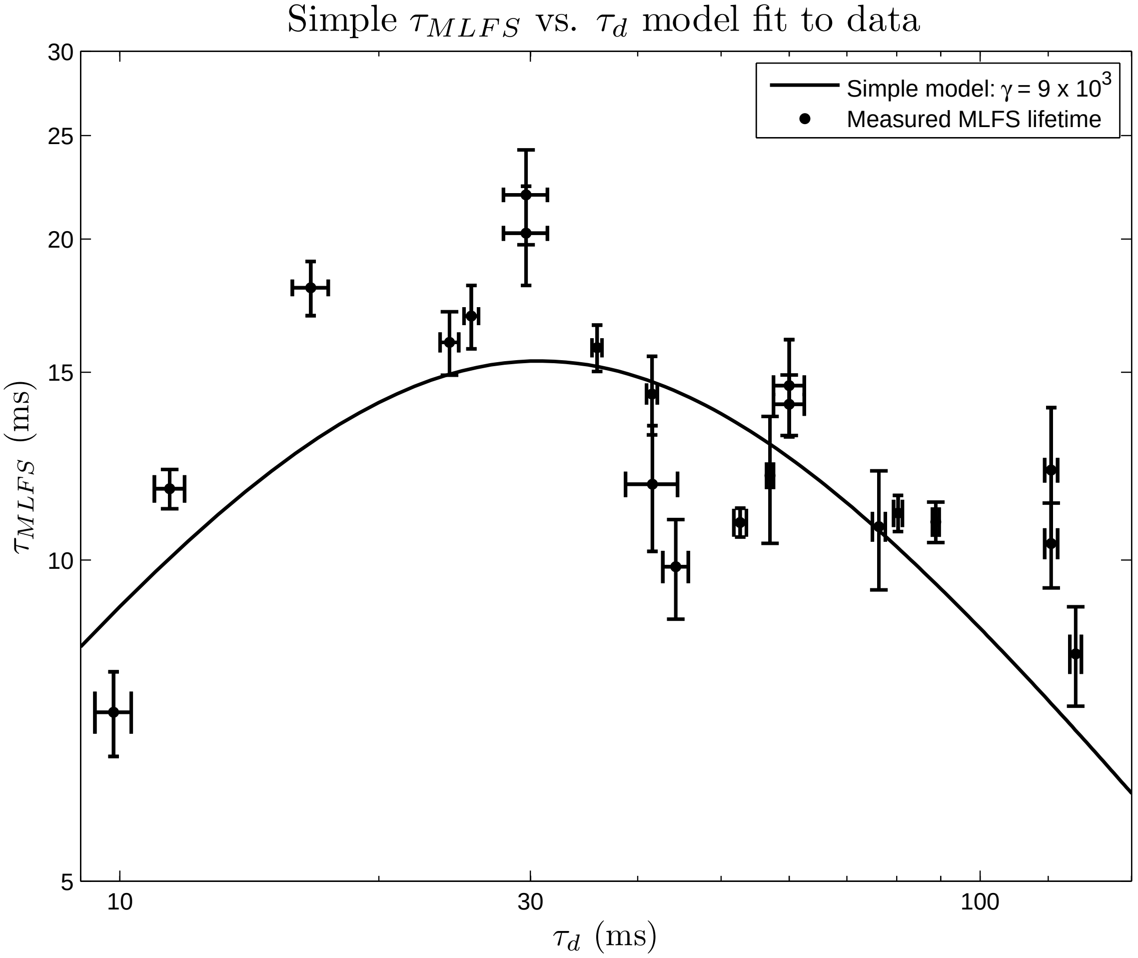

Figure 4-16: Simple model without thermal excitation: best fit for $\gamma$ assuming T = 750 mK. The value of $\gamma$ obtained from this model is an overestimate because thermal excitations are not considered.

state decay rate from the pure Zeeman relaxation rate $\Gamma_{zr}$. $\Gamma_{zr}$ is proportional to the inelastic collision cross section $\sigma_{zr}$. Because $\gamma$ is a measurement of the ratio of elastic to inelastic cross sections, a variation in the selection rules results in a change in the value of $\gamma$.

## 4.3 Iron: Upper Limit on $\gamma$

We also attempted to measure $\gamma$ for collisions between iron and $^3$He. All spectroscopic teachniques to measure temperature, density, and $\tau_d$, $\tau_{MLFS}$, $\tau_{MHFS}$ are the same as they were for the Nickel measurement. Of iron's naturally occurring isotopes, only

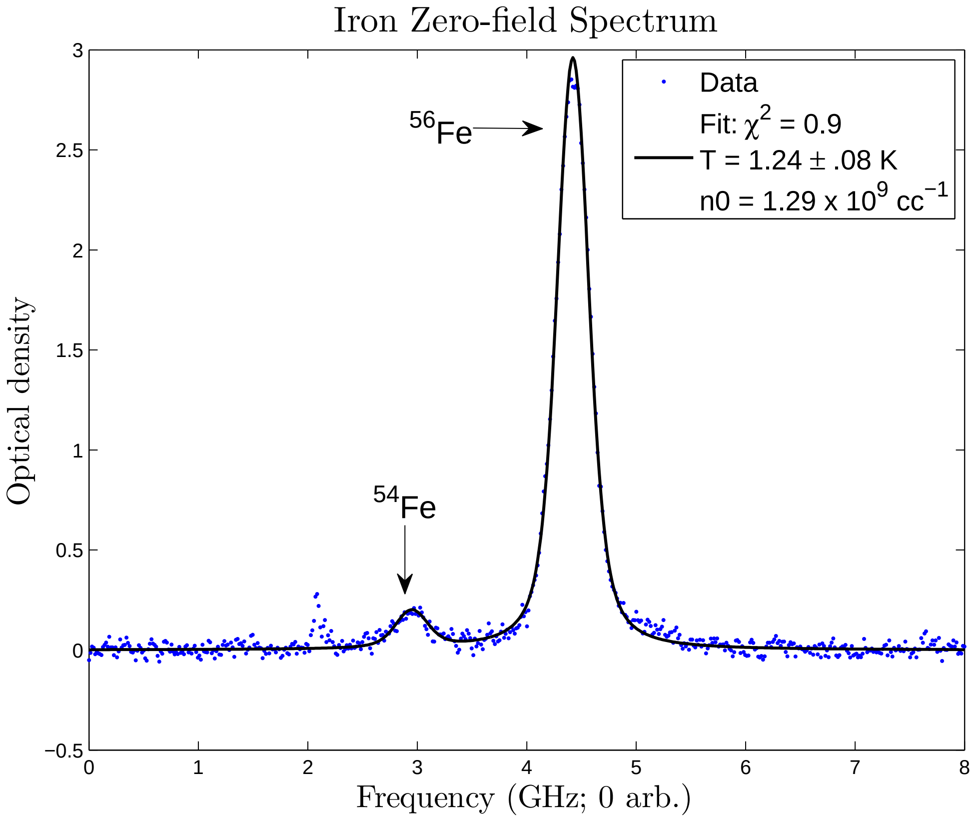

Figure 4-17: Zero-field Iron spectrum fit for density and temperature. Temperature is obtained by fitting a Voigt profile to the spectrum.

$^{57}$Fe has a nuclear spin (I = 1/2) and its natural abundance is 2%. The most common isotopes, $^{56}$Fe and $^{54}$Fe have no nuclear spin and natural abundances of 92% and 6% respectively. As a result, iron, like nickel, is a $J = 4$ atom without hyperfine structure and their energy level structures are very similar.

Figure 4-17 shows the zero-field spectrum of the $a^5D_4 \rightarrow x^5F_5$ transition at 248.4 nm taken 8 ms after ablation. The density of $1.29 \times 10^9$ cm$^{-3}$ corresponds to $1.5 \times 10^{11}$ thermalized Fe atoms. We isolate the MLFS state by turning on the Helmholtz field. Figure 4-18 shows the $\Delta m_J = 1$ transition. There are 9 lines corresponding to the $m_J$ ground states. Because $^{56}$Fe comprises > 90 % of the isotopic population we do not observe an overlap of different isotopic lines as we did in nickel.

The measurement of $\gamma$ for iron was difficult because of its rapid Zeeman relaxation. In our measurements of $\tau_{MLFS}$ vs. $\tau_d$ we did not observe a diffusion dominated region.

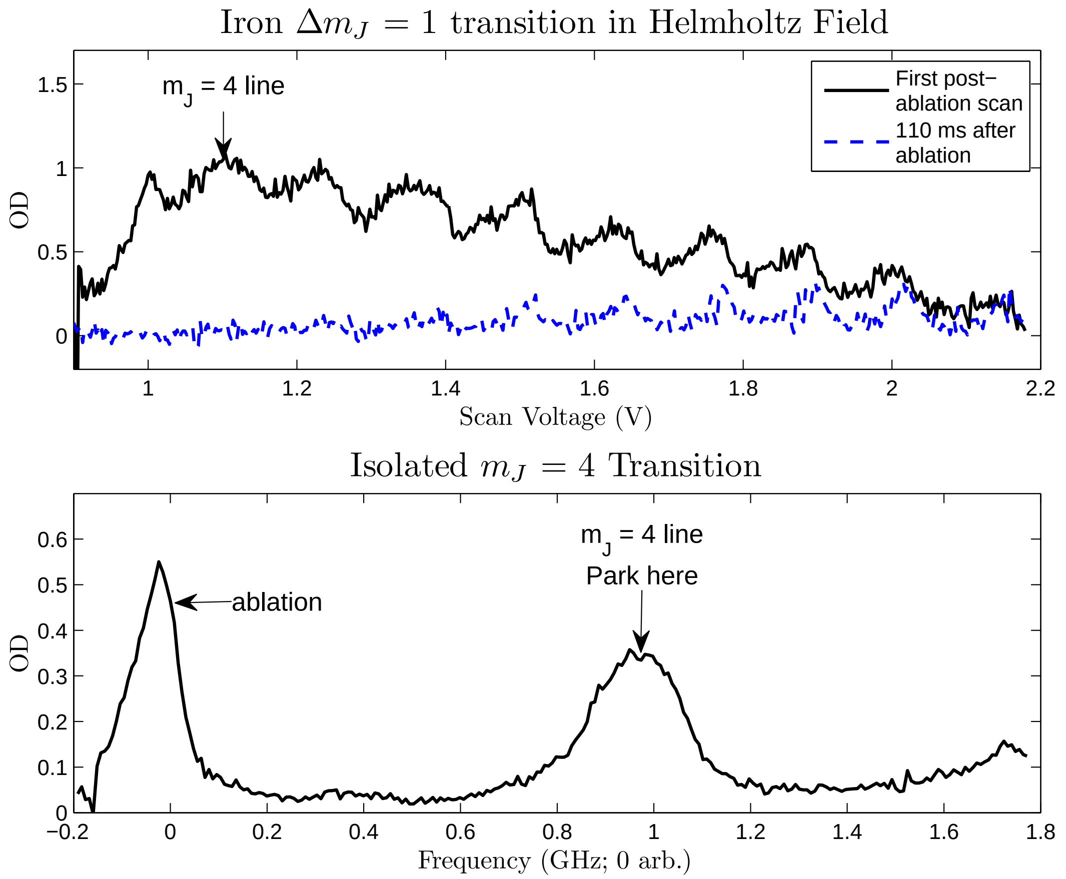

Figure 4-18: Iron observed spectrum in 0.5 T Helmholtz field. The top figure shows a spectrum immediately after ablation and another approximately 100 ms after ablation. The $m_J = 4$ population has decayed away completely. In the bottom plot the laser scan range has been decreased to isolate the $m_J = 4$ peak. The laser is tuned to the peak of the resonance to measure the decay of the MLFS state population decay.

In fact, the relaxation was so rapid for all buffer gas densities that it was difficult to make any kind of $\tau_{MLFS}$ measurement. Immediately after the ablation pulse we typically see an absorption signal that decays in 2-3 milliseconds. This early decay occurs at all buffer gas densities and contains no reliable information. We prefer to avoid this transient signal and ignore absorption data taken in the first $\sim$ 10 ms after ablation. In iron this was impossible because after 10 ms the signals were quite small and $\tau_{MLFS}$ could not be measured. We therefore measure Fe lifetimes starting $\sim$ 5 ms after ablation. Figure 4-19 shows the measured $\tau_{MLFS}$ as a function of $\tau_d$. Notice that at low buffer gas densities we do not see the increase in lifetime associated

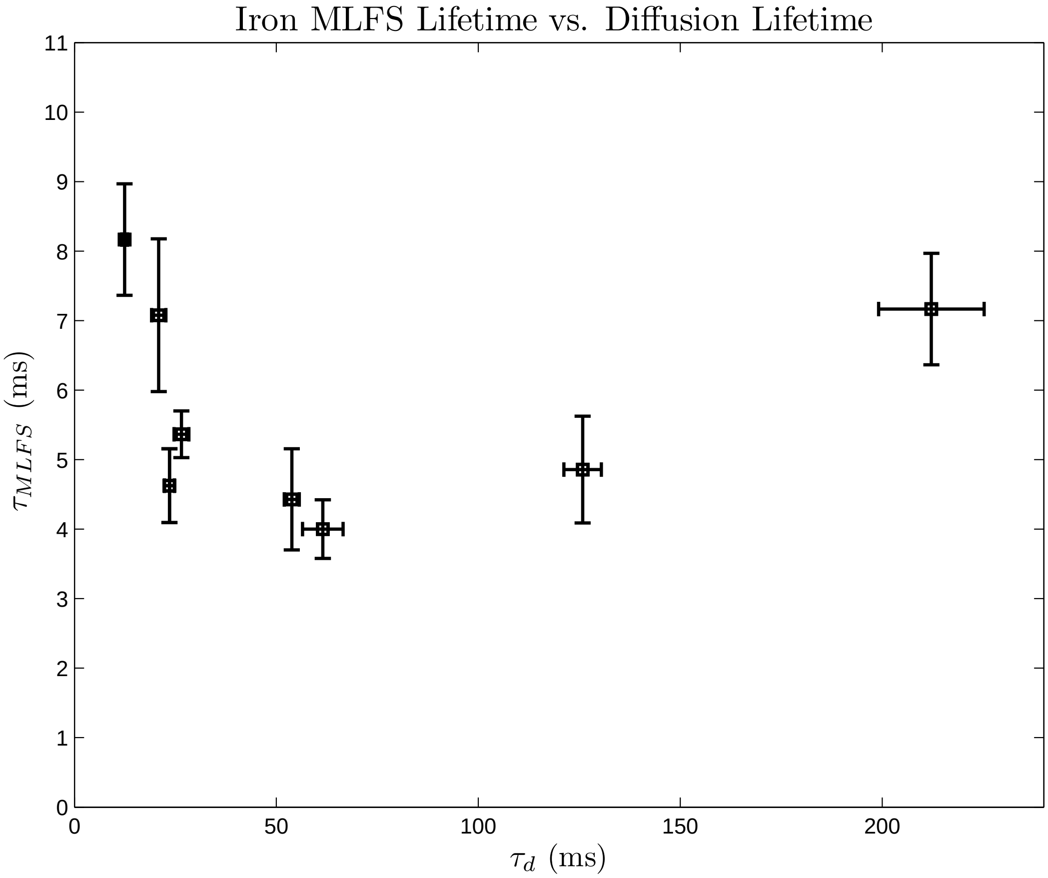

Figure 4-19: Iron MLFS lifetime versus Diffusion Lifetime. There is no region of $\tau_d$ for which $\tau_{MLFS}$ increases. This indicates that Zeeman relaxation loss dominates diffusion loss for all observed values of $\tau_d$ and we can set an upper limit of $\gamma < 3\times10^3$.

with diffusion. There is a region where the lifetime decreases slightly followed by an apparent increase in lifetime at higher buffer gas densities. We are most likely measuring a combination of $\tau_{MLFS}$ and $\tau_d$ which can lead to an apparent increase in $\tau_{MLFS}$ as discussed in Section 2.3.6. It is tempting to assume that the decrease in iron lifetime at low values of $\tau_d$ is due to Zeeman relaxation. However, without an observation of the diffusion dominated regime we are not comfortable assigning a quantitative value for $\gamma$. However, we can set a convincing upper limit.

We see no indication in any of our iron $\tau_{MLFS}$ measurements that we are in a diffusion-dominated regime even at the lowest buffer gas densities. We conclude that Zeeman relaxation occurs on a time scale faster than zero-field diffusion for every observed value of $\tau_d$. We wish to set the most conservative upper bound for $\gamma$ that is consistent with our observation that diffusion does not dominate Zeeman relaxation even for our lowest measured value of $\tau_d = 13$ ms. We do not wish to quote a limit that is artificially low, so our assumptions will all serve to elevate the limit of $\gamma$.

In order to set the limit, we recast Equation 2.28 into the following form:

$$\gamma = \tau_d \tau_{zr} \overline{v}^2 \chi \tag{4.4}$$

Recall that $\overline{v}$ is the relative velocity between a helium and iron atom during a collision $\chi$ is a known geometric factor. We therefore need conservative estimates of $\tau_{zr}$ and $\overline{v}$ for the data point associated with our lowest measured $\tau_d$.

Recall that $\tau_{MLFS}$ is a combined effect of the diffusion and Zeeman relaxation lifetimes. When $\tau_d = \tau_{zr}$ the diffusion and Zeeman relaxation loss rates are equal and the expected value of $\tau_{MLFS} = \tau_d/2$. We assume that this condition is met since it is within the error bar of our lowest $\tau_d$ point. This is the most conservative estimate because it implies that $\tau_{zr}$ is at its largest possible value to still be consistent with our observation that $\tau_{MLFS} < \tau_d$. In order to estimate $\overline{v}$ we use the temperature obtained from the zero-field spectrum taken 8 ms after ablation shown in Figure 4-17. Under these conservative assumptions we set a limit for iron of $\gamma < 3 \times 10^3$.

# Chapter 5

# Conclusions and Outlook

## 5.1 Summary of Iron and Nickel Results

A study of collisions between the most low-field seeking state of nickel and iron with $^3$He has been performed. The ratio of elastic to inelastic collisions $\gamma$ for the Ni-He system has been found to be between $2 \times 10^3$ and $1.1 \times 10^4$. An upper limit on $\gamma$ in the Fe-He system of $3 \times 10^3$ has been set. Although the elastic and inelastic collision rates each depend on the buffer gas density, a method has been developed to measure the ratio $\gamma$ without direct knowledge of buffer gas density. Under our experimental conditions the energy splitting between adjacent Zeeman levels was on the same order as the thermal energy of the atomic sample. Under these circumstances, thermal excitation into the MLFS state alter its perceived Zeeman relaxation rate and must be included in the analysis. The values of $\gamma$ for iron and nickel are too small to effectively load MLFS atoms into a magnetic trap using the buffer gas loading technique. Rapid Zeeman relaxation of MLFS atoms in collisions with the buffer gas causes population transfer into untrapped states before the buffer gas can be removed from the system.

The measurements further demonstrate the phenomenon that inelastic processes are suppressed in transition metal-helium collisions. The anisotropy of the collision is small because the coulomb repulsion of the helium atom by the full outer $4s$ electronic shell in the transition metal prevents the helium electronic cloud from sampling the anisotropic d-shell valence electrons. The small interaction anisotropy results in a large value for $\gamma$.

## 5.2 Outlook: 1 $\mu_B$ and Rare Earth Element Evaporative Cooling

Although the measured collisional properties of the Fe-He and Ni-He systems are interesting, there is no motivation to study transition metals further in our apparatus. Because $\gamma$ for the iron and nickel were not greater than $10^4$ they are not good candidates for loading a magnetic trap in a buffer gas apparatus. The successful trapping of lithium, copper, and silver in our apparatus motivates us to pursue evaporative cooling of these and other species. Our attempts to evaporatively cool lithium are detailed Newman's thesis [20]. We put much effort into minimizing the background buffer gas density to thermally disconnect the trapped sample from the cell wall. The cryogenic valve and pumpout sorb were implemented to remove buffer gas quickly after trap loading. The wired cell was carefully designed to maintain low base temperatures during magnet ramps. Despite these efforts we were not able to lower the trapped lithium sample temperature more than a factor of two below the cell wall temperature. Successful evaporation requires a further reduction in the cell temperature to bind the helium film more tightly to the wall. We are currently considering cell design options to increase thermal conductivity along the walls and to the mixing chamber. In addition, evaporative cooling of a heavier alkali may be more successful. The larger mass mismatch with helium could lead to less efficient energy transfer and a lower heating rate due to background gas.

The values of $\gamma$ in collisions with helium have been measured for several rare earth elements [24]. The values range between $2.7 \times 10^4$ and $4.5 \times 10^5$; large enough to load them into a magnetic trap if the buffer gas can be removed quickly. Our apparatus is particularly well suited to trap these atoms because of its capability of fast buffer gas removal. We are currently exploring the feasibility of evaporatively cooling rare earth elements by measuring the dipolar two-body loss rates of dysprosium and holmium.

# Appendix A

# Wired Cell and Pumping Sorb Construction

## A.1 Wired Cell Construction

The wired cell design requires $\sim$ 1000 0.25 mm wires to be expoxied to the outside wall of the G10 cell body. This task poses two major difficulties. First, the density of wires on the surface of the cell body must as high as possible to maximize thermal conductivity along the wall. Thus the wires must be highly parallel and densely packed. Second, the mixing chamber is $\sim$ 10 inches above the top of the cell. Thus all each needs an additional 15-20 inches of length beyond the top of the cell so they can be heat sunk to the refrigerator. It is a nontrivial task to elegantly lay down $\sim$ 1000 thin, long wires on the outside of a cylinder so they are perfectly parallel and densely packed. The method described below will hopefully aid future design and construction efforts.

We designed a wire winding jig shown in Figure A-1. The jig provides a form on which the wires could be positioned precisely and packed densely. A 20 inch PVC pipe section with an outer diameter equal to the to the outer diameter of the cell fits tightly into the top of the cell body. This PVC section keeps the extra 20 inches of wire length aligned with the cell body during the epoxy process. A 1/2 inch long teflon ring matching the cell outer diameter fits into the bottom of the cell body.

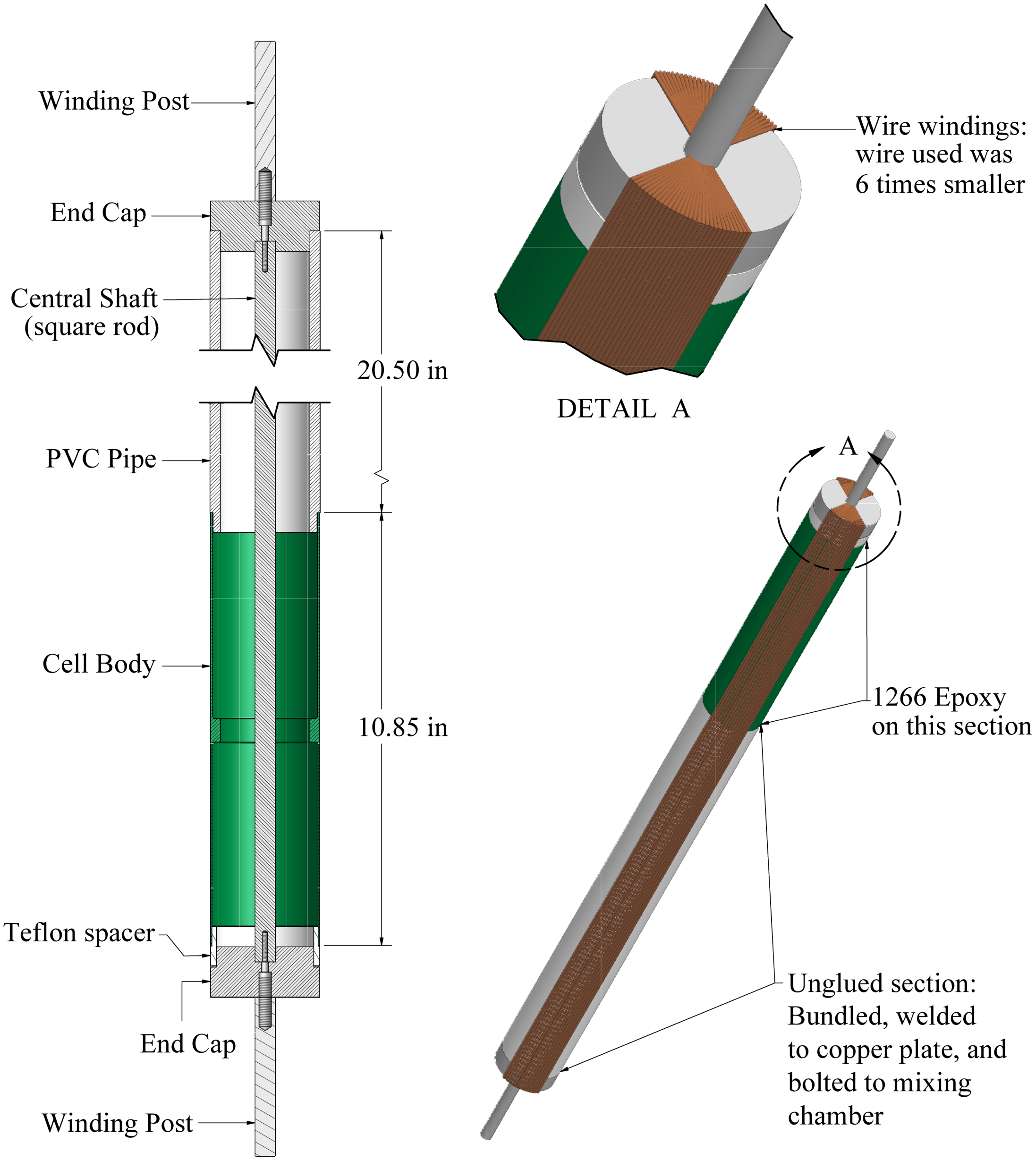

Figure A-1: Cell wire winding jig.

The Stycast 1266 epoxy used to glue the cell wires does not stick to teflon, so the teflon ring prevents the cell wires from being epoxied to the winging jig. Each end of the tube is capped with an aluminum end cap. These end caps each have a 0.5 inch diameter, 6 inch length aluminum rod screwed into them. The rods, or “winding posts”, support the weight of the winding jig during construction. Any rotation of the end caps causes the wires to become twisted and not lay parallel to the cell axis.

A square rod runs down the middle of the entire structure and mates with a square hole in each end cap. This prevents the end caps from rotating with respect to each other.

The cell winding is started by tying the magnet wire to one of the winding posts (winding post 1). The wire is laid down the length of the tube, wrapped half way around the other winding post (winding post 2), laid down along the opposite side of the tube, wrapped halfway around winding post 1, laid back down the tube, wrapped halfway around winding post 2 etc. etc. In this way the entire cell is wound without ever having to cut the spool of wire. As the wire is laid down it is epoxied to the cell body. Care is taken to make sure the epoxy coating is thorough and even but not excessive. The process requires at least 3 people at all times to wind the wire, keep the wires straight and densely packed, and lay down epoxy. Fresh epoxy is made whenever the old batch starts to get too viscous. After all the wires are laid down and epoxied, kevlar thread is wound around the circumference of the top and bottom of the cell and embedded in epoxy to provide additional constraint to the wires at the end of the cell.

After the epoxy is dry, the wires are clipped at the end caps and the winding jig is disassembled. The brass cell adaptor ring (see Figure 3-4) is carefully epoxied into the cell top paying careful attention not to kink the wires. The adaptor ring creates an indium seal with the valve assembly to complete the cell vacuum space. The extra lengths of wire are bundled, stripped of insulation, and welded to a copper plate. During cooldown preparation the copper plate is bolted to the mixing chamber clamp.

## A.2 Pumping Sorb Design

Our pumping sorb resides in the pumping chamber above the trapping region along with the valve apparatus. This caused us some problems in early runs because over time some of the activated charcoal would shed from the pumping sorb and fall onto the valve seat. This degraded valve performance. The sorb shown in Figure A-2 was designed to solve this problem and has worked flawlessly in three separate runs.

Activated charcoal is epoxied to the inside surface of a copper can with Stycast 2850. In our case the copper can has a gap along its length to accommodate our buffer gas fill line which runs through the pumping region. Over time small pieces of charcoal become unattached from the copper can and can fall onto the valve seat. To prevent this, we enclose the entire inside surface of the copper can behind a layer of very fine nylon mesh. A brass frame is soldered to the inside edges of the copper can. This frame provides a surface to which a carefully cut piece of mesh can be epoxied, sealing in any sorb that becomes unattached from the copper can during the experimental run.

We have built sorbs nearly identical to the one described above but with all copper and brass parts replaced with G10. This makes it possible to ramp the magnetic field without inducing unwanted eddy current heating.

It has been suggested that a sorb heat sunk to the $\sim 100mK$ coldest part of the cell might not pump as efficiently as a sorb heat sunk to a surface above 1K [50]. During most of our experimental runs the sorb has been heat sunk to the coldest part of the experimental cell. In the most recent cooldown the sorb was mounted to the stainless steel valve plate which is thermally sunk to the still. We have not yet fully explored whether the sorb pumps more efficiently in this elevated temperature configuration.

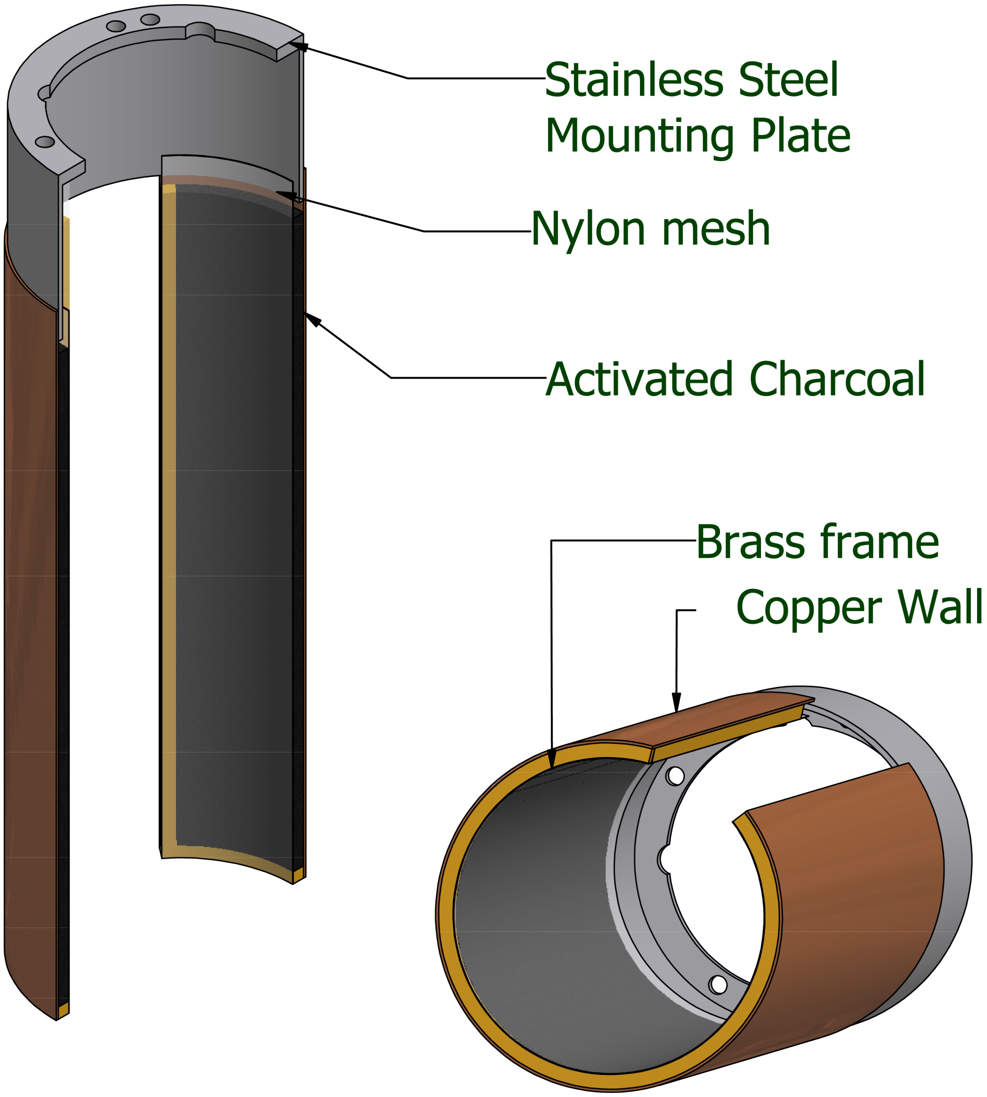

Figure A-2: Cell pumping sorb. Charcoal is expoxied to the inside of the copper can. A fine nylon mesh is expoxied to the brass frame to completely enclose the charcoal. Any small pieces of charcoal dislodged from the copper can during the experimental run cannot fall onto the valve seat.

# Bibliography

[1] M. H. Anderson, J. R. Ensher, M. R. Matthews, C. E. Wieman, and E. A. Cornell. Observation of Bose-Einstein Condensation in a Dilute Atomic Vapor. *Science*, 269(5221):198–201, 1995.

[2] K. B. Davis, M. O. Mewes, M. R. Andrews, N. J. van Druten, D. S. Durfee, D. M. Kurn, and W. Ketterle. Bose-einstein condensation in a gas of sodium atoms. *Phys. Rev. Lett.*, 75(22):3969–3973, Nov 1995.

[3] National Research Council of the National Academies Committee on AMO 2010. *Controlling the Quantum World: The Science of Atoms, Molecules, and Photons.* The National Academies Press, Washington, D.C., 2007.

[4] William D. Phillips. Nobel lecture: Laser cooling and trapping of neutral atoms. *Reviews of Modern Physics*, 70:721–741, 1998.

[5] Dale G. Fried, Thomas C. Killian, Lorenz Willmann, David Landhuis, Stephen C. Moss, Daniel Kleppner, and Thomas J. Greytak. Bose-einstein condensation of atomic hydrogen. *Phys. Rev. Lett.*, 81(18):3811–3814, Nov 1998.

[6] Dale G. Fried. *Bose-Einstein Condensation of Atomic Hydrogen.* PhD thesis, Massachusetts Institute of Technology, Cambridge, MA, June 1999.

[7] Thomas Charles Killian. *$1S - 2S$ Spectroscopy of Trapped Hydrogen: The Cold Collision Frequency Shift and Studies of BEC.* PhD thesis, Massachusetts Institute of Technology, Cambridge, MA, February 1999.

[8] A. I. Safonov, S. A. Vasilyev, A. A. Kharitonov, S. T. Boldarev, I. I. Lukashevich, and S. Jaakkola. Adsorption and two-body recombination of atomic hydrogen on $h3e - h4e$ mixture films. *Phys. Rev. Lett.*, 86(15):3356–3359, Apr 2001.

[9] Julia K. Steinberger. *Progress Towards High Precision Measurements on Ultracold Metastable Hydrogen and Trapping Deuterium.* PhD thesis, Massachusetts Institute of Technology, Cambridge, MA, August 2004.

[10] A. P. Mosk, M. W. Reynolds, and T. W. Hijmans. Atomic deuterium adsorbed on the surface of liquid helium. *Phys. Rev. A*, 64(2):022901, Jun 2001.

[11] S. V. Nguyen, J. S. Helton, K. Maussang, W. Ketterle, and John M. Doyle. Magnetic trapping of an atomic $^{55}$Mn-$^{52}$Cr mixture. *Physical Review A (Atomic, Molecular, and Optical Physics)*, 71(2):025602, 2005.

[12] M. J. Jamieson, A. Dalgarno, and M. Kimura. Scattering lengths and effective ranges for he-he and spin-polarized h-h and d-d scattering. *Phys. Rev. A*, 51(3):2626–2629, Mar 1995.

[13] R. Côté, M. J. Jamieson, Z-C. Yan, N. Geum, G.-H. Jeung, and A. Dalgarno. Enhanced cooling of hydrogen atoms by lithium atoms. *Phys. Rev. Lett.*, 84(13):2806–2809, Mar 2000.

[14] A. Derevianko, R. Côté, A. Dalgarno, and G.-H. Jeung. Enhanced cooling of hydrogen by a buffer gas of alkali-metal atoms. *Phys. Rev. A*, 64(1):011404, Jun 2001.

[15] Kendra Margaret Denny Vant. *Spectroscopy of ultracold metastable hydrogen: in pursuit of a precision measurement.* PhD thesis, Massachusetts Institute of Technology, Cambridge, MA, June 2005.

[16] Lia Machado de Matos. *Octave-spanning lasers for optical metrology applications.* PhD thesis, Massachusetts Institute of Technology, Cambridge, MA, February 2006.

[17] Robert Michniak. *Enhanced Buffer Gas Loading: Cooling and Trapping of Atoms with Low Effective Magnetic Moments.* PhD thesis, Harvard University, 2004.

[18] Jonathan D. Weinstein, Robert deCarvalho, Thierry Guillet, Bretislav Friedrich, and John M. Doyle. Magnetic trapping of calcium monohydride molecules at millikelvin temperatures. *Nature*, 395:148–150, 1998.

[19] Nathaniel Charles Brahms. *Trapping of 1 $\mu_B$ atoms using buffer gas loading.* PhD thesis, Harvard University, 2008.

[20] Bonna Kay Newman. PhD thesis, Massachusetts Institute of Technology, Cambridge, MA, August 2008.

[21] Nathan Brahms, Bonna Newman, Cort Johnson, Tom Greytak, Daniel Kleppner, and John Doyle. (submitted for publication).

[22] John M. Doyle, Bretislav Friedrich, Jinha Kim, and David Patterson. Buffer-gas loading of atoms and molecules into a magnetic trap. *Phys. Rev. A*, 52(4):R2515, 1995.

[23] Robert deCarvalho, John M. Doyle, Bretislav Friedrich, Thierry Guillet, Jinha Kim, David Patterson, and Jonathan D. Weinstein. Buffer-gas loaded magnetic traps for atoms and molecules: a primer. *Eur. Phys. J. D*, 7:289, 1999.

[24] C. I. Hancox, S. C. Doret, M. T. Hummon, L. Luo, and J. M. Doyle. *Nature (London)*, 431:281, 2004.

[25] R. V. Krems and A. Dalgarno. Quantum-mechanical theory of atom-molecule and molecular collisions in a magnetic field: Spin depolarization. *The Journal of Chemical Physics*, 120(5):2296–2307, 2004.

[26] R. V. Krems and A. Dalgarno. Disalignment transitions in cold collisions of $^3p$ atoms with structureless targets in a magnetic field. *Physical Review A*, 68:013406, 2003.

[27] R. V. Krems and A. A. Buchachenko. *J. Chem. Phys.*, 123:101101, 2005.

[28] R. V. Krems, J. Klos, M. F. Rode, M. M. Szczesniak, G. Chalasinski, and A. Dalgarno. Suppression of angular forces in collisions of non-s-state transition metal atoms. *Phys. Rev. Lett.*, 94:013202, 2005.

[29] Jinha Kim. *Buffer Gas Loading and Magnetic Trapping of Atomic Europium.* PhD thesis, Harvard University, 1997.

[30] William H. Wing. On neutral particle trapping in quasistatic electromagnetic fields. *Progress in Quantum Electronics*, 8:181–199, 1984.

[31] T. G. Walker, J. H. Thywissen, and W. Happer. *Phys. Rev. A*, 56(3):2090, 1997.

[32] Z. Wu, T. G. Walker, and W. Happer. *Phys. Rev. Lett*, 54:1921, 1985.

[33] R. M. Herman. Noble-gas-induced rubidium spin disorientation. *Phys. Rev.*, 136(6A):A1576, 1964.

[34] Jinha Kim, Bretislav Friedrich, Dan P. Katz, David Patterson, Jonathan D. Weinstein, Robert deCarvalho, and John M. Doyle. Buffer-gas loading and magnetic trapping of atomic europium. *Physical Review Letters*, 78:3665–3668, 1997.

[35] Jonathan D. Weinstein, Robert deCarvalho, Jinha Kim, David Patterson, Bretislav Friedrich, and John M. Doyle. Magnetic trapping of atomic chromium. *Physical Review A*, 57:R3173–3175, 1998.

[36] Scott Vinh Nguyen. *Buffer gas loading and evaporative cooling in the multi-partial-wave regime.* PhD thesis, Harvard University, 2006.

[37] S R Langhoff and C W Bauschlicher. Ab initio studies of transition metal systems. *Annual Review of Physical Chemistry*, 39(1):181–212, 1988.

[38] Donald C. Griffin, Kenneth L. Andrew, and Robert D. Cowan. Theoretical calculations of the *d*-, *f*-, and *g*-electron transition series. *Phys. Rev.*, 177(1):62–71, Jan 1969.

[39] C. I. Hancox, S. C. Doret, M. T. Hummon, R. V. Krems, and J. M. Doyle. *Phys. Rev. Lett.*, 94:013201, 2005.

[40] Cindy Irene Hancox. *Magnetic trapping of transition-metal and rare-earth atoms using buffer-gas loading.* PhD thesis, Harvard University, 2005.

[41] Roman Krems, private communication.

[42] J. B. Hasted. *Physics of Atomic Collisions.* Butterworth, 1972.

[43] A. A. Buchachenko, G. Chalasinski, M. M. Szczesniak, and R. V. Krems. Ab initio study of tm-he interactions and dynamics in a magnetic trap. *Physical Review A (Atomic, Molecular, and Optical Physics)*, 74(2):022705, 2006.

[44] Robert C. Richardson and Eric N. Smith, editors. *Experimental techniques in condensed matter physics at low temperatures.* Addison-Wesley, 1988.

[45] Jonathan David Weinstein. *Magnetic Trapping of Atomic Chromium and Molecular Calcium Monohydride.* PhD thesis, Harvard, 2001.

[46] Frank Pobell. *Matter and Methods at Low Temperatures.* Springer, 2 edition, 1996.

[47] J. G. E. Harris, R. A. Michniak, S. V. Nguyen, W. C. Campbell, D. Egorov, S. E. Maxwell, L. D. van Buuren, and J. M. Doyle. Deep superconducting magnetic traps for neutral atoms and molecules. *Review of Scientific Instruments*, 75(1):17–23, 2004.

[48] Robert deCarvalho. *Inelastic Scattering of Magnetically Trapped Atomic Chromium.* PhD thesis, Harvard University, 2003.

[49] Vespel is wear resistant polyimide-based plastic with a low coefficient of friction manufactured by Dupont: http://www2.dupont.com/Vespel/en_US/.

[50] John Doyle, personal communication.

[51] Harald E. Hess. Evaporative cooling of magnetically trapped and compressed spin-polarized hydrogen. *Phys. Rev. B*, 34:3476, 1986.

[52] W. Ketterle and N.J. Van Druten. Evaporative cooling of trapped atoms. *Advances in Atomic, Molecular, and Optical Physics*, 37:181–236, 1996.

[53] Jonathan David Weinstein. *Magnetic Trapping of Atomic Chromium and Molecular Calcium Monohydride.* PhD thesis, Harvard University, 2001.

[54] John Morrissey Doyle. *Energy Distribution Measurements of Magnetically Trapped Spin Polarized Atomic Hydrogen: Evaporative Cooling and Surface Sticking.* PhD thesis, Massachusetts Institute of Technology, Cambridge, MA, May 1991.

[55] R. J. Donnelly. *Experimental Superfluidity.* Chicago Lectures in Physics. The University of Chicago Press, Chicago and London, 1967.

[56] Purchased from McMaster: www.mcmaster.com.

[57] Lakeshore RX-102A: http://www.lakeshore.com/temp/sen/rrtd.html.

[58] Hamamatsu sells compact PMT modules which are convenient to mount and do not require a high voltage supply: www.hamamatsu.com.

[59] Claude Cohen-Tannoudji, Jacques Dupont-Roc, and Gilbert Grynberg. *Atom-Photon Interactions: basic processes and applications.* John Wiley & Sons, Inc., 1992.

[60] Harold J. Metcalf. *Laser cooling and trapping.* Springer, New York, 1999.

[61] Wolfgang Demtroder. *Laser spectroscopy: basic concepts and intrumentation.* springer, 2003.

[62] Amnon Yariv. *Quantum Electronics.* John Wiley & Sons, Inc., New York, second edition, 1975.

[63] Continuum minilite: www.continuumlasers.com.

[64] Laser dyes covering the wavelength range 300 nm - 1300 nm can be purchased from Exciton: www.exciton.com.

[65] Coherent has recently stopped selling these systems and their committment to servicing them is weak. Some spare parts can be found at www.laserinnovations.com.

[66] We use Radiant Dyes nozzles and circulators. The dye jet is very flat and the circulation pressures: www.radiant-dyes.com.

[67] Stanford Research Systems DS345 function generator: http://www.thinksrs.com/products/DS345.htm.

[68] T. W. Hansch and B. Couillaud. Laser frequency stabilization by polarization spectroscopy of a reflecting reference cavity. *Optics communications*, 35(3):441–444, December 1980.

[69] V.G. Dmitriev, G.G. Gurzadyan, and D.N. Nikogosyan. *Handbook of Ninlinear Optical Crystals*, volume 64 of *Springer Series in Optical Sciences.* Springer, third revised edition, 1999.

[70] $LiIO_3$ crytal purchased from Super Optronics: 15900 Crenshaw Blvd G346 Gardena, CA , 90249-4872 Phone: 310-516-9082, www.superoptronics.com.

[71] Schott colored glass filters with a wide array of transmission curves exist: http://www.us.schott.com/optics_devices/english/products/filter/glass_filter.html.

[72] G. H. Guthöhrlein and H.P. Keller. Dopper-free laserspectroscopic investigations of hyperfine structure in the atomic cobalt spectrum. *Z. Phys. D.*, 17(3):181–193, 1990.

[73] Charlotte Moore. *Atomic Energy Levels as Derived from the Analyses of Optical Spectra*, volume 2. National Bureau of Standards, 1958.